OPTOFLUIDIC MICROSCOPY: TECHNOLOGY DEVELOPMENT AND ITS APPLICATIONS IN BIOLOGY

Thesis by

Xin Heng

In Partial Fulfillment of the Requirements for the

degree of

Doctor of Philosophy in Electrical Engineering

CALIFORNIA INSTITUTE OF TECHNOLOGY

Pasadena, California

2008

(Defended December 3, 2007)

Thesis Committee

Professor Changhuei Yang (Chair)

Professor Demetri Psaltis (co-advisor)

Professor Azita Emami-Neyestanak

Professor Paul W. Sternberg

Professor Yu-Chong Tai

Professor Sandra Troian

ACKNOWLEDGEMENTS

The success of my research has relied on the expertise of many individuals from a variety of fields. I am grateful for those who have been giving me constant support and guidance as I grew both physically and intellectually in Caltech.

Dr. Changhuei Yang has been my thesis advisor at Caltech since 2003. His undamping enthusiasm in scientific research has been a source of inspiration, motivating me to complete my research project successfully. I joined his lab as a fresh graduate student with little hands-on experience in optics. Therefore, I am very thankful to him for patiently teaching me valuable experimental skills. Under his supervision, I have trained myself into a fine (if not fantastic) experimentalist in the interdisciplinary fields of optical engineering and bioengineering.

Dr. Demetri Psaltis has been my co-advisor, ever since I started my project on developing Optofluidic Microscopy (OFM). I admire his acute physical intuition and feel extremely indebted to his supervision on my research work. I feel fortunate to be the first student on this OFM project, which has turned into a very successful collaboration between Dr. Yang's group and Dr. Psaltis's group.

I would like to express my gratitude to Dr. Azita Emami-Neyestanak, Dr. Paul Sternberg, Dr. Yu-Chong Tai and Dr. Sandra Troian for being in my thesis committee. I thank Dr. Scott Fraser, and Dr. P. P. Vaidyanathan for being part of my candidacy committee. I feel grateful to Dr. Fraser and Dr. Sternberg for letting me use their biology facilities and sharing with me their valuable biology insights.

Our Biophotonics research group is like my big family in the United States. We have worked closely with each other and enjoyed spending some social hours together. Xiquan and Lap-Man are my teammates on the OFM project. I am very thankful to their generous help and their valuable suggestions. Xiquan has helped me tremendously on using FIB to

fabricate nanophotonic devices. Lap has been a good teacher in fluidic mechanics and microfluidic design.

In addition, I would like to send my gratitude to other lab colleagues: Dr. Zahid Yaqoob, Jigang Wu, Emily McDowell, Guoan Zheng, Shuo Han, Matthew Lew, and Arthur Chang for constantly teaching me optics, fabrication, chemistry, or biology.

Thanks to Jigang Wu, Guoan Zheng, and Lapman Lee for proofreading my thesis. I know that my poor writing must have made your work awfully tough.

During my residence at Caltech, I have also benefited from the generous help of many collaborators: Dr. David Erickson (now in Cornell University), Dr. L. Ryan Baugh, Edward Hsiao, Kevin Reynolds (now in Stanford University), James Adleman, Zhenyu Li, and Jae Woo Choi, to name a few.

My final and most important acknowledgements go to my Dad, Wencai Heng, my Mom, Huiqin Zhang, and my elder sister, Yuan Heng, for their 28 years of constant support and understanding. Without their unwavering encouragement, I would not have had enough determination to complete my Ph.D. study. My mom happens to be my math teacher in elementary school.

Xin Heng

衡欣

Pasadena, CA

winter, 2007

ABSTRACT

The Optofluidic Microscope (OFM) is a new imaging platform based upon nanoapertures that are fabricated on planar metallic film, whilst microfluidic delivery technology is used to transport the objects-of-interest. The planar nature of OFM makes it ideal to integrate with other micro total analysis systems, such as cell sorters or cell culturing chambers. Furthermore, a variety of imaging functionalities, such as differential phase contrast, fluorescence, and Raman spectroscopy can potentially fit into a single OFM device.

This thesis reports on the early technology development of Optofluidic Microscopy. I have built a variety of off-chip prototypes of OFM that all possess different functionalities. These OFM prototypes include 1D array OFM, hydraulically pumped OFM, 2D nanoaperture grid OFM, super high-resolution OFM, OFM coupled with optical tweezer actuation, fluorescent OFM, electrokinetic enabled OFM, etc.

I applied the first OFM prototype in imaging *Caenorhabditis elegans (C. elegans)* larvae and characterizing different genotypes. Later on, the microscopy properties of OFM, such as the optical resolution and the depth of field, were thoroughly investigated both experimentally and theoretically. More recently, I successfully combined optical tweezers with a grid-based OFM prototype, which was then used in high-resolution imaging of microspheres and a few biological samples. In addition, preliminary results on fluorescence OFM imaging were also demonstrated.

I trust that these functionalities, after being demonstrated off-chip, can be readily fabricated and then assembled as a complete on-chip OFM. It will eventually enable a real "microscale microscope on a chip".

TABLE OF CONTENTS

LIST OF FIGURES

Chapter 1:

Chapter 2:

Chapter 3:

Chapter 4:

Chapter 5:

Chapter 6:

Chapter 7:

Chapter 8:

LIST OF TABLES

Chapter 5:

Chapter 6:

Chapter 7:

LIST OF FREQUENTLY USED ACRONYMS

Acronym	Full name
ABID	Aperture Based Imaging Device
FEM	Finite Element Methods
CPSF	Collection-mode Point Spread Function
NSOM	Near-field Scanning Optical Microscope/Microscopy
OFM	Optofluidic Microscope/Microscopy
SEM	Scanning Electron Microscope
SPP	Surface Plasmon Polariton

Chapter 1

OVERVIEW

Microfluidics is a multidisciplinary area that brings together the experts from both engineering and fundamental sciences. Optofluidics, as a specialized field of microfluidics, has not drawn much attention until very recently, when optical engineers started to recognize the unique properties of microfluidics and their huge potentials in creating novel optical devices. In this chapter, I will introduce the basics of microfluidics with special attention to microfluidic detection techniques. The physics and technology involved is closely related to the focus of my thesis: Optofluidic Microscopy. In addition, recent research on nanoapertures and their applications in optoelectronics and biology will be introduced.

1.1 Basic microfluidics

Microfluidics, as the name suggests, studies the behavior of fluid in a tiny volume from micro-liters down to pico-liters. Subsequently, the discoveries made in investigating fluidic flow in microfluidics can be used in a large number of applications, such as for controling fluid and manipulating biological samples. The length scale of microfluidics normally ranges from 10 μm to 100 μm, while there has been increased interest in studying fluid flow in sub-micrometer channels.

Microfluidic flow can behave quite differently from its macroscale counterpart. Systems in a microscale environment generally have a much higher surface-to-volume ratio. As such, surface effects such as surface tension, viscous force and fluidic resistance dominate. Microfluidic flow, especially liquid flow, is normally characterized as laminar flow, whose flow pattern is usually a function of the Reynolds number (Re), which will be introduced later.

In fluidic mechanics, the Reynolds number (Re), as arguably the most important dimensionless number, equals to the ratio of inertial forces and viscous forces. It is expressed as follows:

$$\mathrm{Re} = \frac{\rho v^2 / L}{\mu v / L^2} = \frac{\rho v L}{\mu} \qquad (1.1)$$

where ρ is the density of the fluid or the target object, v is mean fluid velocity, L is the characteristic length, and μ is the dynamic viscosity of the fluid. Laminar flow, which occurs at low Re, is characterized by smooth, constant fluid motion. Turbulent flow, on the other hand, occurs at high Reynolds numbers and produces random vortices and other flow fluctuations.

In pipe flows, Re <= 1500 usually indicates laminar flow. Let us take the biofluidic platform as an example to estimate the Reynolds number. The medium of biofluidics is usually water with ρ=1.0 x 10^3 *Kg* m^{-3} and μ=1.002 x 10^{-3} *N s/*m^2 (at 20°C). The velocity of the fluid flow does not normally surpass 10 *mm* sec^{-1}; the hydraulic diameter (*L*) [1] of the microchannel is usually not larger than 1.0 *mm*. By applying the abovementioned parameters into Eq. (1.1), the Reynolds number of this exemplary pipeline flow is Re ~ 10, indicating a laminar flow situation. In my experiments, both the flow velocity and the characteristic length scale are one or two orders smaller than the numbers given here. Hence, I would only need to focus on the behaviors of low Re flow.

The fact that microfluidics is usually described by low Reynolds numbers has significant implications. The well-predictable behavior of micro channel flow makes it easy to apply microfluidic technology to manipulate fluid and transport biological samples. That is to say, a great amount of time and labor can be saved from investigating the complexity of the fluid motion. This particular property of the micro flow is a fundamental driving force behind the proliferation of microfluidic research in various areas of biology and optics. Besides that, microfluidic devices certainly have a few other important advantages such as compactness, low cost and low sample consumption.

My research focuses on the development of optofluidic microscopy, where the microfluidics portion of the system is utilized for sample actuation. Therefore, I will describe a number of fluid actuation strategies that are popular among the microfluidic

community. I will only use the most simplistic models to describe the fundamental properties of each actuation scheme. Throughout our discussion, I will assume that the fluid we are studying is incompressible and Newtonian (Newtonian: the stress is proportional to the strain rate).

(1) Pressure driven flow

The behavior of a fluid, which is incompressible, Newtonian, isotropic, and obeys Fick's law of thermal conductivity, is governed by the Navier-Stokes equation, which actually represents the continuum version of F=ma on the basis of per-unit-volume [1, 2]

$$f - \nabla p + \mu \nabla^2 v = \rho \frac{\partial v}{\partial t} + \rho (v \cdot \nabla) v \tag{1.2}$$

$$\nabla \cdot v = 0 \tag{1.3}$$

which represents the conservation of momentum and mass, respectively. p is the pressure, f is the body force. The boundary conditions for such a fluid are usually no-slip, no temperature jump at the boundaries.

However, for low Reynolds number flow, the inertial effects, i.e. the right hand side of Eq. (1.2), are so small that they can be neglected. Then, the Navier-Stokes equation is further simplified:

$$f - \nabla p + \mu \nabla^2 v = 0 \tag{1.4}$$

Parallel flow (Fig. 1-1(a)) in long, straight micro channels is one of the most fundamental phenomena in microfluidics. Besides its simplicity, it has direct relevance to Optofluidic Microscopy, where stable sample delivery in straight channels is desirable. Therefore, I would like to use parallel flow to describe some of the most significant properties of pressure drive flow.

At the steady state, the parallel flow should be purely axial – only v_z is non-zero and v_z is a function of x and y, but not z. For circular cross section, where no external body force exists except a static pressure gradient, Eq. (1.4) can be readily solved [1],

$$v_z = \frac{-dp/dz}{4\mu}(R^2 - r^2) \tag{1.5}$$

$$\dot{Q} = \int v \cdot dA = \frac{\pi R^2}{8\mu}\left(-\frac{dp}{dz}\right) \tag{1.6}$$

where R is the radius of the circular channel; $\dot{Q}$ is the flow rate. Sample that travels in the micro channel tend to have the same velocity as the fluid in order to minimize the Stokes's drag (e.g. Eq. (1.7) for small spherical objects [1]) between the sample and the fluid. However, such an "equi-velocity" trend assumes that there is no other frictional force existing in the force diagram. In the case of *C. elegans* traveling in micro channel, such an "equi-velocity" condition may not hold. In this particular example, the nematode may also feel the drag force from the channel walls, which makes the worm travel slower than the fluid itself.

$$F = 6\pi\mu R v \tag{1.7}$$

Note that Eq. (1.7) only applied to a rigid and spherical object in Stokes flow. Modification to such a formula is required for real objects.

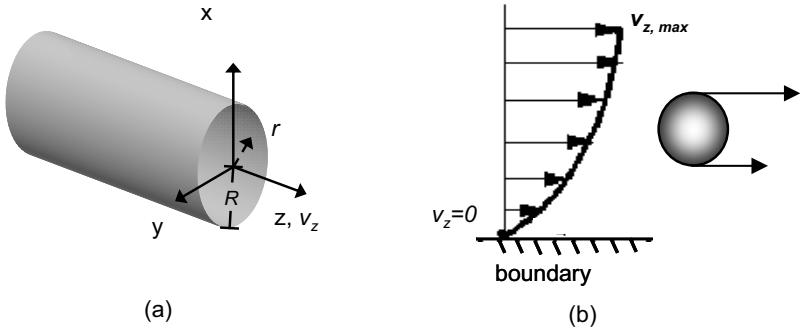

Figure 1-1: Pressure-driven flow in circular channel. (a) Geometry of the parallel flow. R: radius of the channel. (b) The velocity profile is parabolic for such an example of parallel flow.

There are a few key implications from the above equations, as technically they define the design rules of pressure-driven microfluidics. First, the velocity of the fluid flow is

proportional to dp/dz and thus, one can tune the velocity by controlling the pressure drop between the inlet and outlet of the micro channel. This type of fine-tuning can be readily accomplished by using a syringe pump, which usually has an accurate setting of flow rate. One such syringe pump is made by Harvard Instruments: Harvard Apparatus PicoPlus 11. Second, the flow profile is parabolic (Fig. 1-1(b)), indicating that the flow speed (v) is at maximum at the center of the channel, while v reduces to zero at the boundary. Therefore, a sample, such as a mammalian cell that is not flowing in the center of the channel, would see a velocity difference at its top and its bottom, as shown in Fig. 1-1(b). This velocity difference would give a torque to the sample, possibly causing it to rotate quickly. Thirdly, the central velocity is proportional to R^2. This second-order scaling law (Eq. (1.5)) points out that the highest fluid velocity that can be experimentally achieved drops very fast with the channel size. That is to say, the smaller (or narrower) the channel were, the lower the achievable velocity would be, when assuming the pressure gradient remains as a constant. It implies that high flow rate, i.e. high-throughput sample delivery, will be extremely difficult to accomplish in the regime of nanofluidics- the dimension of the channel is not larger than 100 nm. As such, fluidic actuation in the nanofluidic regime is often accomplished by electrokinetic pumping, which is independent of the size of the channel, as will be shown in Eq. (1.11).

(2) Electrokinetic pumping

We can roughly divide electrokinetics into two categories: electroosmosis, which refers to the motion of polar liquid, e.g. water, under the influence of electric field, and electrophoresis, which refers to the motion of a charged material, e.g. a biological cell, under the electric field.

When studying electroosmosis, we should first consider the behavior of polar liquid in contact with a planar wall. The surface charge of the wall influences the distribution of the ions inside the liquid but near the wall. Electric double layer (Fig. 1-2(a)), also called Debye's EDL [1] is subsequently formed at the interface of the liquid and the wall. By adopting the Gauss's law of electrostatics, the Boltzmann distribution of the energy levels

of the ions in the liquid, and a mean field approximation for the ions within the electric field, the electrical potential (φ) can be derived [2],

$$\varphi = \zeta \exp\left(-\frac{y}{\lambda_D}\right) \tag{1.8}$$

$$\zeta = \frac{q_0 \lambda_D}{\varepsilon_w} \tag{1.9}$$

$$\lambda_D = \left(\frac{\varepsilon_w k_B T}{2 n_0 e^2}\right)^{1/2} \tag{1.10}$$

where ζ is called the zeta-potential of the wall, which is determined by surface charge density (q_0), dielectric constant of the wall (ε_w), and Debye length (λ_D). Debye length in Eq. (1.10) depicts the effective thickness of the EDL. It can be seen from Eq. (1.8) that outside EDL, the electrical potential is close to a constant. Note that in order to obtain the above equations, it has been assumed that the thickness of EDL (i.e. the Debye length) is much smaller than the length scale of the channel. Fortunately, this assumption is usually valid as the Debye length is no larger than 10nm for most microfluidic systems, including Optofluidic Microscope (OFM).

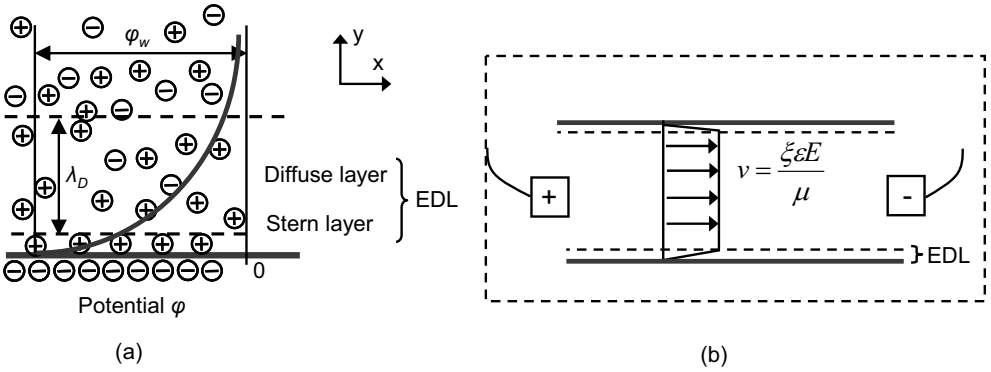

Figure 1-2: Electroosmosis. (a) The ion distribution inside the liquid that is near a charged surface. EDL is roughly divided into a Stern layer and a diffuse layer. (b) The velocity profile of electroosmosis. $v \propto E$ outside the EDL.

This electrical potential can be added to the Navier-Stokes equation (Eq. 1.4) as an external force ($\rho_E \cdot E$) to calculate the electroosmotic flow (EOF), when E is the electrical field applied along the direction of the long channel. After applying the appropriate boundary conditions, the velocity of EOF outside the EDL can be written as:

$$v_{EOF} = \frac{\xi \varepsilon E}{\mu} \tag{1.11}$$

which is linear to the applied electrical field, E (Fig. 1-2(b)) and is independent of the channel size.

The flat velocity profile of EOF can immediately benefit the OFM - the samples transported by electrokinetic pumping, in principle, would not rotate in the channel because the flow velocity is a constant outside the EDL. Note that pressure gradient and electroosmosis may both exist in an electrokinetic pumping experiment. Because of the linearity of the simplified Navier-Stokes equation (Eq. 1.4), the electroosmotic velocity derived here can directly be added to that obtained with pressure driven flow (Eq. 1.5) to find the collective results of the two forces.

On the other hand, electrophoresis studies the manipulation of samples through the use of the electrical field. The movement of a small spherical object in a low Reynolds number environment can be described as the balance between the viscous Stokes drag (Eq. 1.7) and the Coulomb force ($q_s \cdot E$) (Ref. [1]),

$$q_s \cdot E = 6\pi\mu R v \tag{1.12}$$

Note that q_s is the screened surface charge of the spherical sample, which can be calculated by using the same method that derives Eq. (1.8).

The size of the charged sample inside the fluid can be very different. It could be much larger than λ_D, such as a micron-sized latex sphere; or the size of the object can be much smaller than λ_D, such as nanoparticles. However, in both limits, the resulting electrophoretic (EP) velocity of the sample is proportional to $\frac{\xi \varepsilon E}{\mu}$ (see Chapter 2 of ref. [1]), assuming that the object is not in the vicinity of the charged wall surface. Note that

zeta potential (ζ) here is the property of the sample surface, rather than that of the microfluidic wall as in Eq. (1.11).

Sample manipulation by using electrokinetic pumping is popular among the microfluidic community as electrokinetics utilizes surface forces, which scale well with channel's length scale. When the size of the channel gets to the level of 100 nanometers, electrokinetic pumping will be more effective than pressure gradient pumping. In addition, the components of the electrokinetic pump, such as the microelectrode arrays, are easy to integrate into a microfluidic system, so that the entire microfluidic system can be made compact and energy-efficient.

In the end, I want to point out that when drawing the simple conclusions in (1) pressure driven flow and (2) electrokinetic pumping, I have assumed that the object immersed in the liquid medium is far away from the channel wall and the object is perfectly rigid without any deformation caused by the fluid field. The situation would get much more complicated when the size of the object is comparable with the fluidic channel and/or the object is very close to the channel wall. Curious readers can read Ref. [2-4] and their cited literature in order to get more insight about flow or diffusion behavior of the object in the near-wall situation.

(3) Dielectrophoeresis and other actuation schemes

Dielectrophoresis (DEP) deals with the motion of polarizable particles, like cells, subject to a non-uniform AC electrical field. It has becomes quite popular lately because of its capability of trapping nanometric particles within very confined geometry, e.g. smaller than 1 micron. A polarized particle can be approximated as a summation of electric dipoles, whilst the description of the dielectrophoresis of dipoles can be accurate. When using an electrostatic approximation, the time-averaged DEP force can be expressed as follows [1, 5],

$$\left\langle F_{DEP}(t)\right\rangle = 2\pi a^3 \varepsilon_m \,\mathrm{Re}\big(K(\omega)\big)\nabla\left|E_{rms}\right|^2 \tag{1.13}$$

$$K(\omega) = \frac{\varepsilon_p - \varepsilon_m}{\varepsilon_p + 2\varepsilon_m} \tag{1.14}$$

where a is the radius of the particle; $\nabla|E_{rms}|^2$ is the gradient of the square of the rms electrical field. The Clausius-Mossotti factor, $K(\omega)$, is determined by the complex permittivity of the particle (ε_p) and the medium (ε_m). The sign of the real part of $K(\omega)$ determines whether the DEP force is toward the higher field intensity or away from it. For DEP trapping, $\mathrm{Re}(K(\omega))$ needs to be larger than zero; in such a case, the particles move toward the fabricated electrodes, near which the electrical field is highly concentrated, i.e. higher $\nabla|E_{rms}|^2$. Although DEP force has a short working range, it has also been demonstrated in transporting particles in a long distance. In DEP transportation experiments, inter-digitated microelectrode array is fabricated underneath the fluidic channel; the samples start to move when the individual microelectrode turns on and off inter-digitally. This phenomenon is somewhat similar to peristaltic pumping.

Recently, optical tweezers have drawn lots of attention within the microfluidics community due to their superior ability to position and control objects beyond the capability of other sample actuation means. Under the dipole approximation, the gradient force applied on the object is similar in expression as the DEP situation, in the sense that any object with a larger refractive index than that of the medium prefers to move toward higher intensity, i.e. larger ∇I_{laser}. More details of employing optical tweezer actuation in microfluidics will be given in Chapter 7, which reports on our development of the first optical-tweezer actuated OFM.

Electrowetting is probably one of the simplest means of driving microfluidic motion [2]; it works by modifying the surface tension between the solid phase and the liquid phase, i.e. $\gamma_{sl}{}^{o} \rightarrow \gamma_{sl}{}^{o} - \frac{CV^2}{2}$, where γ_{sl} refers to the surface tension at solid-liquid interface; $C = \frac{\varepsilon_r \varepsilon_o}{t}$ refers to the capacitance at the interface for a uniform dielectric of thickness t; and V is the applied voltage.

As such, the modified Young-Dupre equation, or say Lippmann's equation [2] is

$$\gamma_{gl} \cos\theta = \gamma_{sl}{}^{o} - \frac{CV^2}{2} - \gamma_{sg} \tag{1.15}$$

where θ is the contact angle.

When a potential difference is applied between the droplet and the substrate, the droplet starts to spread on the surface and lower the contact angle. It is said that droplet manipulation by using electrowetting can be as fast as 1 *mm/s* [2]. As such, samples or reaction agents encapsulated in an electrolytic droplet can possibly move at high speed on the surface of the substrate. However, electrowetting may suffer from electrolysis or excessive Joule heating.

Besides the abovementioned methods, another few microfluidic actuation schemes will probably benefit optofluidic applications. These schemes include but are not limited to optoelectronic tweezers [6], photo-thermal fluidic pumping [7], magnetic tweezers [8], and thermo-capillary actuation [9].

1.2 Microfluidic detection, sensing and imaging using optical means

Microfluidic detection is of significant use. For example, microfluidic mixing needs to be visualized in an easy-to-understand format, so that fluid physicists can investigate the pattern and the dynamics of the mixing process. As such, an appropriate detection method has to be employed which does not interrupt with the natural dynamic evolution of the fluidic mixing. In addition, data obtained from microfluidic detection is important in analyzing chemical reactions, development of biological cells, etc.

Microfluidic detection can be achieved in various ways that can make use of impedance change, temperature change, change in optical signals, etc. In this section, I will only focus on optical detection methods that have been massively employed in microfluidic systems.

There are many aspects of light that can be targeted as a detection subject. Accessible optical information includes intensity of light as in bright field microscopes, phase change of light as in optical interferometers, and the angular spectrum of the scattered light. Furthermore, nonlinear optical signals, such as fluorescence, second harmonic waves, and Raman scattering signals add another dimension to the field of optical detection. One major advantage of using nonlinear optics is that the acquired data have excellent contrast and are easy to visualize because light at the fundamental wavelength (λ_0) can be very efficiently filtered out of the acquired data.

An exhaustive summarization of all the optofluidic detection methods is impractical considering the length of my thesis. As a result, I will concentrate on only a few examples of lab-on-chip detection schemes. Alongside, some of the fundamental properties of optofluidic detection will be discussed.

The first example is particle image velocimetry (PIV). PIV, as the name suggests, measures the velocity of the particles seeded in the fluid by using the time-lapse images of the particles. A PIV system takes two images shortly after each other and then calculates the distance individual particles traveled within this time. By knowing the time difference and the measured displacement, the velocity is calculated in the end. This technique can have both a high temporal resolution (~10 ns) and a high spatial resolution (~1 μm). The equipment required by a basic PIV system is similar to an optical microscope, except that a "light-sheet" illumination is needed in PIV [10]. As there are still many poorly understood aspects of microfluidics, such as micro-mixing, the PIV techniques will certainly benefit the development of novel microfluidic systems.

Cell sorting technology has significant applications in a number of fields, including molecular biology, immunology, and marine biology. In the field of molecular biology, it is especially powerful when used with fluorescence tagged antibodies. Cell sorting used to reply on expensive flow cytometers, but there has been major progress toward the low-cost flow cytometers. In 2000, Quake group, then in Caltech, announced the first microfabricated fluorescence activated cell sorting (FACS) device based on microfluidics [11]. The fluorescence signals recorded within the detection window (Fig. 1-3(a)) can be used to determine whether the cell sample should be collected for later use or dumped as waste. This cell sorting device is small and disposable. More importantly, various pressure-switch schemes can be accommodated to this microfluidic FACS system and will dramatically improve its cell sorting efficiency.

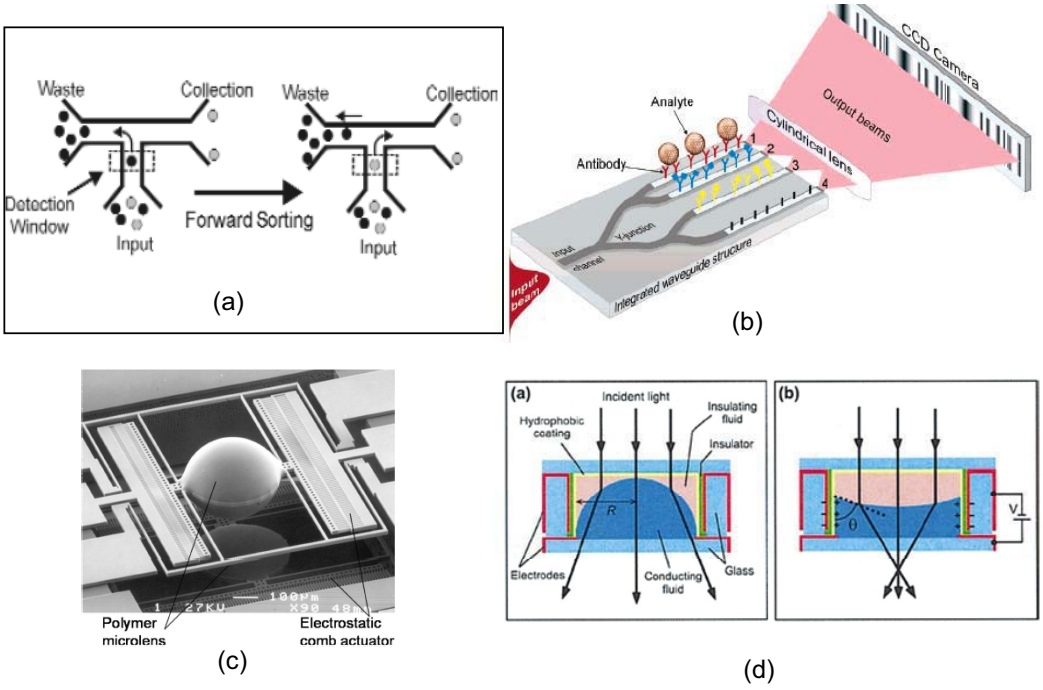

Figure 1-3: Examples of optofluidic sensing or imaging devices. (a) Micro-FACS. The appearance of fluorescence signals at the 'detection window' triggers the opening of the collection reservoir. Reprint permission from Ref. [11]. (b) Microfabricated Young's interferometer sensor was used in virus detection. **1**, **2**, and **3** indicate the measuring channels, and **4** is the reference channel. Reprint permission from Ref. [14]. (c) Microfabricated confocal microscopy by using MEMS technology. Two micro-lens scanners are orthogonally aligned and vertically stacked. Reprint permission from Ref. [15]. (d) Electrowetting enabled tunable lenses for cell phone cameras. Schematic shows the cross section of a liquid-based variable lens in a cylindrical glass housing. The transparent electrodes are formed of 50-nm-indium tin oxide; the insulator is a 3-mm-parylene-*N* layer. Reprint permission from Ref. [16].

Optical interferometer has an extraordinarily high signal-to-noise ratio (SNR), and thus is able to measure very subtle signal changes. For example, optical interferometers are often used to measure the phase change of the optical signals with extremely high accuracy. This unique property of interferometric detection has been used in affinity-based

biosensing. That is to say, the attachment of molecules, such as proteins, onto one arm of the sensor surface will cause a miniscule change in the refractive index of the arm, which is expressed as a tiny drift of the light phase. Optical interferometry can measure the phase drift, and subsequently the change in refractive index (Δn) down to a high level (e.g., $\Delta n \sim 10^{-6}$ in [12], $\Delta n \sim 10^{-8}$ [13]). Recently, Ymeti et al. [14] reported on an integrated Young's interferometer sensor that was applied to detect HSV-1 virus (Fig. 1-3(b)). This integrated device represents a broad range of micro interferometers that can make biosensing much cheaper and more compact compared with a lab-bench system.

The microscope objective lens is arguably the most critical component of an optical microscope. As such, investigation into microfabricated lenses will certainly enable miniaturized optical microscopes. In fact, a range of compact lenses have also been designed by groups around the world. For example, Luke P. Lee's group [15] developed a micromachined confocal microscope that was enabled by electrostatic actuation of two polymer micro lenses (Fig. 1-3(c)). This technology will potentially make possible the integration of a confocal microscope array onto a single chip. However, very sophisticated fabrication technology will be required in order to design a miniaturized objective lens and match the imaging quality of a regular microscope objective. In 2004, Philips Research announced one of the first microfluidic optical lenses (Fig. 1-3(d)) [16]. The device made use of the electrowetting effect, that is, the shape of an oil-water interface was modulated through electrical manipulation of the contact angle. This liquid lens is particularly useful in electronic devices such as cell phone cameras, where the demand on image quality is not so stringent.

1.3 Nanoapertures and their applications

Nanoapertures (or nanoholes) refer to subwavelength apertures with diameters on the order of a hundred nanometers. There is very limited literature about nanoaperture in the range of 10 nm. Technically speaking, smaller nanoapertures are difficult to fabricate and subsequently give very limited improvement in performance, such as resolution or light confinement because the transmission through a sub-50nm aperture is awfully weak

and/or, in many cases, the existence of surface plamson waves makes the effective optical size of the nanoaperture much larger than its physical size.

Bethe was probably the first to study nanoapertures in optics. In his original paper in 1944 [17], he theoretically calculated the transmission through the nanoaperture that was drilled in an infinitely thin but perfect conductor. Bethe's model predicted that the transmission power after being normalized by the aperture's area scaled as $\left(D/\lambda\right)^4$, where D is the aperture diameter, and λ is the wavelength. Later on, Bouwkamp [18] improved Bethe's result by deriving additional terms for the expansion, whose first three terms may be written as [18, 19],

$$\frac{T}{D^2} = \frac{64}{27\pi}\left[\frac{(kD)^4}{2^6} + \frac{22}{25}\frac{(kD)^6}{2^8} + \frac{7312}{18{,}375}\frac{(kD)^8}{2^{10}}\right] \tag{1.16}$$

Where T is the transmission coefficient [17, 18]; and k is the wave vector. Note that the derivation of such a relation was based upon a square aperture with dimensions D x D illuminated by a plane wave at normal incidence. The results for a circular aperture can also be found in Bouwkamp's classical paper [18].

Nanoapertures are known to possess interesting optical properties. Near-field light components, normally too weak or say "too evanescent" to be detectable, are scattered by the nanoapertures and become discernible with a far field detector. For example, a nanoaperture based near field microscope can render a high resolution far beyond the diffraction limit [20].

More recently, there is a seminal work done by Ebbesen et al. [21], which for the first time connected surface plasmon waves with the 2D nanoaperture array. It was discovered that transmission through a tightly-spaced nanoaperture array could be dramatically enhanced compared to the summation of that of all the individual and isolated nanoapertures.

While there is steady progress in understanding the anomalous transmission and diffraction properties of nanoapertures, they have drawn tremendous attention on the application side. A large variety of devices has been demonstrated with remarkable improvements in device performance, such as biosensing, laser technologies, and

photolithography. Therefore, I will devote this section of my thesis to the overview of the applications of nanoapertures that are closely relevant to lab-on-a-chip and optofluidics.

The first example focuses on specially engineered non-circular nanoapertures. Although circular nanoapertures can render a superior high resolution when used in imaging or sensing, they also suffer from exceedingly weak transmission. For example, transmission through a 30nm aperture is three orders-of-magnitude weaker than that through a 100nm aperture.

Such a weak signal issue requires that, in practice, either the acquisition time needs to be elongated or an ultra sensitive detector is necessary. Consequently, the increased consumption in time and cash really limit the ultimate usefulness of the nanoapertures. Therefore, a few labs have been working on innovative nanoaperture designs in order to enhance the transmission without necessarily enlarging the region, within which the light is confined. Hesselink's group in Stanford and Xu's group in Purdue are two of the pioneers in designing C-shaped [22, 23] or H-shaped [23] nanoapertures with enhanced optical transmission. The three-orders-of-magnitude improvement in transmission and 0.1λ confined spot size [22] were contributed by both the propagation modes from these so called "optical ridge-waveguides" structure and local surface plasmons around the aperture. On the application side, such "optical ridge-waveguides" have proved to be useful in improving the performance of photo-detectors (Fig. 1-4 (a)) [24], very small aperture lasers [25], and lithography technology.

Note that both papers have claimed that the reduced spot size of such non-circular apertures could improve the spatial resolution of near field microscopy. Nevertheless, the asymmetrical nature of this kind of apertures may generate image distortions if the optical response of such a nanoaperture structure differs dramatically for TE and TM polarizations. So far, there seems to be no or very little literature that has convincingly demonstrated the effectively of a near field imaging system through the use of such non-circular apertures.

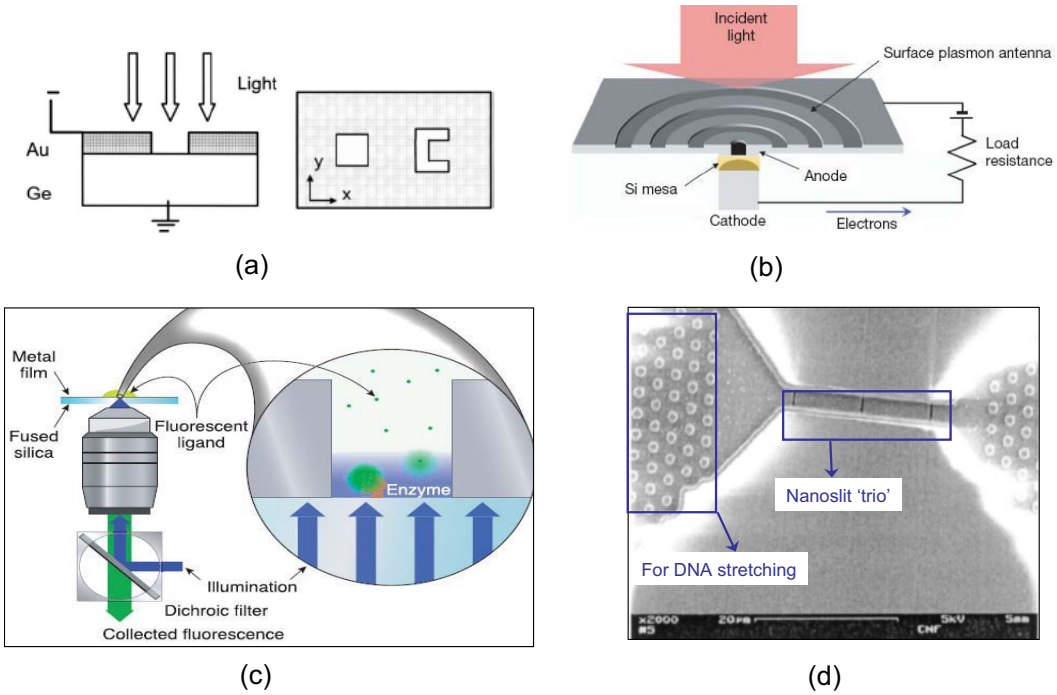

Figure 1-4: Examples of nanoaperture assisted devices. (a) Germanium photodetector improved by "optical ridge-waveguide", i.e. the "C" aperture. The apertures are formed in a Au film on top of a Ge substrate. The device is reverse-biased, and it functionsas a Schottky diode. Reprint permission from Ref. [24]. (b) Nano photodiode with a surface plasmon antenna. Reprint permission from Ref. [28]. (c) Zero-mode waveguide for spectroscopy applications. Reprint permission from Ref. [29]. (d) Nanofluidic near field scanner for DNA measurement. SEM image shows three 100 nm wide slits and hydrodynamic channels nanofabricated into an etched quartz structure. Reprint permission from Ref. [30].

Numerous studies on a single nanoaperture surrounded by periodical corrugated surfaces [26] or a tightly-spaced nanoaperture array [21] were reported in the recent past. The results suggest that the surface plasmon waves confined on the metallic surface were able to channel the light through the nanoapertures and dramatically improved the optical

transmission. It was indicated that the interplay between light and surface plasmon would not have occurred unless the condition of conservation of momentum was satisfied, i.e.

$$K_{sp} = K_{//} \pm G \tag{1.17}$$

where K_{sp} is the momentum of surface plasmon waves; $K_{//}$ is the component of the incident wave-vector in the plane of the nanoaperture array; and G represents a series of the reciprocal wave-vectors provided by the periodic surface corrugation or the nanoaperture array lattice. There is an excellent review article in Nature [27] that summarizes the potential applications of the nanoaperture array in numerous areas, such as optoelectronics (Fig. 1-4(b), also from Ref. [28]).

Moreover, in many occasions, even a single and isolated aperture could be of significant use. As the tiny nanoaperture does not support any waveguide modes, optical waves are largely confined within a femtoliter volume. It has been reported that the fluorescence intensity inside confined geometry is markedly enhanced due to an increase of the excitation wave and the reduction of the fluorescence lifetime within a nanoaperture. Michael Levene and his colleagues [29] successfully applied such an isolated nanoaperture in fluorescence correlation spectroscopy (Fig. 1-4(c)), which is a powerful technique to study the diffusion and reaction rate of single biomolecules. One major advantage of such a "zero-mode waveguide" is that it allows for the study of biophysical events of the molecules at their normal physiological conditions, i.e. millimolar concentration. Nevertheless, most of the then-existing single molecule studies required the dilution of the biomolecules solution down to pico- or nano-moles.

The last example of the nanoapertures will look at the application of "nano-slits", rather than circular nanoapertures. Circular nanoapertures have proved to be powerful in rendering superior resolution in optical imaging; however, taking images is not always necessary. Nanoslit, being one dimension reduced from a circular nanoaperture, can act as a high-resolution "nanoruler" that can be used to measure the distance between closely spaced fluorescence molecules on a long DNA strand or can count the newly divided cells inside a large microorganism. J. O. Tegenfeldt et al. [30] successfully combined the nanoslits with electrokinetically actuated microfluidics and demonstrated their

preliminary work on measuring the length of uncoiled DNA molecules (Fig. 1-4(d)). Their achieved resolution of 200 nm was a clear indication that nanoslits are able to render a high resolution beyond the diffraction limit.

Concluding remarks of this chapter

Both microfluidics and nanoapertures have drawn tremendous interest within the research community. The enormous advantages brought with microfluidics can perfectly combine with the unique properties of nanoapertures thanks to the planar nature of the fabrication technology involved. There have been preliminary research results showing the vast potentials of microfluidic based nanoaperture devices in numerous applications areas in biology, and I have briefly listed a few of them. OptoFluidic Microscopy, which will be discussed in details for the rest of my thesis, is certainly an excellent example of the perfect fusion of microfluidics and nanoapertures.

References

1.N. T. Nguyen, and S. T. Wereley, *Fundamentals and Applications of Microfluidics* (Artech House, 2002).
2.T. M. Squires, and S. R. Quake, "Microfluidics: Fluid physics at the nanoliter scale," Reviews of Modern Physics **77**, 977-1026 (2005).
3.R. F. Ismagilov, A. D. Stroock, P. J. A. Kenis, G. Whitesides, and H. A. Stone, "Experimental and theoretical scaling laws for transverse diffusive broadening in two-phase laminar flows in microchannels," Applied Physics Letters **76**, 2376-2378 (2000).
4.A. E. Kamholz, and P. Yager, "Molecular diffusive scaling laws in pressure-driven microfluidic channels: deviation from one-dimensional Einstein approximations," Sensors and Actuators B-Chemical **82**, 117-121 (2002).
5.W. M. Arnold, "Positioning, levitation and separation of biological cells," in *Electrostatics 1999*(1999), pp. 63-68.
6.P. Y. Chiou, A. T. Ohta, and M. C. Wu, "Massively parallel manipulation of single cells and microparticles using optical images," Nature **436**, 370-372 (2005).
7.G. L. Liu, J. Kim, Y. Lu, and L. P. Lee, "Optofluidic control using photothermal nanoparticles," Nat Mater **5**, 27-32 (2006).
8.H. Lee, A. M. Purdon, and R. M. Westervelt, "Manipulation of biological cells using a microelectromagnet matrix," Applied Physics Letters **85**, 1063-1065 (2004).
9.A. A. Darhuber, J. M. Davis, S. M. Troian, and W. W. Reisner, "Thermocapillary actuation of liquid flow on chemically patterned surfaces," Physics of Fluids **15**, 1295-1304 (2003).

10.R. J. Adrian, "Twenty years of particle image velocimetry," Experiments in Fluids **39**, 159-169 (2005).
11.A. Y. Fu, C. Spence, A. Scherer, F. H. Arnold, and S. R. Quake, "A microfabricated fluorescence-activated cell sorter," Nature Biotechnology **17**, 1109-1111 (1999).
12.T. Allsop, R. Reeves, D. J. Webb, I. Bennion, and R. Neal, "A high sensitivity refractometer based upon a long period grating Mach-Zehnder interferometer," Review of Scientific Instruments **73**, 1702-1705 (2002).
13.J. Zhang, Z. H. Lu, B. Menegozzi, and L. J. Wang, "Application of frequency combs in the measurement of the refractive index of air," Review of Scientific Instruments **77** (2006).
14.A. Ymeti, J. Greve, P. V. Lambeck, T. Wink, S. van Hovell, T. A. M. Beumer, R. R. Wijn, R. G. Heideman, V. Subramaniam, and J. S. Kanger, "Fast, ultrasensitive virus detection using a young interferometer sensor," Nano Letters **7**, 394-397 (2007).
15.S. Kwon, and L. P. Lee, "Micromachined transmissive scanning confocal microscope," Optics Letters **29**, 706-708 (2004).
16.S. Kuiper, and B. H. W. Hendriks, "Variable-focus liquid lens for miniature cameras," Applied Physics Letters **85**, 1128-1130 (2004).
17.H. A. Bethe, "Theory of diffraction by small holes," Physical Review **66**, 163-182 (1944).
18.C. J. Bouwkamp, "Diffraction theory," Reports on Progress in Physics XVIII, 35 (1954).
19.T. Vallius, and J. Turunen, "Transmission through single subwavelength apertures in thin metal films and effects of surface plasmons," Journal of the Optical Society of America a-Optics Image Science and Vision **21**, 456-463 (2004).
20.D. Courjon, *Near-field microscopy and near-field optics* (London: Imperial College Press, 2003).
21.T. W. Ebbesen, H. J. Lezec, H. F. Ghaemi, T. Thio, and P. A. Wolff, "Extraordinary optical transmission through sub-wavelength hole arrays," Nature **391**, 667-669 (1998).
22.X. L. Shi, L. Hesselink, and R. L. Thornton, "Ultrahigh light transmission through a C-shaped nanoaperture," Optics Letters **28**, 1320-1322 (2003).
23.E. X. Jin, and X. F. Xu, "Obtaining super resolution light spot using surface plasmon assisted sharp ridge nanoaperture," Applied Physics Letters **86** (2005).
24.L. Tang, D. A. B. Miller, A. K. Okyay, J. A. Matteo, Y. Yuen, K. C. Saraswat, and L. Hesselink, "C-shaped nanoaperture-enhanced germanium photodetector," Optics Letters **31**, 1519-1521 (2006).
25.F. Chen, A. Itagi, J. A. Bain, D. D. Stancil, T. E. Schlesinger, L. Stebounova, G. C. Walker, and B. B. Akhremitchev, "Imaging of optical field confinement in ridge waveguides fabricated on very-small-aperture laser," Applied Physics Letters **83**, 3245-3247 (2003).
26.H. J. Lezec, A. Degiron, E. Devaux, R. A. Linke, L. Martin-Moreno, F. J. Garcia-Vidal, and T. W. Ebbesen, "Beaming light from a subwavelength aperture," Science **297**, 820-822 (2002).
27.C. Genet, and T. W. Ebbesen, "Light in tiny holes," Nature **445**, 39-46 (2007).
28.T. Ishi, J. Fujikata, K. Makita, T. Baba, and K. Ohashi, "Si nano-photodiode with a surface plasmon antenna," Japanese Journal of Applied Physics Part 2-Letters & Express Letters **44**, L364-L366 (2005).
29.M. J. Levene, J. Korlach, S. W. Turner, M. Foquet, H. G. Craighead, and W. W. Webb, "Zero-mode waveguides for single-molecule analysis at high concentrations," Science **299**, 682-686 (2003).
30.J. O. Tegenfeldt, O. Bakajin, C. F. Chou, S. S. Chan, R. Austin, W. Fann, L. Liou, E. Chan, T. Duke, and E. C. Cox, "Near-field scanner for moving molecules," Physical review letters **86**, 1378-1381 (2001).

Chapter 2

THEORY OF OPTOFLUIDIC MICROSCOPY

Optofluidic Microscopy (OFM) combines advanced microfluidic technologies and the nanoaperture-based imaging technique to produce a "microscope-on-a-chip". Unlike conventional microscopes, OFM does not require the use of an objective lens. Nor does OFM need sophisticated machinery for sample actuation and feedback control, which is always necessary for a commercial near-field optical microscope. In this chapter, I will first introduce the fundamental concepts of conventional microscopy and near field microscopy. After that, I will explain in details the working principles of OFM. In the discussion, the relationship and difference of the abovementioned imaging techniques will be highlighted. At the end, I will introduce a few designs of OFM that either have already been implemented or should be implementable in near future.

2.1 Overview of conventional microscopy and near field imaging

1) Basic concepts of conventional microscopy

Microscopic objects are usually too small to be seen with naked eye. Conventional microscopes are optical instruments that can produce magnified images, real or virtual, of objects. Therefore, the conventional microscope must accomplish two tasks: produce a magnified image of the specimen, and render the details in a way that human eyes or a photo detector (e.g., camera) can read or record.

Since the invention of the optical microscope in the late 1600's, a large variety of microscope architectures has arisen. In terms of specialized microscopy functionalities, there are dark-field, confocal, phase-contrast, fluorescence, etc. In terms of the distance of the image, there are the finite optical system and infinity-optics system. However, the fundamental properties of a microscope have not undergone much change. For example,

the objective lens, as the most important microscope component, still plays the major role in image formation and determining the image quality. Therefore, it is quite straightforward to lay out a few important properties of a conventional microscope. Here I would like to discuss them within the frame of infinity-optics system.

Such a microscope system (Fig. 2-1) usually includes an illumination source, such as a lamp or a laser, a microscope objective, a tube lens, and a sensitive camera (or other recording media). During image formation, the object of interest is placed on the focal plane of the objective lens. In an infinity-corrected optical system, the exit light rays after the objective lens are made up of plane waves with a focal point in the infinity. In this case, a tube lens (or say a camera lens) is necessary to re-focus the light and form an image. On the image plane, we normally place a high-quality camera (Fig. 2-1) and then read the images on a computer screen.

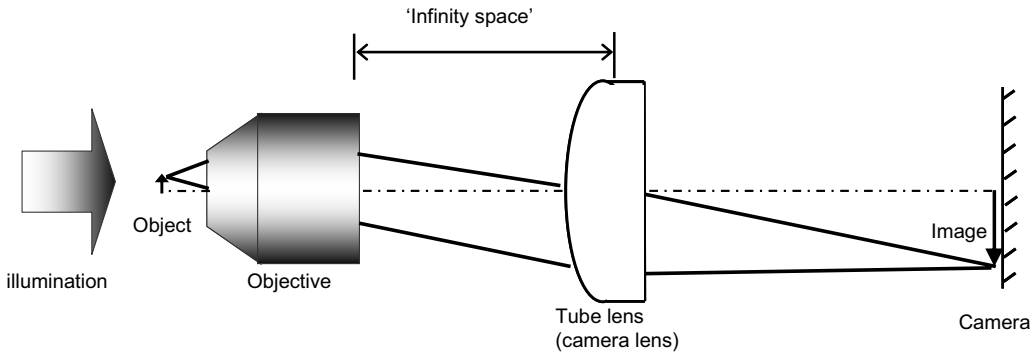

Figure 2-1: Illustration of an infinity-optics system. The object is located on the focal plane. The output from the objective lens is made up of plane waves. "Infinity space" is the space between the objective lens and the tube lens, between which various optical components can be inserted.

The calculation of magnification (M) in the case of infinity-corrected optics is simple. In fact, M is the ratio between the focal length of the tube lens and that of the objective lens. For example, later shown in my optical tweezer setup (Chapter 7), I used a 200mm tube lens and a 40X objective that has a focal length of 4.5 mm. Therefore, the achieved

magnification, M= 200mm/4.5mm ~ 44. Usually a 100X objective lens can magnify the object by 100 folds, and thus enables the study of the real sub-micron details of the object.

One major advantage of an infinity-corrected system over its finite-optics counterpart is that numerous auxiliary components, such as waveplates, pinholes, and polarizers, can be inserted into "the infinity space" (see Fig. 2-1) without having to worry about the possibility of any spatial shift or directional change of the light ray. Thereafter, over the past two decades, all the major microscope manufacturers have gradually migrated to the deployment of infinity optical systems when producing research-grade microscopes.

The resolution of a conventional microscope impinges on the so-called diffraction limit, which arises from the size of the spot that a light beam can be focused to with normal lens elements. At the focal point, the beam forms a symmetric pattern of concentric rings known as the Airy disk pattern, which was first described in detail by Ernst Abbe in 1873. The Airy disk can be fully formulated using the scalar diffraction theory [1].

The distance, *R,* from the highest intensity point located in the middle of the center spot to the first node in intensity is given by

$$R = \frac{0.61\lambda}{NA} \tag{2.1}$$

where λ is the wavelength; *NA* is the numerical aperture of the objective lens. Mathematically, under Rayleigh's criterion [2], *R* denotes the resolution limit of such a lens-based imaging system.

Theoretically, *NA* should always be smaller than 1.0, and the resolution of a conventional microscope under visible light illumination would not be much better than 250 nm. However, the appearance of oil- or water-immersion lenses and the development of shorter illumination wavelength have successfully pushed this resolution limit really close to the level of 100 nm, although such a high resolution, in practice, is not usually obtained. Later on it will be shown that near field imaging based on nanoapertures can beat the resolution limit determined by diffraction theory. In addition, a few groups have demonstrated ways of getting around the resolution barrier with conventional fluorescence microscopy [3, 4].

In the end, I should mention that although conventional microscopes are able to render good image resolution, they normally could not resolve near transparent objects such as

biological cells. That is the primary reason behind the invention of a variety of contrast enhancement mechanisms, such as differential interference contrast (DIC)

2) Basic concepts of near field scanning optical microscope (NSOM)

The concept of near field optical microscopy was first outlined by E.H. Synge in 1928. However, it took almost another 60 years to realize such a system in the spectrum of visible light, due to a variety of technological obstacles. Even nowadays, a commercial NSOM system is still a complicated and expensive piece of instrument.

However, the operation motif of a near field microscope is quite simple: to transfer the near-field components of the light from the object into far field components in such a way that a normal detector can readily detect them. In essence, it is a photon tunneling process, during which a non-propagating wave is modified into a propagating wave.

The image formation procedure can be explained with an illumination type of NSOM (Fig. 2-2 (a)). Here, the illumination light is coupled into the tiny nanoaperture probe, which remains in the near-field proximity with the sample surface throughout the scanning process. Such a tiny probe has a localized light profile (~50 nm), which is 5-10 times smaller than the focal spot of an objective lens. Thus, such a nanometric probe is able to differentiate miniscule structures that are extremely close to each other. Such a near field imaging technique will be more clearly explained with an example on Page 70 of Chapter 5. A more thorough investigation of a 2-dimensional NSOM can be found in Ref. [5] that included detailed explanations of the imaging properties of NSOM, such as resolution, contrast, polarization, etc.

The majority of the light components of the NSOM probe are near field, i.e. evanescent wave components. However, the near field light components when meeting with the sample surface are scattered by the structures on the sample surface and then transformed into propagating components.

In transmission-type NSOM, the scattered light from the sample surface is collected normally by a good microscope objective; it is then recorded by a sensitive photodetector, such as a photomultiplier tube. Note that similar to laser scanning confocal microscopy, a NSOM system utilizes a point-by-point scanning mechanism. That is to say, it is not a full

field imaging method. In such a case, a camera even if it is sensitive enough is not necessary. Instead, we usually use a single-point detector like faster PMTs as the recording medium as it usually has a higher recording speed.

Besides the illumination mode NSOM, there is also a collection-mode one: the sample is illuminated by plane wave, and then the light being scattered off the sample surface is collected by a NSOM probe. Note that both imaging modes will be discussed in more detail in Chapter 5 and Chapter 6, as their image formation principle is the backbone of our initial OFM prototype.

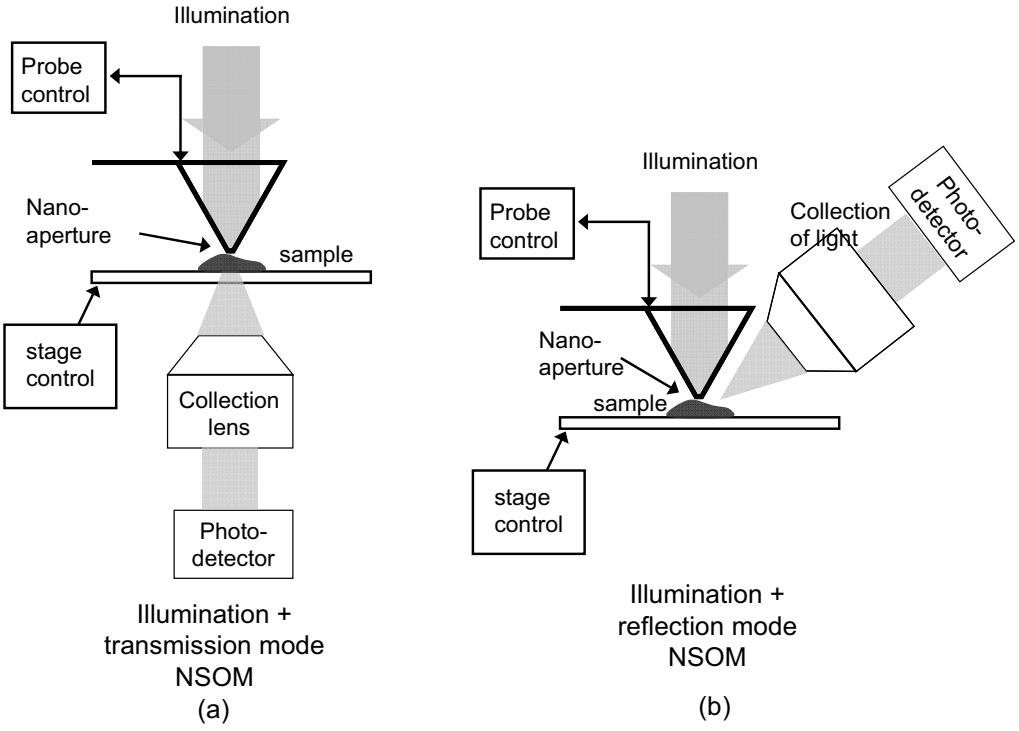

Figure 2-2: Illustration of near field scanning microscopy (NSOM). (a) Illumination + transmission mode: the NSOM probe provides illumination; transmission from the sample surface is recorded. (b) Illumination + reflection mode.

It is also worth noting that in the transmission mode NSOM systems, the nanoaperture probe and the collection optics are on different sides with respect to the sample location. Therefore, in applications such as imaging non-transparent samples or thick samples, this transmission type of NSOM may be too difficult to implement. On the other hand, there is another class of imaging modality: reflection mode NSOM (Fig. 2-2(b)), where the reflection from the sample is collected.

The evanescent field does not propagate in the classical sense to obey refraction, diffraction or reflection behaviors. As such, evanescent waves do not obey the diffraction theory that commonly describes the normal propagation waves. Therefore, many classic conclusions drawn from the traditional diffraction theory do not apply in the study of evanescent waves, for example, Eq. (2.1): the resolution limit imposed by the optical diffraction.

In general, the resolution limit specified by the diffraction barrier can be bypassed by near field microscopes. The achievable resolution for both NSOM operation modes, in theory, is the same, i.e. equal to the size of the probe (D) but independent of the wavelength. For example, a 50nm nanoaperture with a 650 nm laser source should be able to deliver a resolution as high as 50nm, which is far beyond the range of a conventional microscope. However, further reduction of the probe size might prove to be fruitless. Due to the existence of local surface plasmon waves at the periphery of the NSOM aperture, the effective size of the nanoaperture, i.e. the resolution of aperture-based NSOM will not be better than 30 nm, empirically speaking. Having said that, there are certainly noel ways to circumvent such a restriction imposed by surface plasmon waves, among which aperture-less NSOM is an excellent example. Aperture-less NSOM makes use of the tip-enhanced near field component to discover nanostructures with $\leq$ 10 nm resolution [6].

A near field microscope usually has an extremely short depth of field. Thereafter, during a NSOM scan, it is always required that the nanoaperture probe should be extremely close (preferably less than 20 nm) to the surface of the sample. Thereafter, a commercial NSOM system, without exception, utilizes a feedback control system for this purpose. One control mechanism is to monitor and maneuver the Van der Waals force between the sample surface and probe. That is to say, the tiny change of the sample-probe separation will

generate a large modification of the Van der Waals interaction between them, thus causing either a large frequency change of a vibrating probe (Fig. 2-3 (a)) or a large deflection of a static cantilever probe (Fig. 2-3 (b)) [7].

In terms of feedback implementation, there have been varieties of control modes, such as constant height mode or constant force mode. The probe can work at either DC mode such as a cantilever or AC (i.e. oscillatory) mode. As such, monitoring of the displacement of the tip can be accomplished by employing an AFM-type of deflection laser or using a vibrating tuning fork. Technologically speaking, feedback control system is the most sophisticated and critical part of a NSOM system, which has probably hindered the proliferation of the near field microscope. In the rest of chapter, I will explain how OFM can alleviate the needs of an expensive feedback control system without sacrificing too much of the image quality.

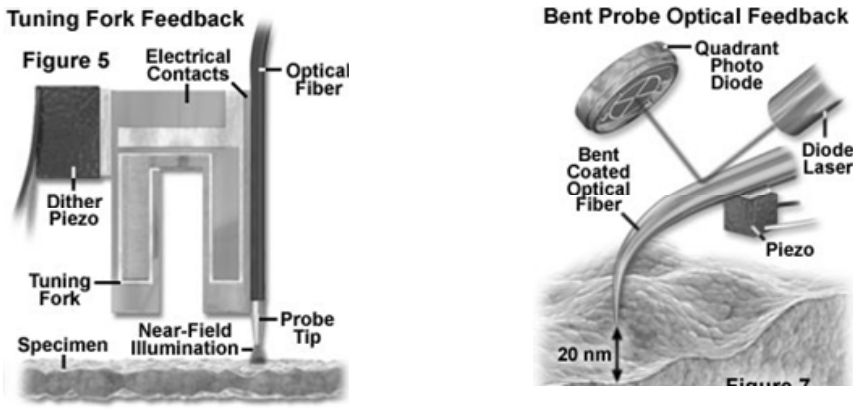

Figure 2-3: Two feedback control mechanisms that are widely applied in NSOM. (a) Tuning Fork Feedback: both amplitude and frequency of the oscillating probe is monitored. (b) Bent Optical Fiber Feedback: deflection of the neck of the probe is monitored.

At last, I will introduce a different type of near field microscopy method, total internal reflection fluorescence microscope (TIRFM), as it has become increasingly popular in the biology community. This microscope system makes use of the total internal reflection to

set up a thin sheet of evanescent waves on the bottom of the substrate, as seen in Fig. 2-4. Fluorophores that are far away from the interface (e.g., >100 nm) would not fluoresce due to exceedingly low intensity of excitation light at that depth. However, fluorophores that fall into the proximity region of the interface will be excited by the evanescent wave, and the resulting fluorescence can be detected in far field. This type of imaging mechanism is similar to the condition of the frustration of total internal reflection, under which evanescent wave becomes propagating after being scattered by the micro- or nano-particles.

Both photon-tunneling types of microscope systems have high axial resolution, i.e. within 100 nm. On the other hand, its lateral resolution is still restrained by the diffraction limit. In biomedical research, TIRFM has developed into a power tool to study the surface of the target objects, such as plasma membrane of the mammalian cells.

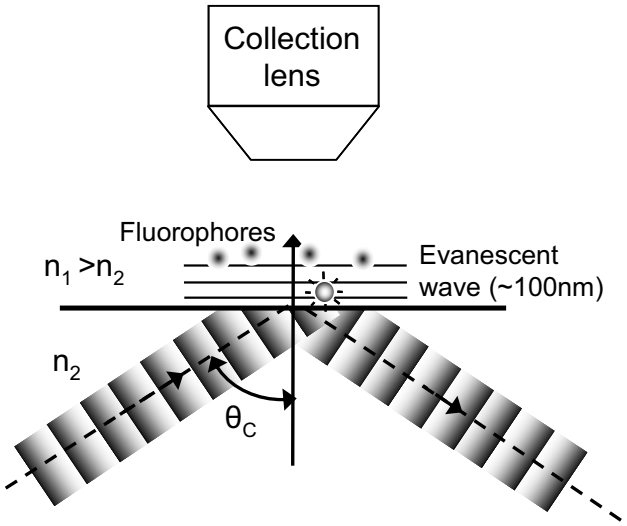

Figure 2-4: Total Internal Reflection Fluorescence Microscope (TIRFM). The TIRF prism sets up a thin sheet of evanescent wave on the substrate surface.

2.2 Operating principles of OFM

Both microfluidics and nanoapertures are readily produced by making use of state-of-the-art planar fabrication technology. In our OFM implementation, we choose to fabricate the nanoaperture array based imager and the microfluidic chip separately. Then these two modules can be bonded together without having to overcome many technological obstacles. One example of a complete OFM is shown in Fig. 2-5 (by courtesy of Xiquan Cui); the total size is even smaller than a US quarter.

Figure 2-5: A compact OFM compared with a US quarter. The OFM consists of a CMOM camera, a thin metallic film with nanoaperture patterns and a microfluidic chip (by courtesy of Xiquan Cui).

We would like to start the discussion of the motivation behind the invention of OFM by examining an example of using a CMOS camera directly for cell imaging purpose (Fig. 2-6 (a)). In this situation, the target cell can be placed directly on or near the surface of the CMOS camera. The shadow image of the cell will then be recorded by the camera. In fact, such a method has been utilized by Lange *et al.* [8] and other groups. Although this simple method enables compact and high-speed imaging, the image quality is by no means desirable. The size of the pixels of a digital camera is finite, typically larger than 5 μm.

Thus, the resolution of the resulting image by using this method cannot be better than the pixel size (L), i.e. 5 μm. (If over-sampling needs to be considered, then the resulting resolution should be 10 μm, i.e. $2L$). Because the size of most of the cells is on the order of 10 μm, cells will show on the screen as featureless and hence tough-to-recognize objects. Therefore, we can conclude that this type of direct imaging, although simple and fast, has limited use in biology research.

However, we do not have to totally abandon this idea of direct projection imaging. One quick solution of its resolution problem is to make smaller camera pixels. For example, a camera with a pixel size of 200 nm will possibly give excellent resolution of a cell. There actually has been steady progress toward this direction, although the pace of the development is quite slow due to tremendous technological difficulties. Therefore, we need to seek new solutions before the pixel size of a CMOS camera can reach such a desired value.

In fact, we may see a slower-than-expected progress in the size reduction of CMOS camera from the semiconductor industry. The trade-off between the dynamic range of the camera pixels and the spatial resolution (i.e. the pixel size) of the camera makes it unfavorable to make the camera pixel too large or too small. Chen, T. and colleagues reported in their conference proceedings that [9], 'for a typical O.35p CMOS technology the optimal pixel size is found to be approximately 6.5 μm at fill factor of 30%. It is shown that the optimal pixel size scales with technology, but at slower rate than the technology itself.'

(1) The first step of building an OFM

Optofluidic Microscope (OFM) successfully introduces the concept of nanoaperture imaging into this type of direct imaging scheme. More specifically, we make use of the OFM method to replace the camera pixels with nanoapertures that are much smaller.

The OFM method can be explained in two separate steps. In the first step (Fig. 2-6 (b)), a thin film of highly conductive metal is coated on the surface of a CMOS camera; after that, submicron through-holes are defined at the center of a row of pixels. The metallic film reflects nearly all the incident light, thus enabling the though holes as the only collectors of

the incoming photons. That is to say, we effectively reduce the size of each camera pixel during this fabrication procedure.

As was introduced in the previous section, the resolution of nanoaperture imaging is, in theory, limited only by the size of the aperture. Therefore, by defining tiny apertures on top of a metal-coated CMOS camera, we can dramatically improve the resolving power of a CMOS camera from the 10μm level to, possibly, the 100nm level.

Nevertheless, using such an imaging device is unlike using a CMOS camera, which can give a full field image within a few milliseconds. In the first-step OFM (Fig. 2-6(b, c)), the tiny apertures are not continually connected, which requires that we should scan the sample or scan the underlying imager, so that each nanoaperture can take a line scan over one stripe of the cell.

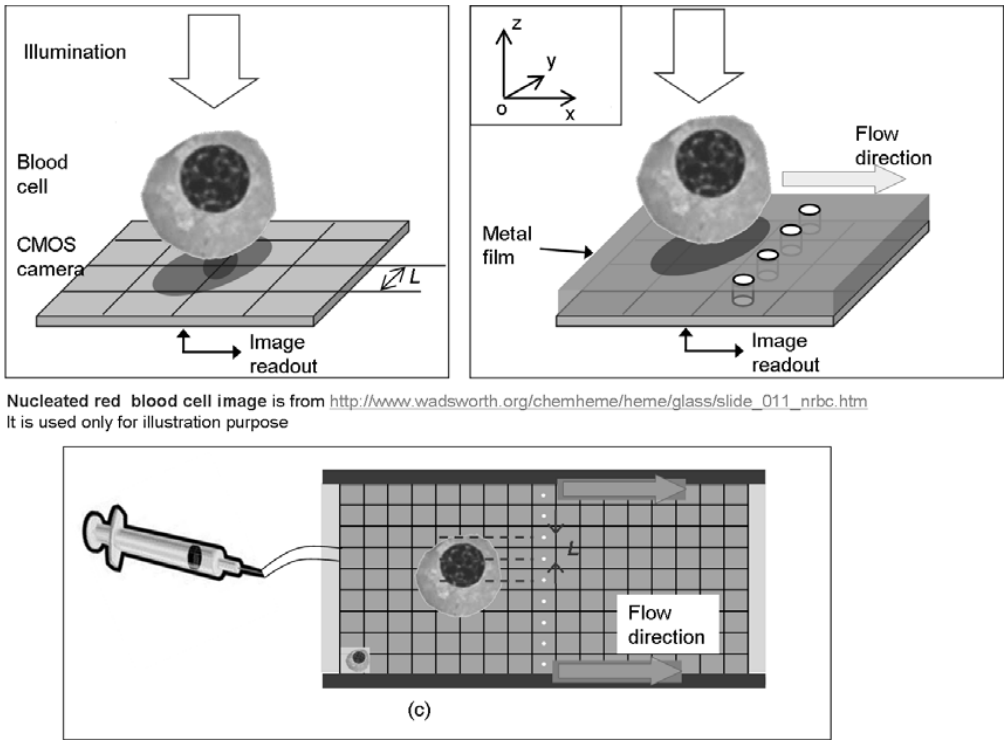

Figure 2-6: (a) A nucleated red blood cell directly on top of a CMOS camera. (b) CMOS camera with a column of nanoapertures. The rest of the camera is protected by a metallic film. The red blood cell flows through the nanoaperture region. (c) A bird's eye view of (b) with a syringe pump.

There are many methods of transporting cell samples, such as microfluidics, optical tweezers or magnetic tweezers. Within microfluidics, numerous actuation mechanisms can be employed, including pressure-difference, electrokinetics, magnetic force, etc. In Fig. 2-6(c), we show the bull's eye view of the device, where a syringe pump is used to deliver the cell sample over the line of nanoapertures.

Nevertheless, we shall notice that there is an under-sampling issue associated with this imaging method. Although the nanoapertures take fine line-scans of the sample in x direction, they are not able to do so in y direction. The reason is that in y direction, these nanoapertures are supposed to separate from each other by at least the length of a camera pixel (~5 μm), such that no two nanoapertures will lie on the same camera pixel. This restriction on aperture spacing determines that the line scans of Fig. 2-6 (c) cannot overlap with each other - a requirement for sufficient sampling.

More specifically, in order to realize the desired optical resolution, it is required that the line scans from adjacent holes should separate from each other by no more than half the diameter of the nanoapertures. Therefore, we have to seek a different scanning scheme is in order to achieve the abovementioned condition of sufficient sampling.

(2) The second step of building an OFM

One proposed OFM design can perfectly overcome such an under-sampling issue. It is illustrated in Fig. 2-7(a) and was first outlined in Ref. [10].

In this specific design, the nanoapertures are brought to the same row in x direction. However, the nanoapertures are punched in such a way that there is a skewing angle (θ) between the nanoaperture array and the flow direction. Equivalently, in the second scheme (Fig. 2-7(b)), the nanoapertures are defined in the center of each pixel, but the microfluidic channel can align with the nanoaperture array with a skewing angle (θ). The advantage of such a layout is that all the nanoapertures have similar responsivity to the light. In fact, such a scheme is exactly what was implemented in the first fully-integrated OFM [11],

although we still use the layout in Fig. 2-7 (a) to explain the key design parameters of OFM.

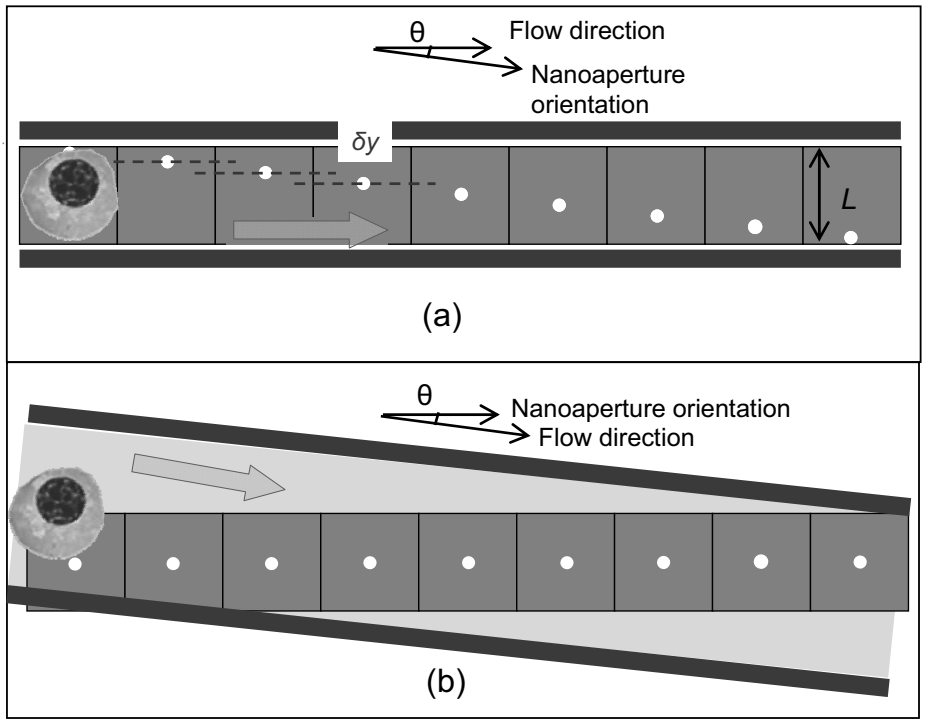

Figure 2-7: Two designs of OFM. (a) The nanoaperture array is punched in a slanted fashion on the CMOS camera; the microfluidic channel is aligned with the camera. (b) The nanoapertures are punched at the center of each camera pixel; the microfluidic channel is aligned in a slanted fashion.

We can easily calculate the pixel size (δx, δy) associated with this skewed scanning method:

$$\delta x = v\delta t$$
$$\delta y = L\sin(\theta) \qquad (2.2)$$

where v is the velocity of the sample motion; δt is the total acquisition time of the recording medium, e.g. a CMOS camera; and L is the size of the camera pixel (Fig. 2-7(a)). Here, the

θ angle is fully controlled by the designer, and it can be adequately small as desired for a small δy. On the other hand, the velocity of the sample motion can be as slow as 100's of microns per second in microfluidics, and it can be even less than 1 μm/s by using other means, like optical tweezers. As such, with a high-speed CMOS camera (normally >5 KHz), δx can also be made sufficiently small in order to satisfy the over-sampling conditions.

Since the nanoapertures are laid out in a slanted fashion, the adjacent nanoapertures, e.g. Hole A and Hole B in Fig. 2-8(a), although scan the neighboring portions of the cell, do not actually 'see' the cell pass by at the same time. Such a result applies to all the other apertures inside the aperture array. As such, the time-of-flight line traces obtained from each aperture will inevitably have a time delay (Δt) with each other, as is illustrated in Fig. 2-8(b). If stacking together all the time traces in y direction, we will end up with a geometrically distorted image of an originally spherical cell (Fig. 2-8(c)).

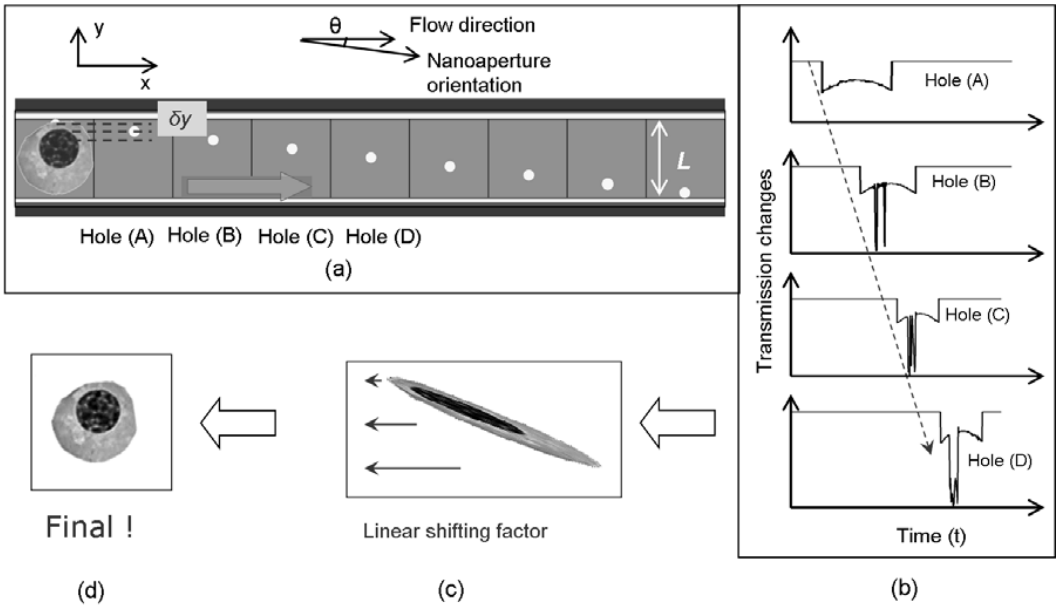

Figure 2-8: Illustration of the image formation process of OFM. (a) A red blood cell is scanned across the nanoaperture region. (b) The transmission signals from 4 apertures. (c) Geometrically distorted image of the RBC. (d) Corrected image of the RBC.

Fortunately, this type of geometric distortion is not random and thus can be removed, assuming that the camera speed and the moving speed of the cell are both constant for the time when the target object passes through the nanoaperture array. By assuming that, we can obtain an expression for the time delay Δt as:

$$\Delta t = \frac{L\cos\theta}{v} \tag{2.3}$$

Note that both L and θ can be determined by fabrication or alignment. The sample speed v is determined by the specific experimental conditions and thus has to be measured in real time.

A simple nanoaperture array is not able to measure the sample speed, as no nanoapertures can scan the identical parts of the object. However, v can be measured by adopting such a method as shown in Fig. 2-9(a). In this innovative design, v is measured through the use of an isolated aperture (α) at one end of the array, such as at the front end (Fig. 2-9(a)).

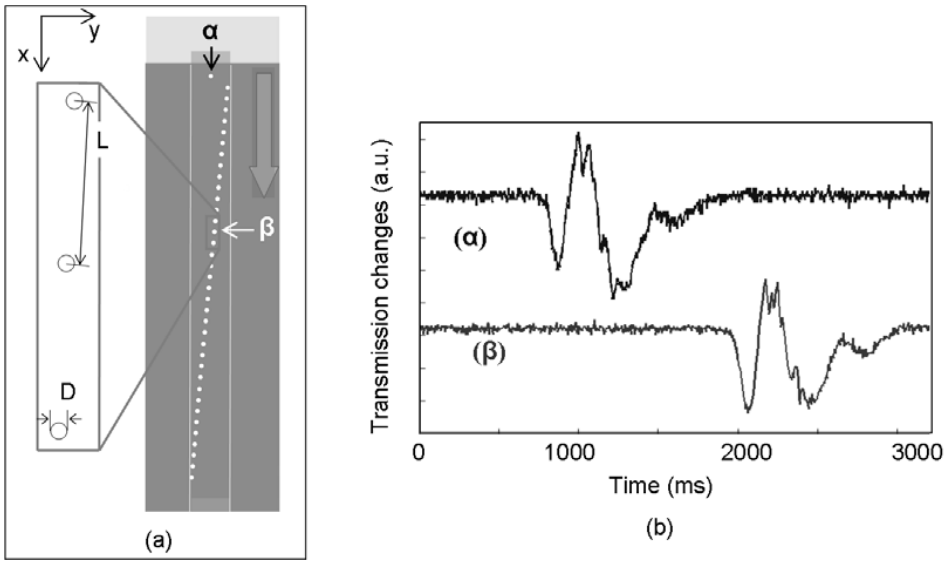

Figure 2-9: (a) Top view of the OFM: introduction of α, an isolated aperture. β: the corresponding aperture within the nanoaperture array, as explained in the text. (b) Example of time-of-flight signals from α and β, which is associated with the translation of an un-rotated *C. elegans* larva.

When we align the nanoaperture array with the fluidic channel in such way that aperture α resides at the center of the channel, then the middle hole of the long nanoaperture array, i.e. aperture β, will have the same y coordinate, as α should scan the same line across the target. As such, v can be calculated as the ratio between the separation of these two apertures ($\overline{\alpha\beta}$) by the time delay between them. After knowing the sample velocity v, then all the parameters in Eq. (2.2) and Eq. (2.3) can be immediately obtained.

In addition, this aperture pair serves an additional function – to monitor the possibility of tumbling/rotation of the pass-by targets. The line scans through different portions of the objects usually look very distinctive, because the target objects, particularly a biological sample, have fine features associated with them. Hence, if the target rotated or tumbled during its passage over the nanoaperture array, the two line scans extracted from aperture α and aperture β would appear dissimilar as the aperture pair scanned different portions of the cell. This unique property of a nanoaperture pair enables us to screen out rotating targets effectively. Figure 2-9(b) shows such a pair of similar line scans acquired through the aperture pair during the passage of an un-rotated *C. elegans*.

This piece of "tumbling screener" should be particularly useful in an automatic imaging scenario, where all the line scans are very rapidly recorded by the underlying camera chip and then read by a computer. The tumbling screener can automatically make a judgment about whether or not the sample was passing the nanoaperture array with a constant speed and static orientation, and then tell the computer program whether to process the data of this sample or dump it immediately. In the other words, this method ingeniously eliminates the human intervention of the entire image acquisition/processing procedure, thus saving a large amount of labor and time.

Besides using an isolated aperture, another way of automatically measuring the sample speed is to use multiple nanoaperture arrays to acquire an image [11]. As long as the nanoaperture pairs like α and β can be spotted in such a multiple-line array, a similar method can be used to calculate the flow speed and/or screen out rotating samples.

Up to this stage, I have briefly explained the most fundamental design rules of an Optofluidic Microscope. In the next section, I will sketch out a few different OFM designs,

which should have general interest. In the next chapter, I will discuss the implementation of the first OFM prototype and its application in biology.

2.3 Other OFM configurations

OFM method was outlined in full length in the previous section. In short, OFM method nicely overcomes two major problems: 1) the resolution and 2) the sampling issue. Besides the original OFM architecture, there are also many other ways of constructing an Optofluidic Microscope device that is worth of future investigation. Therefore, I would like to devote a section to the discussion of a few imaging functionalities that should be realizable with OFM in near future.

Illumination type of OFM

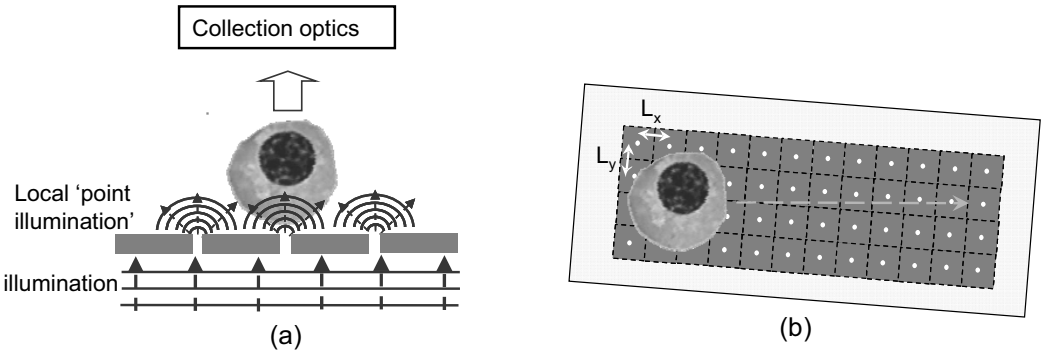

Figure 2-10: (a) Illumination type of OFM. It can be fabricated on a LED or laser diode. (b) Nanoaperture grid replaces the former nanoaperture 1D array.

The first thing we should notice is that the OFM design discussed so far (Fig. 2-7 – Fig. 2-9) is essentially a collection type of imaging device. By contrast, an illumination-mode OFM can also be constructed. In this case, the nanoapertures can be defined directly on a

metal-coated LED head or laser diode (Fig. 2-10 (a)). As such, the entire illumination unit can be made both compact and cheap. Conventional sample delivery schemes such as microfluidics are still compatible with this system. In Chapter 7, more details will be disclosed about the illumination mode OFM, where it is coupled with optical tweezers.

However, more micromachining effort needs to be undertaken in order to reduce the size of the optical collection portion of the device (Fig. 2-10 (a)), provided that compactness is a critical "selling point" of the device. Fortunately, there have been ways of fabricating compact collection optics possibly for this usage, such as tunable fluidic lenses [12] or a GRIN lens, to name a few.

Grid based OFM

Another important innovation beyond the original 1D nanoaperture array is to add another dimension to this device, i.e. utilizing a 2D nanoaperture array. In Chapter 7, when we discuss this type of OFM design in more detail, we term it a grid-based OFM. One such grid is shown in Fig. 2-10 (b).

The most important feature of a grid-based OFM is that the total length of the nanoaperture array can be vastly reduced by folding a lengthy 1D array into a compact 2D array. In this case, a number of nanoapertures can scan different parts of the sample at the same time, thus reducing the total acquisition time. More importantly, the entire image acquisition will be much less vulnerable to the possible rotation of the samples during their passage over the nanoapertures. However, this design has already assumed that the sample size is larger than the pixel size of the underlying camera; otherwise, the advantages of using a 2D aperture grid will not exist.

SPP assisted OFM

Surface plasmon polaritons (SPP) have been a hot topic in the field of nanoapertures. More specifically, it has been shown that through the use of corrugated metallic surface, SPP was able to beam optical waves through nanometric aperture [13], thus possibly enhancing the

transmission of the tiny holes, as well as increasing the depth of focus associated with the holes. One such device is illustrated in Fig. 2-11. Here, the surface corrugation serves as a coupler for the momentum of the incident beam ($K_{//}$) to match with that of the SPP (K_{SPP}). Mathematically, it has been given in Chapter 1,

$$K_{SPP} = K_{//} \pm G \tag{2.4}$$

where G represents a series of the reciprocal wave-vectors provided by the periodic surface corrugation or the nanoaperture array lattice. Note that in Fig. 2-11(a), the surface corrugation does not have to be on the top surface of the metal film. It could be on the bottom side or on both sides depending on the application. Usually the surface corrugation on the top surface is to beam the light through the nanoaperture, whilst that on the bottom side can be used to reshape the diffraction pattern.

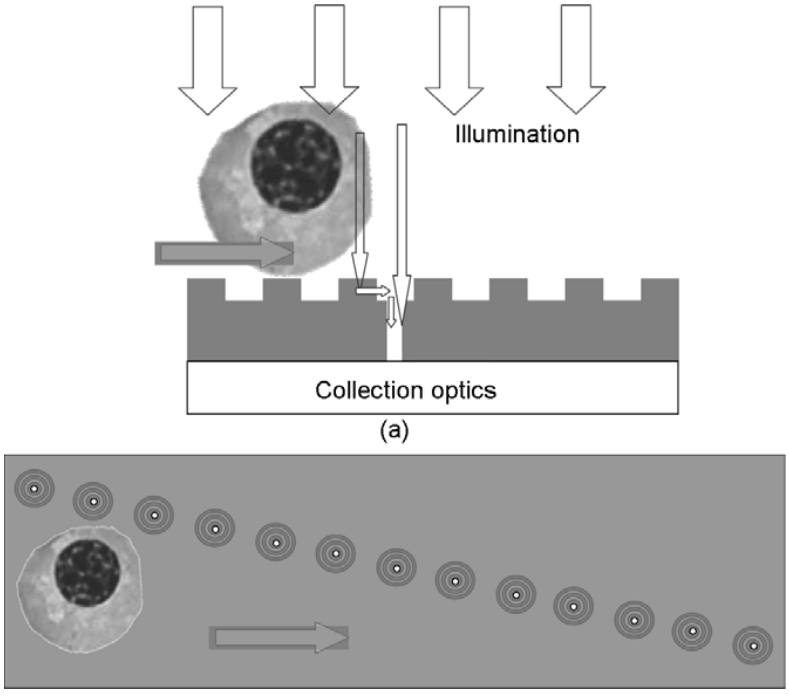

Figure 2-11: Illustration of SPP assisted OFM. (a) Side view of such a device. Surface corrugation is formed around the through-hole. (b) Top view of an SPP assisted OFM device with arrays of concentric rings.

OFM with a fiber bundle

The next scheme of OFM implementation stems from recent work on fabricating ordered nanoaperture arrays directly out of a fiber bundle [14]. Fig. 2-12 (a) shows a side view of such a bundle. These ordered nanoapertures can be considered as an array of NSOM tips, which enable high-speed, high-resolution imaging. A key advantage of this nanoaperture bundle is that the collection optics can be vastly simplified, as the other end of the fiber bundle can easily align with a recording medium. However, more research needs to be conducted in order to improve the yield of the fabrication technique; as in this paper, only ~60% of all the nanoapertures were found functional (Fig. 2-12(b)).

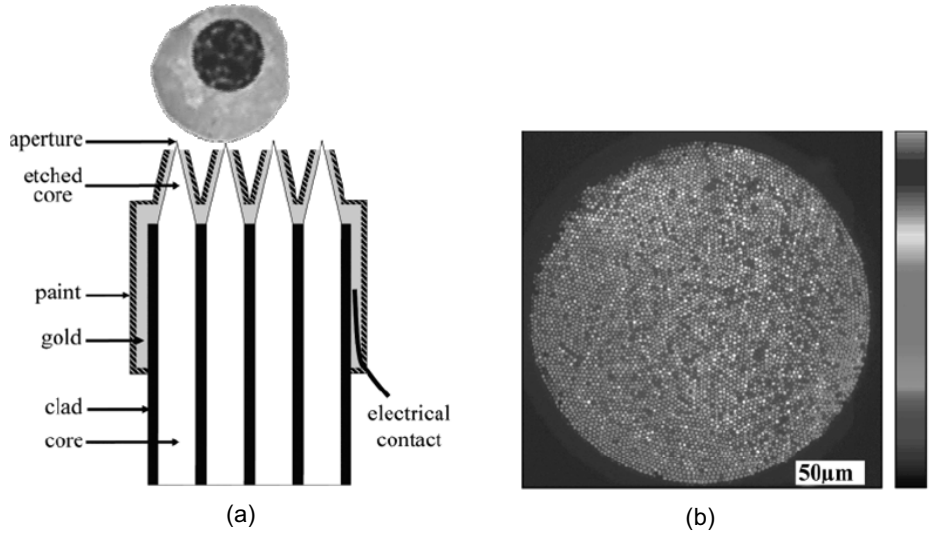

Figure 2-12: (a) Schematic of the nanoaperture "bundle". (b) Epi-fluorescence image collected through the array. Reprint permission from Ref. [14].

Fluorescence OFM

Fluorescence is arguably the most important functionality of a microscope, especially for the biologists and chemists. For example, molecules in a cell nucleus can be tagged with fluorophores by a simple chemical reaction, and the fluorescence of the tag enables sensitive and quantitative detection of the molecules in the nucleus. Thanks to the rapid

development of thin film filters directly on a microchip, implementation of fluorescence OFM is very promising. One such OFM device (collection-mode) is shown in Fig. 2-13, where a linear-variable bandpass filter is pre-deposited on a CMOS camera. Multiple nanoaperture arrays can be fabricated on a single chip to enable multi-spectral imaging. On the other hand, if a single fluorescence line is sufficient, then a uniform dielectric filter can be coated on the CMOS sensor and a relatively simple light source can be utilized. There is an excellent review on integrated fluorescence filters on Lab On a Chip [15].

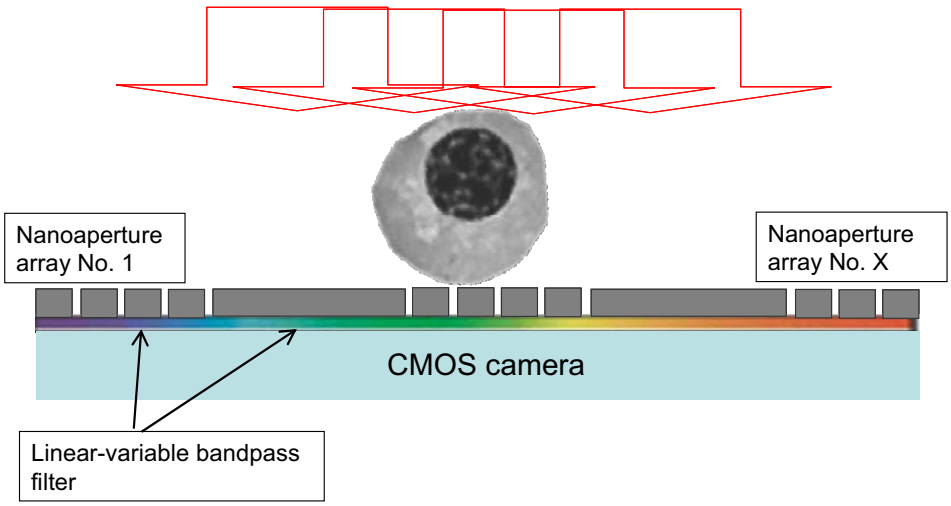

Figure 2-13: Fluorescence OFM. A multicolor filter is directly deposited on the camera surface.

Concluding remarks of this chapter

In this chapter, we first introduced the operation motif of both conventional microscopy based on lens magnification and near field microscopy based on nanometric tips. Later on, we discussed the operating principles of Optofluidic Microscopy and a few modified versions of the device. From the imager implementation point of view, the imaging portion of OFM, i.e. CMOS sensor + metallic film + nanoaperture array, can be considered as a resizing process for the pixels on the CMOS camera. From the microscopy theory point of

view, OFM, similar to near field microscopy, is based on nanoaperture imaging and is independent of a lens magnification unit. Therefore, OFM is, in essence, a lensless imaging technique. By directly fabricating the nanoapertures close to a CMOS surface, the entire device can be made compactly and cheaply. We can easily integrate microfluidic platforms into OFM because their fabrication procedures are compatible. By making use of the advantages of microfluidic technologies, an OFM device is capable of high-throughput, multi-functional imaging without a lot of labor-intensive effort.

Reference

1.J. W. Goodman, *Introduction to Fourier optics* (New York : McGraw-Hill, 2004)).
2.S. Inoue, and K. R. Spring, *Video microscopy: the fundamentals* (New York : Plenum Press, 1997)).
3.M. Bates, B. Huang, G. T. Dempsey, and X. W. Zhuang, "Multicolor super-resolution imaging with photo-switchable fluorescent probes," Science **317**, 1749-1753 (2007).
4.E. Betzig, G. H. Patterson, R. Sougrat, O. W. Lindwasser, S. Olenych, J. S. Bonifacino, M. W. Davidson, J. Lippincott-Schwartz, and H. F. Hess, "Imaging intracellular fluorescent proteins at nanometer resolution," Science **313**, 1642-1645 (2006).
5.L. Novotny, D. W. Pohl, and P. Regli, "Light propagation through nanometer-sized structures: the two-dimensional-aperture scanning near-field optical microscope," Journal of the Optical Society of America a-Optics Image Science and Vision **11**, 1768-1779 (1994).
6.J. M. Gerton, L. A. Wade, G. A. Lessard, Z. Ma, and S. R. Quake, "Tip-enhanced fluorescence microscopy at 10 nanometer resolution," Physical review letters **93** (2004).
7.http://www.olympusmicro.com/primer/techniques/nearfield/nearfieldintro.html.
8.D. Lange, C. W. Storment, C. A. Conley, and G. T. A. Kovacs, "A microfluidic shadow imaging system for the study of the nematode Caenorhabditis elegans in space," Sensors and Actuators B-Chemical **107**, 904-914 (2005).
9.T. Chen, P. Catrysse, A. El Gamal, and B. Wandell, "How Small Should Pixel Size Be?," in *Sensors and Camera Systems for Scientific, Industrial, and Digital Photography Applications, Proceedings of SPIE*, M. M. Blouke, N. Sampat, G. M. J. Williams, and T. Yeh, eds. (2000), pp. 451-.
10.X. Heng, D. Erickson, L. R. Baugh, Z. Yaqoob, P. W. Sternberg, D. Psaltis, and C. Yang, "Optofluidic microscopy- a method for implementing a high resolution optical microscope on a chip," Lab on a Chip **6**, 1274 - 1276 (2006).
11.X. Q. Cui, X. Heng, W. W. Zhong, P. W. Sternberg, D. Psaltis, and C. H. Yang, "Imaging microorganisms with a high-resolution on-chip optofluidic microscope," *submitted* (2007).
12.S. Kuiper, and B. H. W. Hendriks, "Variable-focus liquid lens for miniature cameras," Applied Physics Letters **85**, 1128-1130 (2004).
13.H. J. Lezec, A. Degiron, E. Devaux, R. A. Linke, L. Martin-Moreno, F. J. Garcia-Vidal, and T. W. Ebbesen, "Beaming light from a subwavelength aperture," Science **297**, 820-822 (2002).

14.A. Chovin, P. Garrigue, I. Manek-Honninger, and N. Sojic, "Fabrication, characterization, and far-field optical properties of an ordered array of nanoapertures," Nano Letters **4**, 1965-1968 (2004).
15.M. Dandin, P. Abshire, and E. Smela, "Optical filtering technologies for integrated fluorescence sensors," Lab on a Chip **7**, 955-977 (2007).

Chapter 3

CONSTRUCTION OF THE FIRST OFM PROTOTYPE

In this chapter, I will discuss in detail the fabrication procedure of the individual modules of the first OFM prototype, such as the nanoaperture array and the microfluidic channel. The employed fabrication techniques include thin film deposition, electron beam lithography, reactive ion etching, photolithography, soft lithography, etc. Toward the end of the chapter, I will explain how to assemble all the modules together.

3.1 Fabrication of the nanoaperture array

The first OFM prototype was not directly made on a CMOS sensor. Instead, in order to facilitate the justification of the OFM principle, the nanoaperture array was actually fabricated on a glass substrate. The images of the nanoapertures were projected onto a CCD camera using a regular microscope setup. In this way, we were able to verify the working principle of OFM in a much simpler manner. More details on the experimental procedure will be sketched out in Chapter 4. Here, I will only discuss about the fabrication process.

The fabrication of the nanoaperture array generally takes five steps (Fig. 1). First, the glass slide (fused silica or Pyrex) is cleaned with hot piranha, and then a thin layer of metal is evaporated on the top surface of the slide. Highly conductive metal has a shallow skin depth and thus is preferred as an opaque mask. For example, at λ_o= 632.8 nm, the skin depth (based on intensity attenuation) of aluminum, gold, and silver is 6.6 nm, 17 nm, and 12.6 nm, respectively. In the first OFM prototype, we chose aluminum as the mask material, as its skin depth is short and it adheres to glass very well. 90nm thick aluminum was evaporated on top of the glass slide by using an electron beam evaporator.

Next, a thin layer of Poly(methyl methacrylate) (PMMA) was spin-coated on top of the metallic surface. PMMA is a type of positive electron-beam lithography resist. Actually, it is by far the most popular resist, offering extremely high resolution, ease of handling, and

excellent film characteristics. Electron beam exposure causes scission of the polymer chains. Then the exposed (lighter molecular weight) resist is developed in a solvent developer.

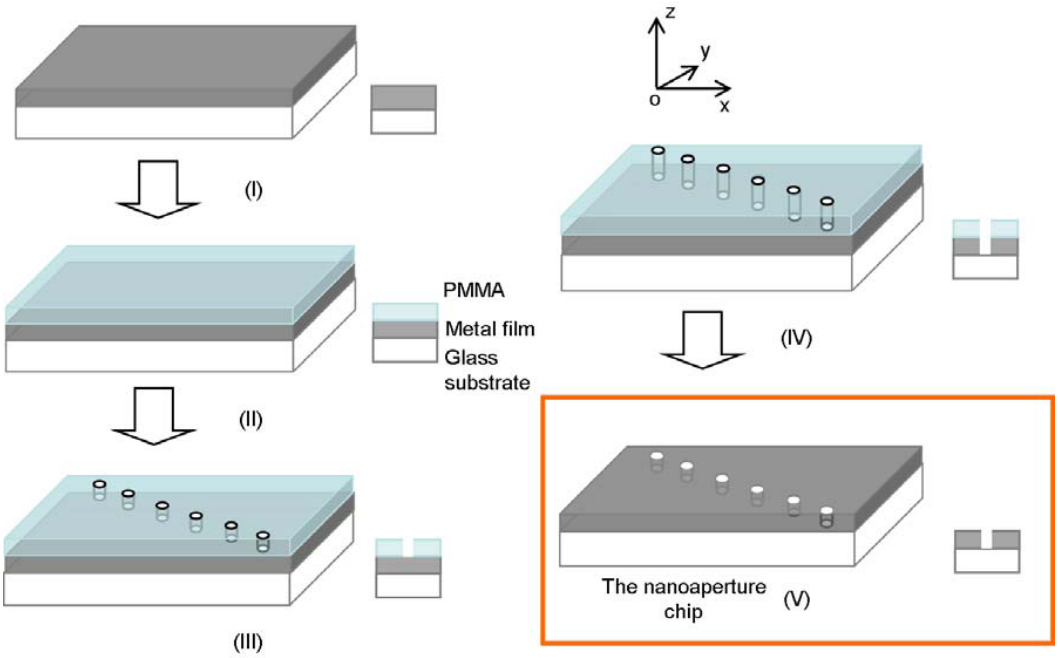

Figure 3-1: Fabrication procedure of the nanoaperture array. Step (I): metal evaporation. (II) Spin coat PMMA on metal surface. (III) E beam lithography and solvent development. (IV) Reactive ion etching to transfer the nanoaperture pattern into the metallic film. (V) Strip off the PMMA residue.

When fabricating nanometric through-holes on metallic surface, it is suggested that the thickness of the PMMA film should be at least twice that of the metal film, because PMMA will later be used as an etching mask. Hence, we selected PMMA 950 c4, which is about 250 nm thick when being spun at 4500 RPM ("rounds-per-minute"). After spin coating, we baked the PMMA resist on the 180^{o}C hotplate for 10 to 15 minutes.

In the third step (Fig. 3-1), we define the nanoaperture array on PMMA by using an e beam writer, such as JEOL 9300 FS. Subsequently, the sensitized pattern is dissolved in PMMA developer (Microchem Corp.).

The specific parameters of the nanoaperture array, such as the aperture size, the aperture spacing, and the number of apertures, were defined in CAD software beforehand. The size of the nanoapertures for OFM can range from 50 nm to 1 μm. The spacing between nanoapertures is 5 μm or 10 μm, which are both popular pitch spacing for a CMOS camera. Note that although e beam lithography is excellent in accurately defining nanostructured patterns, the process consumes a long time and has a low efficiency. However, most of the nanoaperture sizes can be fabricated with the use of state-of-the-art photolithography technologies, which are thus a perfect choice for mass-producing OFM cheaply.

In the fourth step (Fig. 3-1), the nanoaperture array defined on PMMA is transferred into the metal. Both dry and wet etching techniques are normally used for this purpose. However, wet etching is usually isotropic and has poor directionality. As such, the walls of nanoapertures can be severely undercut. Feature sizes less than 1μm usually cannot be resolved after the wet etching process.

In comparison, dry etching is much better suited for transferring optical microstructures because of its high directionality. Thus is the choice for us. Among all the usual metal candidates for OFM, i.e. Al, Ag, Au, and Cu, Al is the simplest one that can be dry etched by chlorine based etching gas. The etch rate of aluminium varies between different recipes and different machines. For example, by using the Unaxis SLR770 ICP in UCLA's Nanolab, I can etch Al at 2-3 nm/sec. Hence, it usually takes less than one minute to finish etching through the aluminum material.

Finally, the PMMA residue needs to be removed. The utilizable "strippers" include acetone, NMP, methylene chloride, oxygen plasma, Nanostrip, etc. In my fabricate process, I found that methylene chloride can usually strip off residue PMMA within half a minute, and this solvent is compatible with aluminium. (Note that Al is much more chemically active than noble metals such as Au or Ag. Thus, more attention should be paid to undertaking aluminum based fabrication procedure).

An example of one final nanoaperture array is shown in Fig. 3-1 (V). An SEM image of a pair of holes from a nanoaperture array is shown in Fig. 3-2. For this particular example, the size of the apertures is 600 nm, and their spacing is 10 μm.

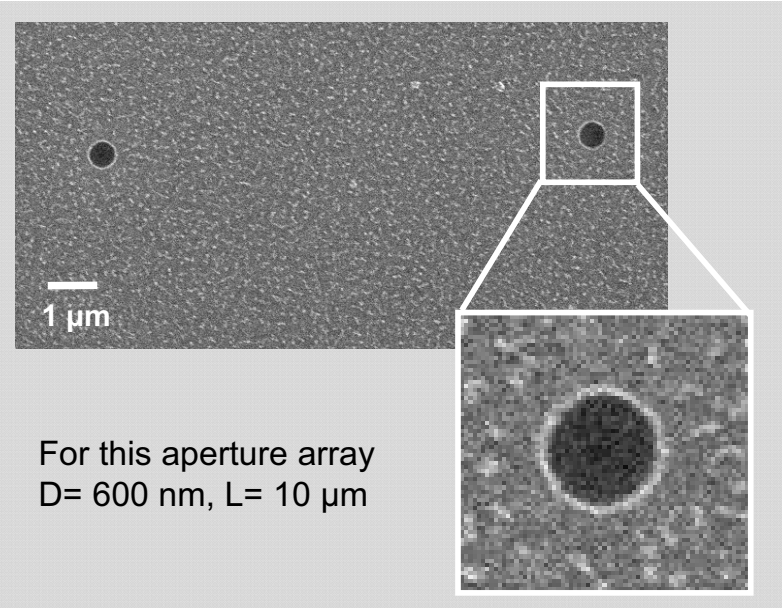

Figure 3-2: SEM images of nanoapertures fabricated by an e beam lithography process.

3.2 Fabrication of microfluidic chips

The introduction of soft elastomeric material into microfluidic technology has a short history. In the 1990's, Whitesides group in Harvard was one of the first to start using Poly(dimethylsiloxane), i.e. PDMS, to make microfluidic chips out of an already-completed rigid mold. This type of fabrication is termed replica molding, or more generally, soft lithography.

Replica molding usually takes the general procedure as follows

1. Patterns of the microfluidic device are still created by using standard lithography procedures such as photolithography or electron beam lithography. Popular substrates include silicon and silicon dioxide.

2. The stamp is produced by pouring degassed PDMS resin over the top of the patterned substrate. For example, RTV A and B (RTV 615, General Electric Silicone, Wilton, CT) can be mixed with a ratio of 10:1 to create relatively soft PDMS. They can also be mixed with a 5:1 ratio to produce more rigid PDMS.
3. Then the PDMS resin is baked at 80^{o}C for an hour or two to solidify the resin.
4. The solid PDMS chip is then peeled off from the substrate; the microfluidic pattern, by this time, has been stamped into the PDMS material.
5. The microfluidic mold can then be saved for later use.

The advantages of utilizing soft lithography techniques in creating microfluidic chips are abundant. First, the molding process is simple and rapid. It allows for fast prototyping at the developmental age and rapid mass-production at the manufacturing stage. The density of the functional units on a microfluidic chip can be very high, because the fabrication of the mold is compatible with the VLSI fabrication technology.

Second, PDMS is cheap and disposable. Microfluidic channels or interconnects, during their lifespan of usage, normally encounter clogging or contamination problems. In glass-based or silicon-based microfluidics, the microchip itself after being clogged would have to be disposed if the cleansing process fails. As a consequence, new chips need to be made for new experiments, and the fabrication procedure would inevitably introduce additional cost. However, we do not have to do the same thing when using PDMS chips. After throwing away the old PDMS chips, a fresh elastomeric chip with exactly the same geometry can be replicated out of the same mold that was used to make the earlier chips.

In addition, the replica molding process does not have to be carried out in a clean room environment, thus making the microfluidic technology more accessible to biology and chemistry community.

Figure 3-3 summarizes the fabrication process of the microfluidic channel we have been using in OFM. The creation of a rigid mold is completed by the use of standard photolithography. First, the microfluidic channel structures or valve structures, such as the electrokinetic focusing channel structure (Fig. 3-3(a)), need to be designed in CAD software. Then the patterns in a CAD file can be printed on a plastic transparency mask or

made on a chromium mask. Next, the pattern of the microfluidic device on the mask can be transferred onto a silicon wafer by the use of photolithography.

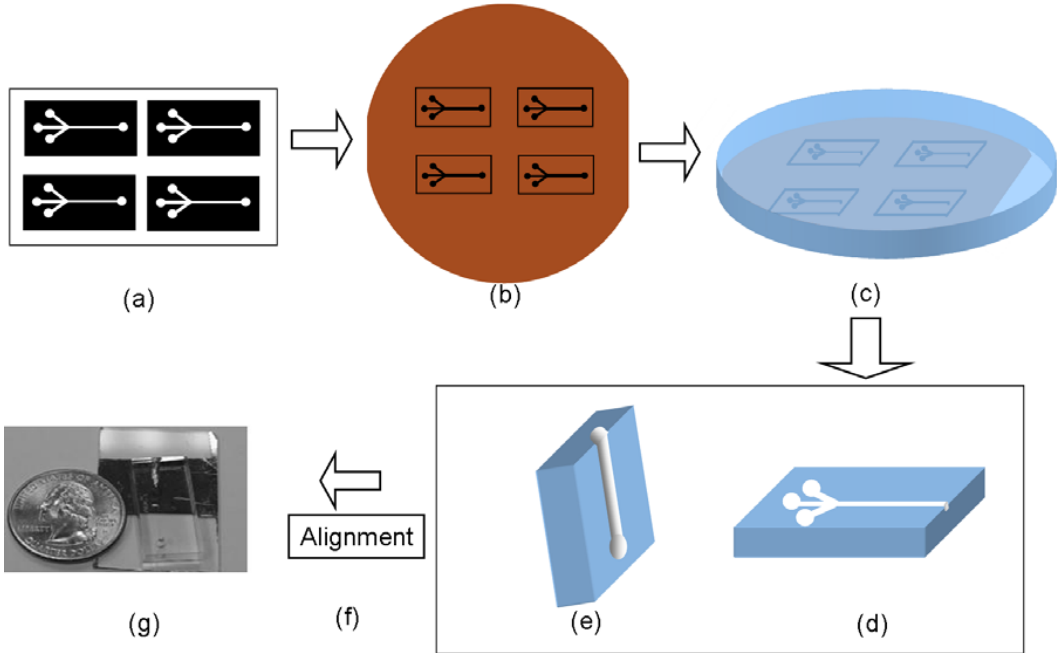

Figure 3-3: Microfabrication of the fluidic chip. (a) Patterns of the fluidic channel are drawn in CAD software. (b) A rigid mold of the microfluidic pattern made by photolithography. (c) PDMS is poured onto the mold. (d, e) The PDMS chip is peeled off the mold. (g) Example of such an OFM prototype compared with a US quarter.

The photoresist we chose is SU8-2025 (Microchem Corp.), which is capable of creating microstructures with a height of 10 μm to 30 μm. We use a Suss mask aligner (Karl Suss MA6) to "imprint" the pattern of the microfluidic device onto the SU8. Note that, after post-exposure bake and development, we bake the final chip at 180^{o}C for 10 minutes to round up the channel a little bit as well as make the material more rigid and sustainable.

The channel structures in Fig. 3-3 (c) can be transferred onto PDMS elastomer by using the soft lithography process as explained earlier. Inlets and outlets of the micro channels are then punched. The orientation of the inlets of the micro channel is shown in Fig. 3-3

(d). In such a way, we can make use of the gravity-driven fluidic flow, whose implementation will be explained in more detail in Chapter 4.

3.3 Assembly of the nanoaperture chip with the microfluidic chip

In this section, I will explain how we align the nanoaperture array with the microfluidic channel such that the nanoaperture can nicely span the whole width of the channel.

The geometry of the nanoaperture array and that of the microfluidic channel is relatively easy, not containing complex or highly curved patterns. As such, aligning them together is not too difficult. We make use of a microscope or a mask aligner to line up these two modules properly (such as Fig. 2-7 of chapter 2). After the alignment, the PDMS chip can bond onto the surface of the metallic chip (i.e. nanoaperture array) by using a small mechanical force, such as that from forceps.

The bonding between PDMS and aluminum is excellent, and thus fluid leakage has not normally been detected throughout my experiment. There has been consensus about the fact that the hydrophobility of the PDMS surface makes it notoriously difficult to pump fluid into the micro channels. However, in my experiment, I used relatively large micro channels, e.g. 15μm high x 30μm tall [1], and thus no surface treatment such as Oxygen plasma was used to "oxidize" the surface of PDMS before the elastomeric chip was hermetically sealed onto the metallic chip.

Figure 3-4(a) shows a "pseudo" example of the final alignment result. In the microscope image, the aperture size is 600 nm, and the spacing is 10 μm. The isolated aperture, which is required to measure the speed of the flowing sample, is ~40 μm above the nanoaperture array and 10μm to the left of it. An 80μm-wide microfluidic channel lined up with the nanoaperture in a slanted fashion. The total number of apertures in the nanoaperture array is 121, which gives a pixel size $\delta y = {80\mu\text{m}}/{121} = 0.66\mu\text{m}$. The isolated aperture is aligned with the central hole of the nanoaperture array. When the nanoapertures are made almost uniform in size, the transmission through the individual apertures can be shown nicely on a camera screen (Fig. 3-4 (b)).

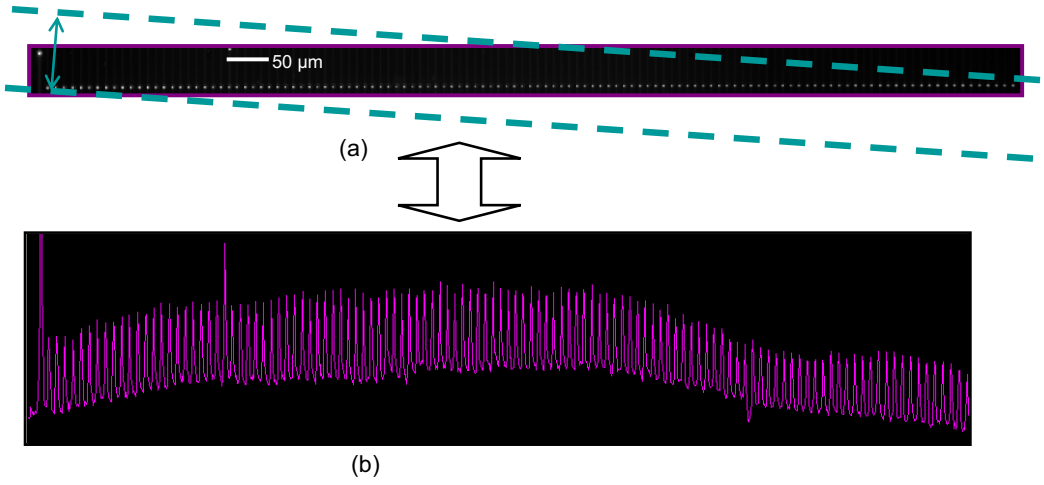

Figure 3-4: (a) Image of a nanoaperture array with an isolated hole; the dashed lines represent the microfluidic channel. (b) The transmission signals through individual apertures. The isolated aperture is slightly wider, thus having larger signal strength.

Although making the complete device is not the motif of my thesis, I would still like to make some simple but maybe naïve comments on the device integration aspect of the OFM. In general, there are two strategies of building a device, whether or not compact. One is the integration scheme and the other is the module-based scheme in general.

In order to make the OFM device easy to use and cheap to dispose, the module-based scheme seems to be better suited. That is to say, the microfluidic chip and the nanoaperture imager should be made separately and the replacement of one of the functional unit will not affect the working conditions of the other. However, it needs to be born in mind that the module-based approach usually makes the system bulky and often causes various problems when wanting to make two separate units cooperate. Therefore, it may be more beneficial to separately integrate all the optical units and integrate all the microfluidic units, as illustrated in Fig. 3-5 – a hybrid approach. For example, when we plan to insert a

fluorescence filter into the system, it might be better to deposit them directly on the camera, rather than making the filter as an independent unit.

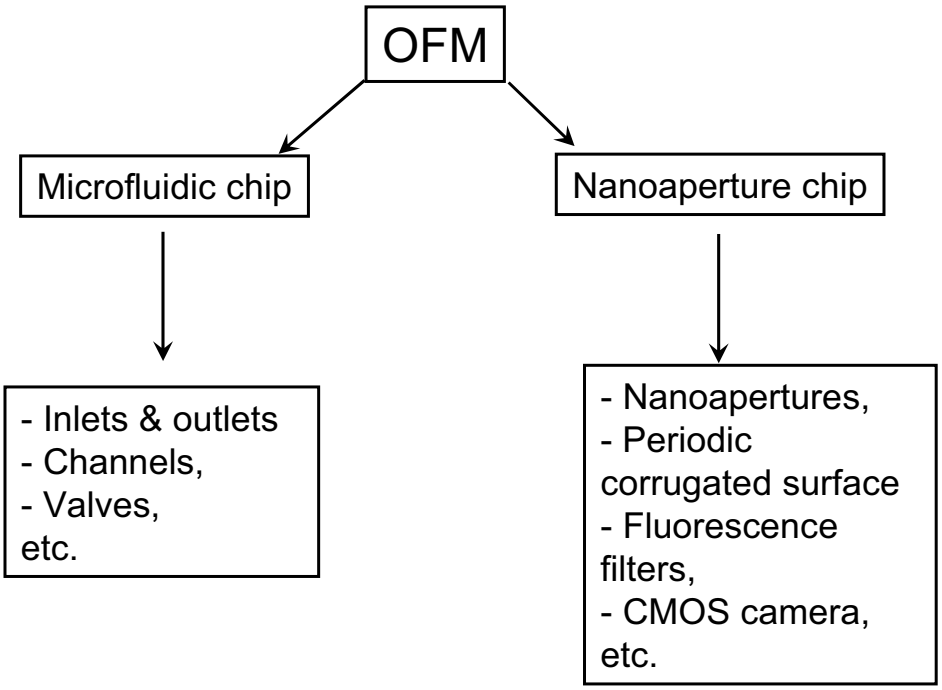

Figure 3-5: Infrastructure of an OFM device: the hybrid approach.

Concluding remarks of this chapter

The fabrication of OFM takes advantage of the state-of-the-art lithography technologies and the assembly of all the functional modules is quite straightforward, making it easy for mass reproduction. The separation of different functional modules is ideal when the replacement of one module but not all the modules is necessary.

Reference

1.X. Heng, D. Erickson, L. R. Baugh, Z. Yaqoob, P. W. Sternberg, D. Psaltis, and C. Yang, "Optofluidic microscopy- a method for implementing a high resolution optical microscope on a chip," Lab on a Chip **6**, 1274 - 1276 (2006).

Chapter 4

APPLICATIONS IN NEMATODE IMAGING AND PHENOTYPE CHARACTERIZATION

In this chapter, I will explain the initial imaging experiment we have performed with the first OFM prototype. I will reveal the detailed design parameters such as specifications of the nanoaperture array and the setup of the imaging system. Our first biological example was larvae of nematode, *C. elegans*. Images acquired from different *C. elegans* genotypes were utilized for the purpose of phenotyping. In addition, I will discuss the imaging performance of the OFM device, e.g. the resolution that should be feasible for the device.

It is worth noting that in the initial setup I did not built up the Optofluidic Microscope as a complete on-chip device: we only integrated together the nanoaperture array chip and the microfluidic chip (Fig. 4-1(a)). Instead, an inverted microscope was utilized to project the nanoaperture array onto a CCD camera. However, based on the principles of nanoaperture imaging, the optical microscope played no role in limiting the resolving power of the nanoaperture array; instead, it merely functioned as optical beam relay.

4.1 Imaging of *C. elegans* larvae

The full name of *C. elegans* is *Caenorhabditis elegans*. It is a kind of free-living nematode that can be found in temperate soil environments. *C. elegans* is the choice of model micro-organisms for the studies of genetics, development and behavior, as well as the nervous system. From the research perspective, *C. elegans* has the advantages of being a multi-cellular microorganism with a complete description of cell lineage. It has developed quite a few mature physiological infrastructures such as nervous systems but is still simple and cheap enough in terms of culturing, gene analysis, and cell development studies. That is to

say, *C. elegans* is a transparent roundworm that is complex enough to provide biological interest but is still simple enough for observation and quantitative analysis.

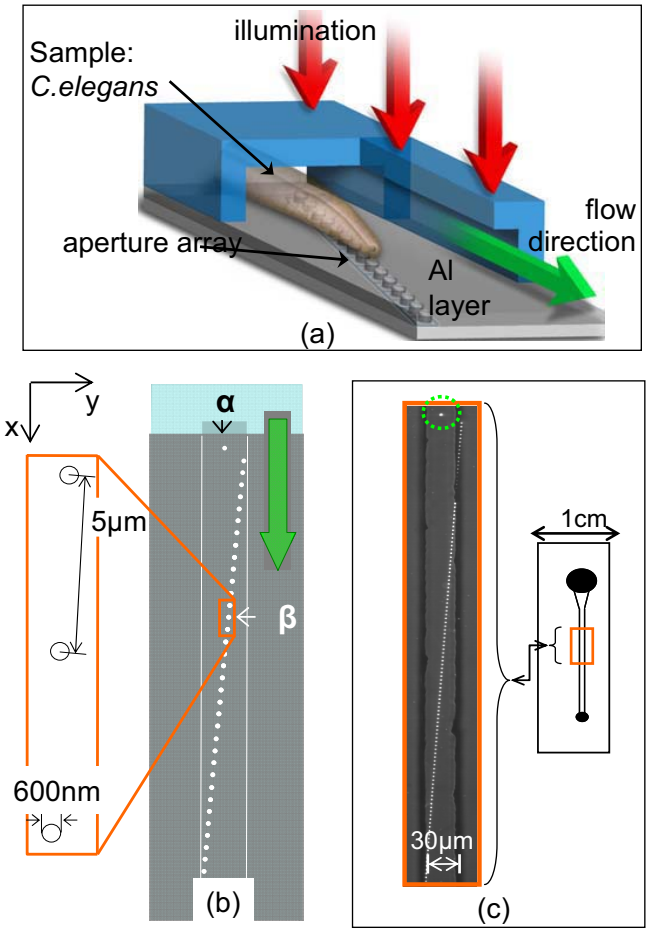

Figure 4-1: (a) Schematic of the OFM prototype. Nanoaperture array is defined on thin Al film. (b) Illustration of the nanoaperture pattern with an isolated hole. (c) Image of such a nanoaperture array.

Molecular genetics has advanced to the point that genome-wide screens using libraries of RNAi have become standard, but the determination of phenotypes is now one of the limiting steps in genetic analyses. At present, *C. elegans* are routinely used for drug

screening [1], and the phenotype determination problem has yet to be addressed satisfactorily. In many cases, body size and body shape are the major phenotypes. For example, abnormal TGF-beta signaling pathway affects body size [2]. However, in current *C. elegans* research, the parameters are only described qualitatively by adjectives such as "dumpy", "small", etc. This can be attributed to the fact that the difference between phenotypes often remains undistinguishable to human observers. For these reasons, an automated, accurate and high-throughput phenotyping system will be very useful.

The experimental setup is illustrated in Fig. 4-2 and Fig. 4-3 (a). The OFM prototype consists of an opaque Al film (90 nm) with an etched array of submicron apertures (L= 5.0 μm, D= 600 nm, number of apertures: 100, see Fig. 4-1(b, c)) and a PDMS microfluidic chip (width= 30 μm, depth= 15 μm, length ~2 cm). The nanoaperture array is oriented at a small angle (θ= 0.06 rad.) relative to the micro-channel (Fig. 4-1). A uniform light source (Lamina BL3000, white LED) at normal incidence to the device provides the illumination (~0.1 W/cm^2).

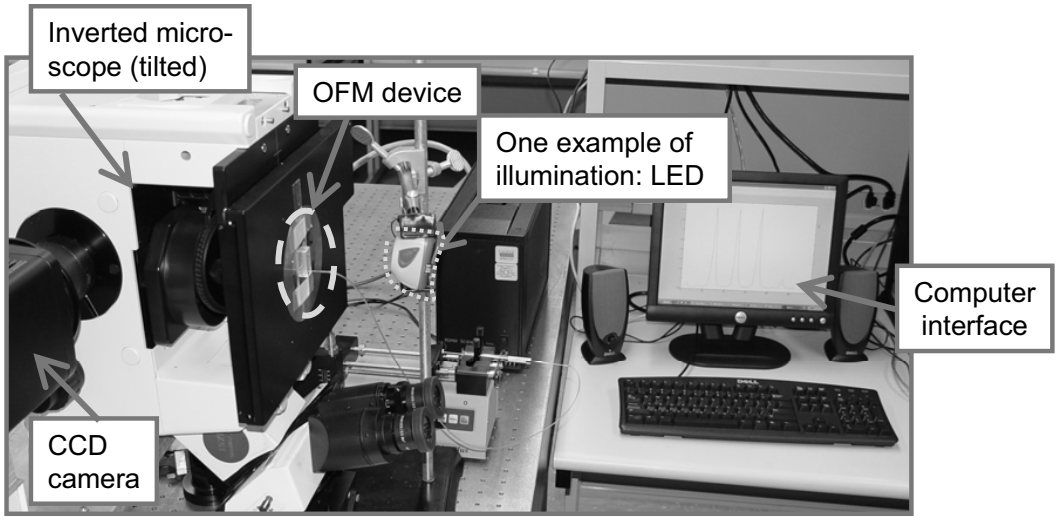

Figure 4-2: Photograph of the experimental setup.

The placement of the OFM device on the sensor array should be such that the transmission through each aperture maps uniquely onto a single pixel of the sensor array. The fabrication of the prototype directly onto a sensor array is straightforward [3, 4] and can be efficiently executed in commercial settings.

In our present setup, the transmissions were relayed through the use of an inverted microscope (Olympus IX-51) onto a CCD camera (Princeton Instruments, Spec10-100), as is shown in Fig. 4-2 and Fig. 4-3(a). The conventional optical microscope served as a relay optical system and played no direct role in limiting the resolving power of OFM. However, this arrangement facilitates the evaluation of the imaging performance of the OFM prototype more easily.

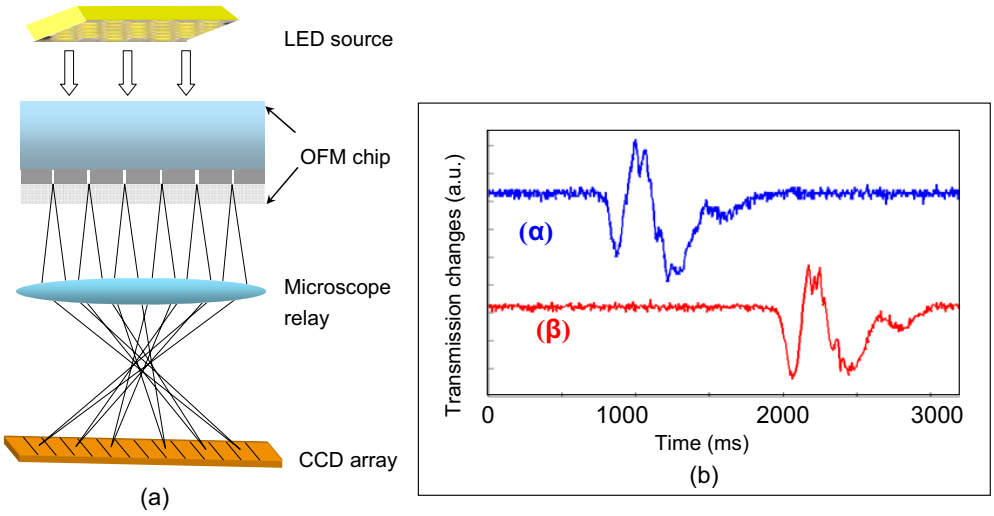

Figure 4-3: (a) Illustration of the experimental setup. (b) Example of time-of-flight signals from α (blue) and β (red), which are associated with the translation of a *C. elegans* larva.

Imaging a target with an OFM device is accomplished by flowing the target across the nanoaperture array. As it passes over the nanoaperture array, each individual aperture will take a line scan of the target. The principles of image formation have been discussed in Chapter 2: in short, by compiling all the time-of-flight line scans and considering the time

delay between adjacent apertures, an image of the object can be subsequently reconstructed.

The aperture spacing, i.e. pixel size in y direction (δy), is chosen to be 300 nm (half the aperture size), so that the line scans properly span the entire sample. The pixel size along x-direction (along the flow direction) is given by the product of the sample velocity (v) and the camera's acquisition time (δt). Finally, we want to note that the sample throughput of the system is proportional to the sample velocity and, hence, is proportional to δx. Therefore, development of high-speed cameras should improve the throughput of future OFM devices as image-based cytometers.

To demonstrate the capability of our OFM prototype for imaging *C. elegans*, we used a collection of wild-type *C. elegans* at the first larval stage (*L1*). We prepared the sample by first euthanizing *C. elegans* in a 70^{o}C heat bath for 3 minutes, and then mixing them with 0.1% Bovine Serum Albumin (BSA) solution. The BSA solution served to reduce adhesion of the targets with the channel walls. Pressure (gravity) driven flow was used to drive the targets through the channel. Note that when the worms entered the channel, their speed were able to reach a stable state almost instantaneously, i.e. the entrance length is estimated to be less than 100 μm.

The nematode concentration in the microfluidic reservoir was approximately 5 *C. elegans* per nL. The average transport speed was 300 μm/s. Given that the CCD pixel acquisition time is 2.5 ms, this velocity gives an effective pixel size along x–direction (δx) of about 750 nm. The maximum achieved throughput of the microfluidic transport was 40 worms per minute. One example of a group of 10 *C. elegans* running through the nanoaperture array is shown in Fig. 4-4 (a): individual nematode larvae generated modulation to the transmission signals through the apertures. Then the compilation of these time-of-flight transmission changes by using the method of Chapter 2 produced the C. elegans images (e.g., Fig. 4-4(b), which is before the scaling of the y axis).

It is worth noting that, at that time, approximately 45% of the acquired images were rejected, due to sample rotation and nematode aggregation. We can expect the yield to increase significantly with better microfluidic system design and finer flow control.

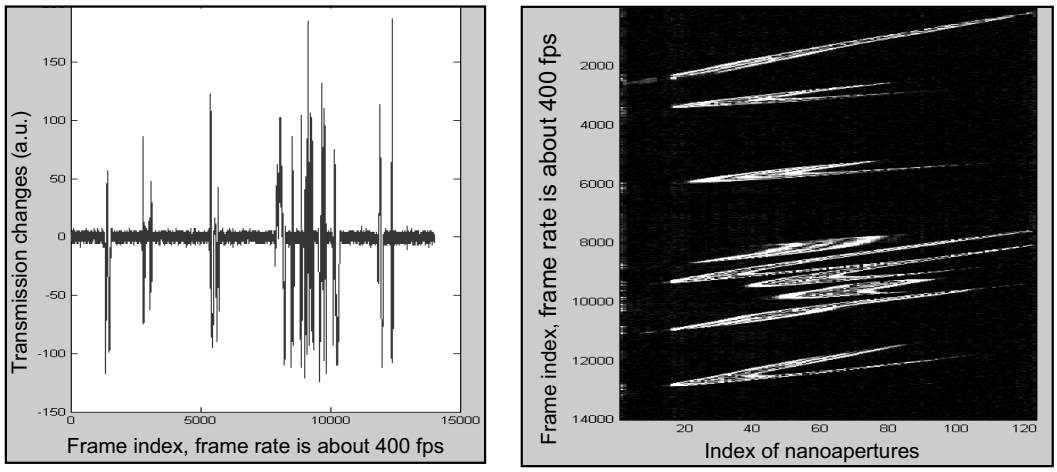

Figure 4-4: (a) The time-of-flight signals from Aperture No. 60 from the array. Each signal modulation indicates the passage of one worm. It was estimated as ~10 worms for 25 seconds. (b) Images of such 10 worms after the correcting the time delay. However, the y axis of the figure is not scaled correctly.

Figure 4-5 (a-f) shows six OFM images of the wild-type *C. elegans*, and Fig. 4-5(g) shows the transmission microscope image of a *C. elegans* taken under similar illumination condition. It can be seen clearly that the OFM is capable of imaging the body profile of the *C. elegans*. In addition, the nematode pharynges are discernable in the OFM images, providing a clear indication of OFM's ability to image targets with resolution comparable to a conventional microscope.

The observable difference in the resolution in the images is attributable to the varying height at which the nematodes flowed across the aperture array – the closer they were to the aperture array, the higher their resolution was. The change in resolution will be discussed in Section 4.3 and also in Chapter 5 and Chapter 6.

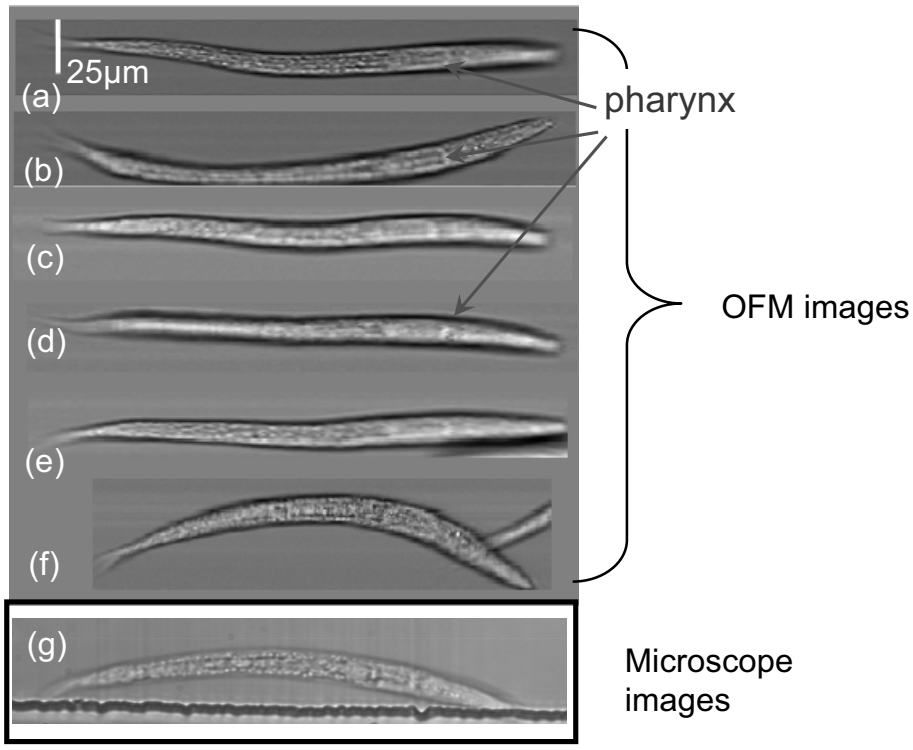

Figure 4-5: (a-f) OFM images of wild-type *C. elegans* at the first larval stage (L1); white bar =25μm. (g) Conventional microscope image (40X objective lens) of a similar nematode.

4.2 Characterization of two genotypes of *C. elegans*

Optofluidic Microscopy, in principle, is an automated imaging technique, i.e. the entire image generation process does not require human intervention. As such, it should enable high-throughout image acquisition and post-processing. Such a key advantage of OFM can be made use of for the phenotyping studies of large population of *C. elegans*.

Phenotype refers to the set of observable characteristics of an individual resulting from the interaction of its genotype with the environment; thus, phenotypes reflect both the nature and the nurture of the organism. Distinguishable phenotypes of an organism could be a large variety of things, including body length, body width, skin color, etc.

We demonstrated the capability of the OFM system in nematode phenotyping applications by using body size and bodily aspect ratio as phenotypic parameters. We acquired OFM images from two separate populations of *C. elegans* larvae: wild type and the mutant dpy-24 (slightly shorter and stouter). The sample preparation procedure was identical, as explained in the previous section. Measurements of body length and body width were taken from the acquired images. The acquired phenotype data is plotted out as an aspect-ratio map (Fig. 4-6).

From this measurement, we found that the average length of wild-type larvae is (240 ± 8) μm, and its average width is (10.8 ± 0.3) μm, which gives a bodily aspect ratio (i.e. length over width) of about (22.2 ± 0.9). On the other hand, the average length of dpy-24 larvae is (210 ± 20) μm, and its average width is (10.7 ± 0.7) μm; this gives an aspect ratio of (19.8 ± 1.3). This initial study shows that the two genotypes, although at *L1* stage, can be separated on the aspect ratio map successfully. The length of the *C. elegans* seems to develop into a more distinguished property between the genotypes.

In addition, the aspect ratio map is consistent with the fact that morphological variance within the mutant group (dpy-24) should be larger than that of the wild-type group. In addition, the dpy-24 mutants should be weakly shorter and stouter than the wild type. Note that better morphological distinction is expected for more grown *C. elegans*; then the phenotype characterization procedure described here will be more appropriate.

The overlap in the two population distributions was not caused by measurement error associated with the OFM system. It can be attributed to a few reasons. First, there is significant size variation within each population group. Second, at the early larval stage, the phenotype difference has not been developed and is thus hardly discernible from the images.

Note that such image based analysis of phenotypes is similar to conventional microscopy based analysis. However, our method is a significant improvement as it can be automated

and thus the throughput is much higher. This is, to our knowledge, the first time that high-resolution nematode imaging and quantitative phenotyping have been performed on a single microfluidic chip.

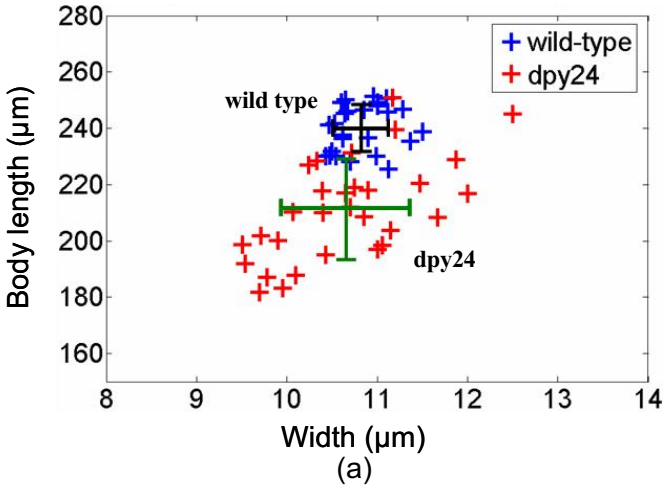

(a)

Genotypes	Wild type	Dpy-24
Body length (μm)	240 ± 8	210 ± 20
Body width (μm)	10.8 ± 0.3	10.7 ± 0.7
Morphological aspect ratio	22.2 ± 0.9	19.8 ± 1.3

(b)

Figure 4-6: (a) Aspect ratio map of wild-type larvae (25 entities); aspect ratio map of dpy-24 mutants (31 entities). The black and green error bars represent the variation span of wild-type and mutant, respectively. (b) Table of the morphology of such two genotypes.

4.3 Characterization of the image properties of the OFM prototype

The image formation process of OFM is not the same as that of conventional microscopy. In conventional microscopy, the resolving power is limited by the light acceptance ability (i.e. NA) of the objective lens and is directly related to the wavelength of the light by

$0.61\lambda/NA$. This property does not apply to aperture based imaging processes, such as aperture-NSOM or OFM. On the other hand, the image formation process of OFM is not exactly the same as that of NSOM. An aperture-NSOM utilizes a sophisticated feedback system to ensure the absolute near-field conditions throughout the entire image acquisition. However, OFM, to some extent, relaxes this strict requirement. As such, the achieved resolution inevitably depends on the specific conditions, under which individual objects were transported. For example, in a taller channel, it is more likely that the object would be far away from the nanoaperture plane and thus would have worse resolution. Such an imaging condition separates OFM from other existing aperture based imaging devices.

There are, therefore, two parameters of interest for OFM imaging: the resolution limit and the experimentally achieved resolution.

First, I would like to quantify the best resolving power of Optofluidic Microscopy. The OFM device can be treated as a parallel set of NSOM probes [5], all of which operate in the collection mode. Therefore, the resolution limit of the OFM can be established by measuring the collection mode point spread function (CPSF) of the aperture. The CPSF is defined as the variation in the transmission through the aperture as a pseudo-point source is laterally scanned across it (Fig 4-7(a)). In other words, the vertical axis of a CPSF plot is the transmission, and the horizontal axis is the lateral displacement of the pseudo-point source from the center of the aperture. The resolution of the OFM for a target at any given plane above the aperture array is given as the width of the CPSF for that plane.

As the CPSF broadens with increasing height from the aperture array, the resolving power of the OFM, likewise, degrades gradually. The exact relationship between resolution and height is discussed in detail in Chapter 5 and Chapter 6. The resolution limit of a given OFM is equal to the width of the CPSF, when the pseudo point object remains a near-field distance from the aperture plane. Practically, this resolution is only attained for parts of the targets that are in near field with the aperture array.

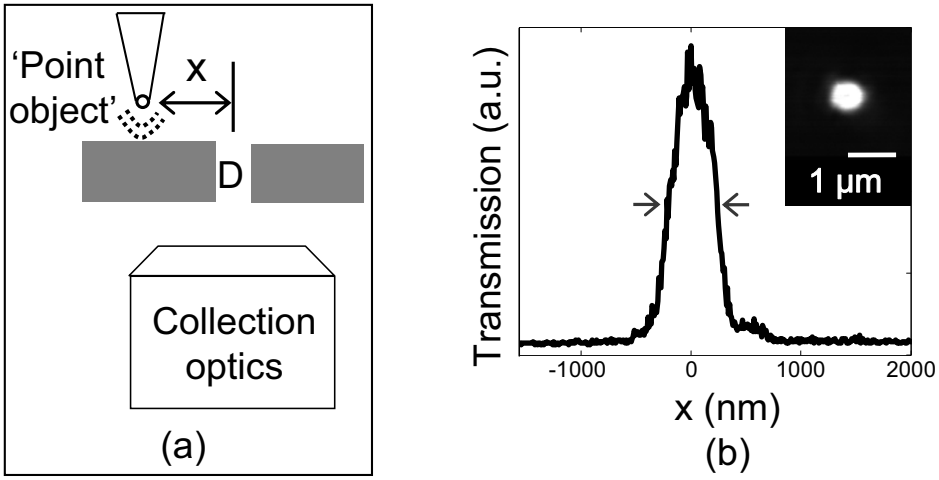

Figure 4-7: (a) Illustration of the experimental scheme of measuring the CPSF: a NSOM tip raster-scans the aperture; the transmission signal is collected through a relay microscope. D=600nm; x: the lateral distance between the NSOM tip and the aperture center. (b) The CPSF extracted from the acquired NSOM image (inset).

We experimentally measured the near-field CPSF of the apertures used in our prototype with a transmission mode NSOM (Alpha-SNOM, WITec Gmbh). The experiment setup is illustrated in Fig. 4-7(a), where the NSOM tip was taken as a pseudo point object. The illumination is provided by a red laser diode (λ= 650 nm, 30 mW). Given that the NSOM tip is 80 nm wide and the aperture is 600 nm in diameter, the approximation of the NSOM tip as a point source is reasonable. Fig. 4-7 (b) shows the measured CPSF profile of the OFM prototype. Based on measurements of 8 different apertures, the resolution limit of our OFM prototype is calculated to be 490 +/- 40 nm (Sparrow's criterion [6]). Note that Sparrow's criterion is independent of the profile of the PSF and thus is an excellent metric to use when we compare resolution of different imaging modalities. The value of the resolution limit (490 nm) is quite smaller than the actual aperture size (600 nm), which is mainly because we chose Sparrow's criterion to measure the width of CPSF. This criterion normally generates a smaller value when measuring profiles of the point spread function.

We note that, as the resolution limit of the OFM is fundamentally constrained by the aperture size, OFM with resolution that is better than the diffraction limit, in theory, can be realized by using smaller apertures. However, to reach this resolution during the imaging process, the target will have to be in contact with the aperture array plane, and the pixel acquisition time will have to be sufficiently short.

Another parameter of interest is the experimentally achieved resolution. While the aperture size provides a good approximation for this parameter, the actual value is likely higher, as all the parts of the sample can not always be kept in near field. We are able to quantify the achieved resolution of our OFM prototype experimentally by the following method.

Some *C. elegans* passed across the aperture array in a "nose-down" fashion, i.e. the front segments of the nematodes were in very close proximity to the aperture array. The acquired images from these nematodes enable us to verify the achieved resolution of our OFM prototype. Fig. 4-8 (a) shows one such image.

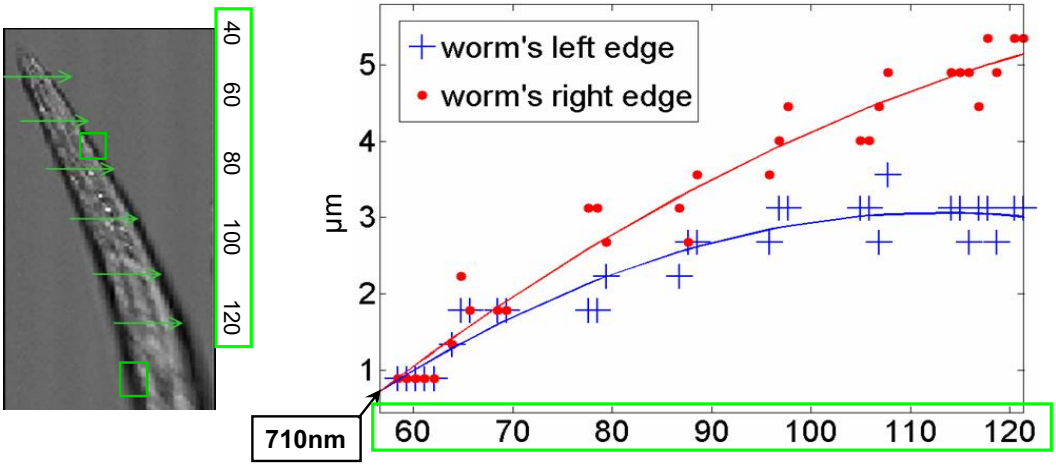

Figure 4-8: (a) OFM image of a "nose-down" worm; the green arrows represent the line scans along the worm's body. (b) Projection plot of the achieved resolution of the current OFM prototype; y-axis: the sharpness of the body edge; x-axis: the horizontal location of the line scan.

By taking line scans across this image, we plotted the relationship of the location of the line scan and the sharpness of its body edge (Fig. 4-8 (b)), where the sharpness is defined as the full width of the body edge that is presented in this image. The measurements from both ends of the worm body converge to 710 +/- 50 nm. This measured resolution is, to some extent, consistent with the predicted resolution of 600 nm as determined by the size of the aperture. 3D finite-element simulation reveals that for this particular case, the smallest height gap between the sample and the aperture is within 150 nm.

Note that this method of checking experimentally obtained resolution is rather superficial. In order to quantify the resolution in this case, a test-target type of object is desired. For example, it will be desirable to image a specially designed microsphere, which has fine and known structures on its bottom portion. A more thorough method to investigate the imaging properties of OFM, or more generally, aperture based imaging devices, will be introduced in Chapter 5 and Chapter 6.

Concluding remarks of this chapter

In this chapter, I have presented in detail the implementation of Optofluidic Microscope and demonstrated OFM's ability with an example of imaging *C. elegans*. The OFM's resolution is not limited by the actual pixel size of the detection sensors (5-10 μm). In addition, the method can potentially be used to create very compact imaging systems. The system demonstrated here could be modified to include real-time phenotype sorting, or automated imaging of a single nematode for life-cycle studies (e.g. a few days). Also, the automated nature and accuracy of the OFM method allows for measuring relatively subtle phenotypic variation within a population of one genotype. Quantitative analysis of phenotypic variance is insightful in studying the effects of environment stress, nutrition and drugs on growth, reproduction, and life span of *C. elegans*. In addition to nematode related research, the OFM can also be used to image other micro-organisms or biological cells that can be suspended in a liquid medium. The simplicity and compact nature of OFM systems

and the fact that they can be produced with existing fabrication technology will translate to their swift adaptation as an important lab-on-a-chip component.

Reference

1.K. Evason, C. Huang, I. Yamben, D. Covey, and K. Kornfeld, "Anticonvulsant medications extend worm life-span.," Science **307**, 258-262 (2005).
2.C. Savage-Dunn, "TGF-β signaling, WormBook, ed. The C. elegans Research Community, WormBook,doi/10.1895/wormbook.1.22.1, ," http://www.wormbook.org (2005).
3.D. Lange, C. W. Storment, C. A. Conley, and G. T. A. Kovacs, "A microfluidic shadow imaging system for the study of the nematode Caenorhabditis elegans in space," Sensors and Actuators B-Chemical **107**, 904-914 (2005).
4.M. L. Adams, M. Enzelberger, S. Quake, and A. Scherer, "Microfluidic integration on detector arrays for absorption and fluorescence micro-spectrometers," Sens. Actuator A-Phys. **104**, 25-31 (2003).
5.B. Hecht, B. Sick, U. P. Wild, V. Deckert, R. Zenobi, O. J. F. Martin, and D. W. Pohl, "Scanning near-field optical microscopy with aperture probes: Fundamentals and applications," Journal Of Chemical Physics **112**, 7761-7774 (2000).
6.T. R. Corle, and G. S. Kino, *Confocal scanning optical microscopy and related imaging systems* (San Diego: Academic Press, 1996).

Chapter 5

THEORETICAL MODELING OF OFM: APERTURE BASED IMAGING DEVICE

In the previous chapter, we have seen that Optofluidic Microscopy, as a new imaging methodology, has a few unique imaging properties that deserve a more detailed study; such properties include the transmission power, the resolution, the image contrast, etc. In addition, the transmission and diffraction of nanoapertures in a plane was usually investigated in either a near field regime or very far field (e.g. >1mm) regime. However, there is a lack of thorough investigation of nanoaperture diffraction scenarios, which are on the order of 100 nm to 1μm away from the nanoaperture plane. Therefore, we applied both a theoretical model and an experimental method to for this study, which is directly related to the imaging performance of an OFM system, more importantly, collection-mode OFM. In this chapter we will first focus on the theoretical method.

5.1 Two different imaging modes of OFM

In the past decade, we have seen a trend of extending the use of sub-wavelength apertures for imaging [1], sensing [2], or spectroscopy [3], as this scanning-probe type of interrogation method can provide superior resolution and sensitivity beyond the scope of conventional methods. Among all the applications, Aperture Based Imaging Devices (ABIDs) are related to our interest, as OFM is one such subject implemented in microfluidic regime. For the sake of saving words, nanoaperture based imaging devices will be called nano-ABID.

Nanoaperture based imaging devices, i.e., nano-ABIDs, have the potential to deliver ultrahigh resolution that is beyond the diffraction limit, because the resolution of such devices is fundamentally limited by the aperture size, but independent of the illumination

wavelength, or the numerical aperture of any lens involved [1, 4]. The commercial edition of nano-ABID is the renowned near field scanning microscope (NSOM). In Fig. 5-1, we show a NSOM system (Alpha-SNOM, WITec Gmbh), which is installed in the Beckman Institute on Caltech campus.

In addition, the miniaturized version of ABIDs, such as OFM, has the distinct advantage of enabling compact and portable analysis systems. Such unique properties associated with OFM will facilitate the next generation of micro total analysis systems.

In general, there are two categories of ABIDs: in one configuration, the apertures are taken as the illumination sources (type-I ABIDs, Fig. 5-2(a)), while in the other, the apertures are considered as collection units (type-II ABIDs, Fig. 5-2(b)). Note that both configurations are essentially a transmission type of imaging system. In contrast, there is another class of imaging system, i.e. reflection mode ABIDs, where the reflection from the sample is collected. However, in such a configuration, the illumination source and the detectors are usually on the same side with respect to the location of the sample of interest, thus making the device more difficult to miniaturize. As a result, the reflection type of ABIDs will not be the focus of our study, although it should certainly be able to generate enough scientific interest, particularly for surface scientists.

There has been some early work on developing aperture based sensing or imaging devices, which can potentially be the platform for miniaturized ABIDs. One such example is the “near field scanner” developed by Tegenfeldt and his colleagues [2]. This near field scanner is essentially a type I device. Three rectangular nanoslits, instead of circular nanoapertures, were applied to accurately measure the length of extended DNA molecules within a nanofluidic channel. The nanoslit trio functioned as near field illumination sources, and a resolution of 200 nm was reported when the device was tested with fluorescent beads. Such a resolution was reported to be beyond the diffraction limit.

Besides that, the original prototype of OFM [5] developed in our group reported the use of apertures as parallel light collectors to produce a transmission image of an object. It was a type II ABID with similar geometry as Fig. 5-2(b).

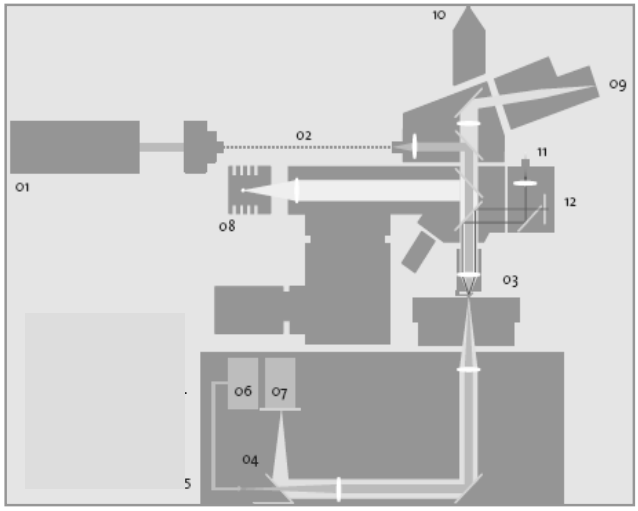

Beam path of the microscope

01. Laser
02. Single mode fiber
03. Cantilever-SNOM-sensor
04. Flip mirror
05. Multimode fiber with SMA connector
06.Dectector
07. Video camera
08. White light source for Kohler illumination
09. Color video camera
10. SMA connector for signal pick-up in reflection
11. FC fiber connector for beam deflection laser
12. Segmented photodiode

From the company, http://www.witec.de/pdf/alphaSnom/alpha300Sflyer.pdf

(a)

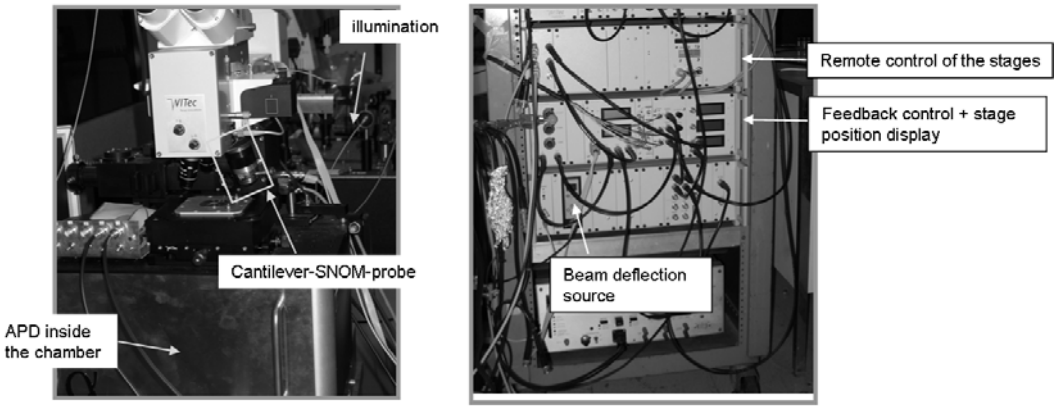

(b)

Figure 5-1: (a) Diagram of the commercial NSOM setup (Alpha-SNOM, WITec Gmbh). (b) Photos of the NSOM setup.

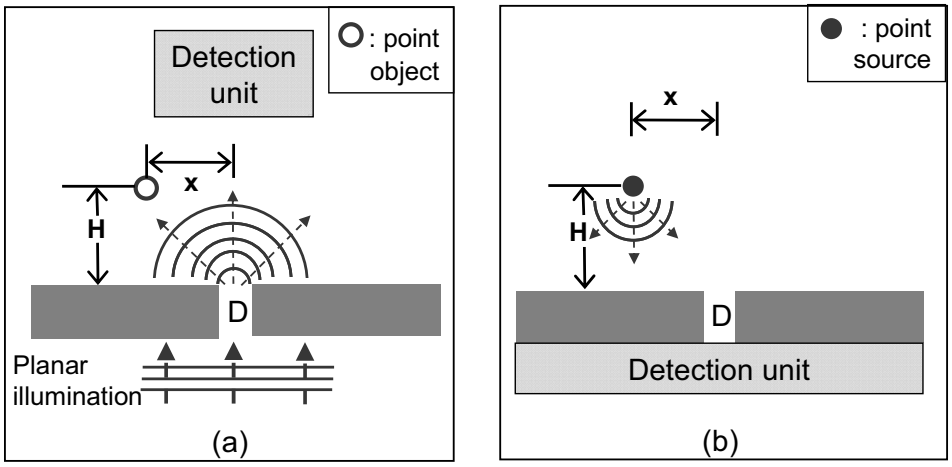

Figure 5-2. Two schemes of subwavelength aperture based imaging devices (ABIDs): (a) Type-I. (b) Type-II. H: vertical separation of the point object (or point source) away from aperture. x: the lateral displacement of point object/source from the aperture.

Type I ABID

The complexity of analyzing the imaging performance of type I and type II ABIDs is quite different. Type I ABID uses nanoapertures as illumination sources; a planar wave incident onto the backside of the aperture generates a specific transmission and diffraction pattern of the near and far field components on the exit side of the aperture (see Fig. 5-3 (a)). Note that I used a nanoslit rather than a circular nanoaperture to exemplify the resolution feature of a type I device.

The near field imaging based on nanoaperture probes or tips can also be explained with this figure. The optical field is very concentrated at the exit of the nanoaperture with a confined spot size of ~58 nm (Fig. 5-3(b)). Imagine there are two nanoscopic scatterers, one is at the center and the other is L=-58 nm away from the center, as indicated in Fig. 5-3

(a, b). The central scatterer being within a much stronger optical field scatters the light much better than the other scatterer does, which is within a weak field. Such a variation in the intensity of the scattered field would generate a point-spread-function-like curve, similar to Fig. 5-3 (b).

As the strength of the scattering field is more or less proportional to the strength of the local field, the width of the original PSF should also be the width of the resulting PSF when using such scatterers as object.

In Fig. 5-3, the associated diffraction pattern, or more specifically, the width of the diffraction pattern, is directly related to the imaging properties of type-I ABIDs. For example, the width of the diffraction pattern on a white screen will be enlarged as the screen moves away from the plane where the aperture is located. Subsequently, the widening of the diffraction pattern means that the resolution of the imaging device is degraded.

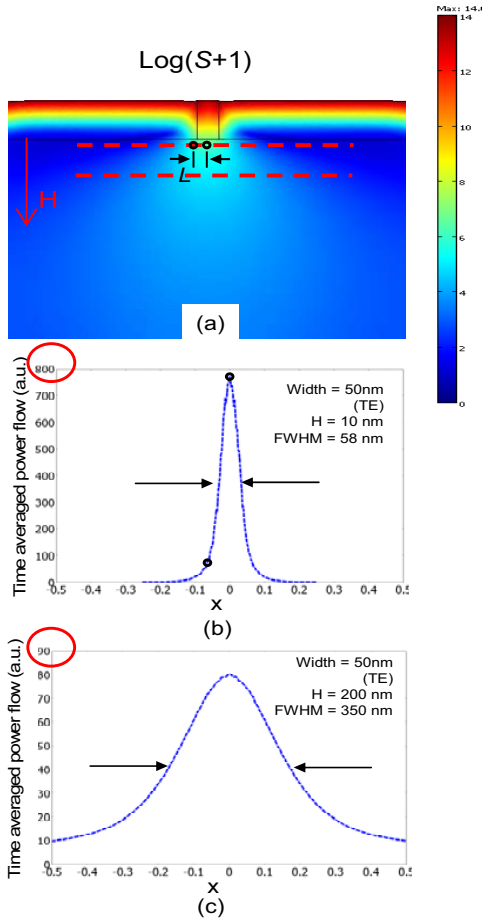

Figure 5-3: Resolution of Type I ABID. A 50nm wide nanoslit is used as an example. (a) The diffraction pattern of the nanoslit. Plotted quantity: (log(S+1)); S: time averaged power flow. (b, c) FWHM of the diffracted pattern when H= 10nm and 200 nm, respectively. The black dots in (b, c) refer to virtual scatterers.

I used $S+1$ such that the logarithm would not return a negative value.

Note that besides the degradation of resolution with increased H, the contrast between the center of the diffraction pattern and its background diminishes rapidly (circled in red).

In addition, as the size of the diffraction pattern gets larger and larger, the contrast between the center of the diffraction pattern and the background will diminish. In a realistic case where noise comes to play, it is inevitable that achievable resolution will further deteriorate because of the lack of contrast.

Therefore, the geometry of studying Type I ABID is rather simple. By studying the transmission and diffraction properties of a single aperture, we will be able to obtain almost complete understanding of type I ABID. Although there has been very little literature on the subject of type I ABID, a large number of articles have been published regarding the subject of light transmission through apertures [6-11], which can all be used to characterize the imaging properties of type I ABIDs.

Finally, I would like to use a simplistic model to discuss the fundamental limit on the smallest aperture size for type I ABIDs. In the limit that the metal film is purely or very highly conductive and film thickness is infinitesimally thin, Bethe [12] showed that the effective transmission area is given is proportional to the sixth power of the aperture's diameter.

In a recent work, de Abajo [13] observed that the transmission is further attenuated exponentially as a function of the thickness of the conducting film. Combining these two effects, we postulate that the effective transmission area can be expressed as:

$$A_T = \left(\frac{16\pi^3}{27}\right)\left(\frac{\pi D^2/4}{\lambda^4}\right)\exp\left(-4\pi d\sqrt{\frac{0.586^2}{\pi D^2/4}-\frac{1}{\lambda^2}}\right) \tag{5.1}$$

where D is the aperture diameter, d is the thickness of the metal film; and λ is the wavelength-in-vacuum.

The formulation agrees well with the simulation data that de Abajo [13] reported. The total transmission photon count for a pixel dwell time τ (also equivalent to the inverse of frame rate) is given by,

$$N_T = \frac{\varepsilon I A_T \tau}{h\frac{c}{\lambda}} \tag{5.2}$$

where $h\frac{c}{\lambda}$ is the photon energy; I : illumination intensity; and ε : quantum efficiency of the camera.

Dominating noise sources include the photon counting noise (shot noise) and the receiver noise ($n_r\tau$). Thus, the sensitivity (SNR, or signal to noise ratio) can be expressed as:

$$SNR = \frac{N_T}{\sqrt{N_T + (n_r\tau)^2}} \tag{5.3}$$

The state-of-the-art nanofabrication technology enables the creation of etching patterns with resolution of 10's of nanometers. Therefore, it should be possible to create OFM devices with resolution of sub 100 nm. Our preliminary estimates based on Eq. (5.1) - Eq. (5.3), shown in Fig. 5-4, predict that with a 600 nm illumination laser, we can easily achieve 40 dB signal sensitivity for OFM with resolution of 100 nm. Note that the far field trend shown in Fig. 5-4 assumed that the effective transmission area is equal to the physical cross section of the aperture ($\pi D^2/4$).

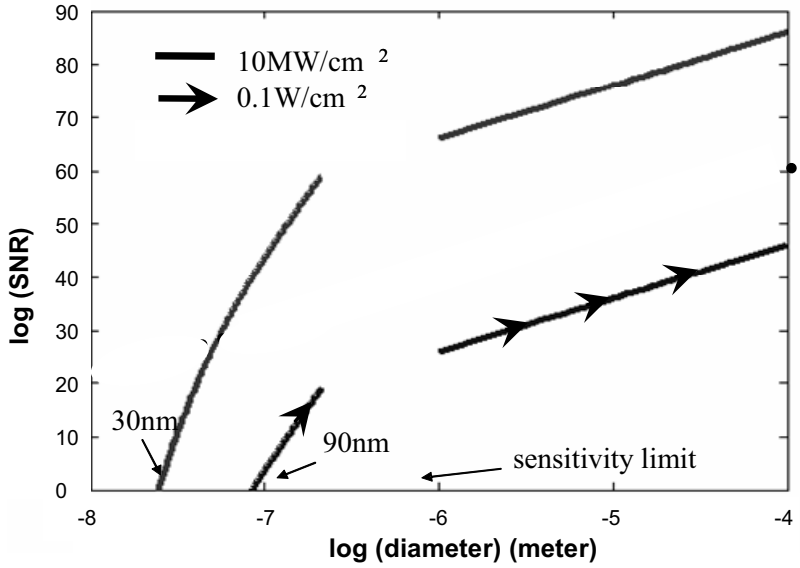

Figure 5-4: Transmission SNR curves for varying aperture sizes at two illumination intensity (10MW/cm2: biological laser illumination intensity limit, 0.1W/cm2: ambient sunlight intensity). The sensitivity curves for the apertures are derived through analysis in two different size regimes.

Type II ABID

Unfortunately, the method that can be used to study type I ABID (illumination type) is not suitable for characterizing type-II ABID, where the nanoapertures function as light collectors. Ideally speaking, the performance of a type-II ABID should be studied with a point source located at varying height (H) and varying lateral displacement (x) from the aperture (see Fig. 5-2(b)).

In order to study this problem, we need to find a light source that can be approximated as a point source or, say, a source with a size significantly smaller than that of the apertures. Unfortunately, a perfect point source is impossible to find experimentally. Even in 3D

simulation, it is hard to implement a point source. Therefore, we had to resort to the second strategy, i.e. looking for a pseudo point source whose size is sufficiently small and then decoupling the size effect out of the system. Such kind of pseudo-point source is necessary in both simulation schemes and experimental methods.

In addition, we utilized a similar method explained in Chapter 4, where we measured the collection mode point spread function (CPSF) of the aperture. The CPSF was defined as the variation in the transmission through the aperture as a pseudo-point source is laterally scanned across it. The major difference here is that the height of the point-like source can vary, rather than remain a near-field distance with the nanoaperture.

The primary objective of this chapter is theoretically modeling the transmission characteristics of a submicron aperture with a pseudo point source. While our focus is to apply our findings to design better type-II ABIDs, this geometry may also be of relevance to research areas, such as near field Raman scattering [14] and near field radiation force [15].

5.2 Simulation scheme: Finite Element Method (FEM)

Although diffraction theory with paraxial approximations works quite well for many macroscale optical systems, such as a phase grating, it often fails in explaining phenomena related to microscale systems. Two major reasons are that, in microscale systems, the object of interest usually has similar or even smaller size compared with the wavelength of light; meanwhile, people are more interested in knowing about the field distribution surrounding the microscale geometry, like a nano crescent [16]. Therefore, the full vector nature of the optical field needs to be considered, i.e. Maxwell's equations are required. However, Maxwell's equations in a realistic 3D case, like type II ABID, cannot be solved analytically because of the complex boundary geometry, such as the sharp edges.

Therefore, such microscale systems are usually investigated with a computation method. So far, a lot of effort has been invested into developing efficient simulation schemes to study the steady state or even transient behavior of microscale photonics systems.

Among a wide spectrum of simulation schemes that are being used in optics studies, two approaches stand out and are relatively more popular than others. They are the Finite Difference in Time Domain (FDTD) method and Finite Element Method (FEM). Therefore, I will like to spend some time explaining these two EM simulation methods.

Note that in my study, I chose to use commercial FEM software (COMSOL Multiphysics) to study type II ABID. However, the FDTD method still has its own advantages, especially for spectroscopic studies.

Finite Difference Time Domain (FDTD)

The FDTD method, first invented by Yee in 1966 [17], is a grid-based time-domain method for electrodynamic modeling. Maxwell's equations (Eq. (5.4) and Eq. (5.5)) are discretized by using central-difference approximations of the spatial and temporal derivatives (Eq. (5.6) and Eq. (5.7), assuming isotropic material).

$$\frac{\partial E_x}{\partial t} = \frac{1}{\varepsilon}\left(\frac{\partial H_z}{\partial y} - \frac{\partial H_y}{\partial z} - \sigma E_x \right)$$

Similar expression for E_y and E_z (5.4)

$$\frac{\partial H_x}{\partial t} = \frac{1}{\mu}\left(\frac{\partial E_y}{\partial z} - \frac{\partial E_z}{\partial y} \right)$$

Similar expression for H_y and H_z (5.5)

$$E_x\Big|_{i+\frac{1}{2},j,k}^{n+1} = \left(\frac{1-\frac{\sigma\Delta t}{2\varepsilon}}{1+\frac{\sigma\Delta t}{2\varepsilon}}\right) E_x\Big|_{i+\frac{1}{2},j,k}^{n} + \left(\frac{\frac{\Delta t}{\varepsilon}}{1+\frac{\sigma\Delta t}{2\varepsilon}}\right) \left[\begin{array}{l} -\dfrac{H_y\Big|_{i+\frac{1}{2},j,k+\frac{1}{2}}^{n+\frac{1}{2}} - H_y\Big|_{i+\frac{1}{2},j,k-\frac{1}{2}}^{n+\frac{1}{2}}}{\Delta z} \\ +\dfrac{H_z\Big|_{i+\frac{1}{2},j+\frac{1}{2},k}^{n+\frac{1}{2}} - H_z\Big|_{i+\frac{1}{2},j-\frac{1}{2},k}^{n+\frac{1}{2}}}{\Delta y} \end{array} \right]$$

Similar expression for E_y and E_z (5.6)

$$H_x\Big|_{i,j+\frac{1}{2},k+\frac{1}{2}}^{n+\frac{1}{2}} = H_x\Big|_{i,j+\frac{1}{2},k+\frac{1}{2}}^{n-\frac{1}{2}} + \frac{\Delta t}{\mu} \left[\begin{array}{l} \dfrac{E_y\Big|_{i,j+\frac{1}{2},k+1}^{n} - E_y\Big|_{i,j+\frac{1}{2},k}^{n}}{\Delta z} \\ -\dfrac{E_z\Big|_{i,j+1,k+\frac{1}{2}}^{n} - E_z\Big|_{i,j,k+\frac{1}{2}}^{n}}{\Delta y} \end{array} \right]$$

Similar expression for H_y and H_z (5.7)

After that, the electrical fields and the magnetic fields of the finite-difference equations are solved in a leapfrog manner repeatedly until the solutions are fully evolved.

In the conventional FDTD method, the uniform rectangular grids are used to discretize the space. That is to say, the entire simulation space is divided into a large number of tiny cubes. The electric fields (*E*) are defined on the edge of the cubical cell, while the magnetic fields (*H*) reside on the center of the cubical walls (Fig. 5-5).

The major advantage of FDTD lies in the fact that the algorithm is easily understood and thus can be quickly put into implementation. The FDTD method also has developed effective absorption boundary conditions (BCs) to truncate the simulation space and good near-field-to-far-field transform methods. In addition, as a time domain technique, the FDTD method can study the behavior of an optical system over a wide spectrum of frequency within a single simulation run.

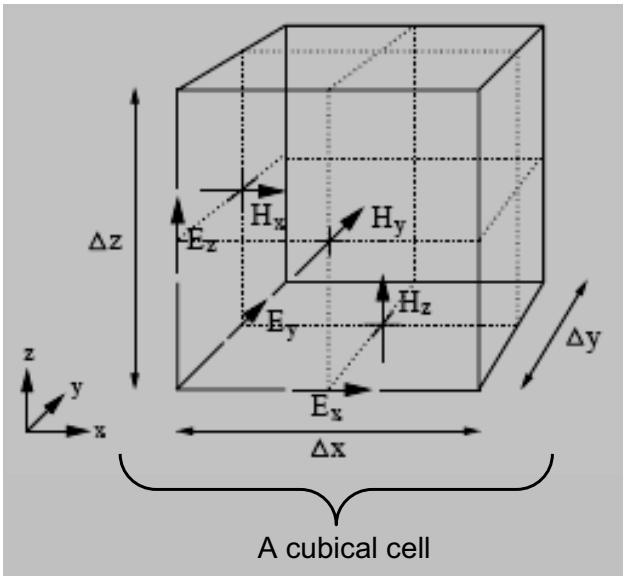

Figure 5-5: A representative FDTD cubical. The electric fields (*E*) are defined on the edge of the cubical cell, while the magnetic fields (*H*) reside on the center of the cubical walls

Nevertheless, FDTD has a few disadvantages. A key one is that the FDTD method utilizes rectangular grids, and thus is unable to map a curved structure effectively. Furthermore, the uniform rectangular grids cannot resolve "nanoscopic" structures (e.g. ~50 nm nano-post array), as it will make the entire simulation space too densely meshed and thus impossible to compute.

Finite Element Method

The finite element method, unlike FDTD, was not originally developed for the purpose of electromagnetic studies. Its early development can be traced back to the 1940's, when FEM was initially used to study complex problems in structural mechanics in the discipline of civil engineering and aeronautics. Commercial FEM software is still routinely used in solid mechanics labs. The fact that the FEM method can be implemented to solve different

physical system also indicates that FEM can be implemented to solve "multiphysics" problem, e.g. coupling the optical trapping problem with the thermal convection problem. In contrast, the FDTD method is incapable of solving such multiphysics problems.

The FEM for electrodynamic modeling is usually a frequency-domain method, i.e. a harmonic wave ($e^{i\omega t}$) is assumed. The solution domain is discretized into small regions called finite elements. The shape of the finite area patch is normally a triangle or a quadrangle. The points defining the region of the element are called "nodes" or "degree of freedom".

The mesh of the FEM, unlike the FDTD method, does not need to be uniform for the entire simulation volume; the shape of the finite element is tetrahedral, instead of cubical. The property of FEM mesh brings forth the major advantage of FEM compared with FDTD, i.e. FEM is better at simulating curved surfaces and optical nanostructures (Fig. 5-6 as an example).

Generally, in electromagnetics, FEM is predominantly associated with one type of residual method, such as the weighted residual method. This particular formulation is simple to implement and normally provides a precise result. Thus, I will only use the weighted residual method to describe briefly the finite element method for electromagnetics. In addition, I will only consider one-dimensional problems to discuss the general procedure of the FEM.

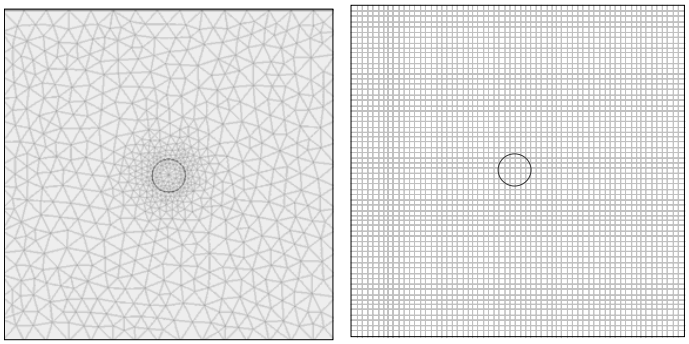

Figure 5-6 (only for tutorial purpose): A nanosphere (D= 100 nm) inside a 1μm cube. Mesh density of a FEM grid (left) is much lower than that of a FDTD grid (right).

Consider a 1D Sturn-Liouville equation as an example:

$$-\frac{d}{dx}\left(p(x)\frac{dU}{dx} \right)+q(x)U(x)=f(x) \tag{5.8}$$

Note that one-dimensional electromagnetic problem is only one set of examples for Eq. (5.8). As a first step, a residual quantity is defined:

$$R(x)=-\frac{d}{dx}\left(p(x)\frac{dU}{dx} \right)+q(x)U(x)-f(x) \tag{5.9}$$

Since *U(x)* is not expected to vary rapidly within a short distance, we discretize the domain into elements and instead enforce the condition over each of the elements

$$\int_{\text{domain of W}_\text{m}} W_m(x)R(x)dx=0 \tag{5.10}$$

where $W_m(x)$ is called a weighting function. From Eq. (5.9) and Eq. (5.10), we can derive the weak form of the differential equation in one dimension:

$$\int_0^{L_m}\left[p(x)\frac{dW_m}{dx}\frac{dU}{dx}+q(x)W_m(x)U(x)-W_m(x)f(x) \right]dx - \left[p(x)W_m(x)\frac{dU}{dx} \right]_0^{L_m}=0 \tag{5.11}$$

Note that by changing this testing interval and W_m, we can construct a set of equations for the solution of the discretized field values.

We can choose a linear representation to discretize *U(x)*:

$$U(x)=\sum_{e=1}^{N_e}\sum_{i=1}^{2}U_i^e N_i^e(x) \tag{5.12}$$

where U_i^e are the unknown coefficients of the expansion, and N_i^e is the shape function (i.e. interpolation polynomials) used to approximate the unknown functions within each element.

After such a discretization procedure, we need to enforce appropriate boundary conditions and assemble the equations for all the elements into a matrix form. Solving the matrix form of the equations usually involve LU decomposition, which is largely an expensive procedure in terms of memory usage. This is arguably one major drawback of FEM.

In my specific case, I have been able to implement COMSOL Multiphysics, a well-developed type of FEM software in the study of my nanoapertures. In order to get accurate solutions, the boundary conditions and the solvers need to be selected carefully. I will provide more details on that topic in the next section.

At last, I want to mention that another advantage of FEM for electromagnetics is that the experimental values of the permittivity (ε) of the materials can be used. On the contrary, as a time-domain method, FDTD requires a full mathematical expression of the permittivity for the entire frequency domain under investigation. Such an accurate formula sometimes does not exist, e.g. microwave properties of steel. Subsequently, the accuracy of FDTD method will thus be affected.

5.3 Simulation implementation: COMSOL Multiphysics

In the section, I will discuss how we applied COMSOL Multiphysics [18] to study the geometry of a pseudo point source scanning over a nanoaperture. The use of a simulation approach, as opposed to an analytical calculation, is necessitated by two facts. First, the finite conductivity and finite thickness of the metal layer needs to be accounted for. Therefore, Bethe's analysis [12] and Bouwkamp's analysis [19] are both inappropriate, as they assumed perfect conductivity of the thin metal film. Second, we need to model the transmission through the apertures for a range of spatial locations of the point source. The lack of spatial symmetry prevents us from simplifying such a structure (Fig. 5-7) into 2D geometry or axial-symmetric 2D geometry.

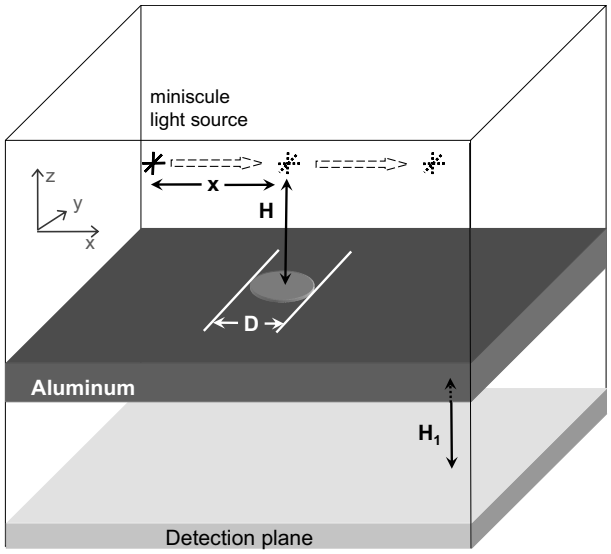

Figure 5-7: Schematic of the simulation geometry. The dashed arrows indicate the movement of the light source in the simulation space. The detection plane is 0.2 μm underneath the subwavelength aperture., i.e. H_1 = 0.2μm (distance between metal's bottom surface and the detector plane). D, H, and x are defined the same way as those in Fig. 5-2(b).

We chose a short antenna, i.e. a Hertzian dipole [20] of 10 nm long as the pseudo point source; length of the dipole certainly is much shorter than the size of the apertures and thus has miniscule effect on the resolution of the nanoaperture. The radiation pattern of a Hertzian dipole is:

$$E = \frac{2I_o(dl)\cos(\theta)}{4\pi\varepsilon\omega}\left[\frac{\sin(\omega t - kr)}{r^3} + \frac{k\cos(\omega t - kr)}{r^2}\right]\vec{e}_r + \frac{I_o(dl)\sin(\theta)}{4\pi\varepsilon\omega}\left[\left[\frac{\sin(\omega t - kr)}{r^3} + \frac{k\cos(\omega t - kr)}{r^2} - \frac{k^2\sin(\omega t - kr)}{r}\right]\right]\vec{e}_\theta \qquad (5.13a)$$

where I_o, ω is the amplitude and frequency of the oscillating electric current inside the dipole antenna, whose length is *dl*. The Z axis of the spherical coordinate system is along

the direction of the oscillating Hertzian dipole. The radiation field (Eq. 5.13 (a)) naturally contains near-field components (the $1/r^3$, $1/r^2$ terms) and real radiating components (the $1/r$ terms), which can be made use of in the simulation. We can imagine that when the dipole is close to the nanoaperture, near-field components of the optical field will predominantly couple with the aperture. However, when the dipole is in far field, only its far field components will matter. The expression of such radiating fields is:

$$E = -\frac{k^2 I_o (dl)\sin(\theta)}{4\pi\varepsilon\omega r}\sin(\omega t - kr)\vec{e}_\theta$$

$$H = -\frac{k I_o (dl)\sin(\theta)}{4\pi r}\sin(\omega t - kr)\vec{e}_\varphi$$

$$S = E \times H = \frac{k^3 I_o{}^2 (dl)^2 \sin^2(\theta)}{16\varepsilon\omega\pi^2 r^2}\sin^2(\omega t - kr)\vec{e}_r \qquad (5.13b)$$

More details in regards to radiation of Hertzian dipole can be found in Chapter 11 of Rao's book [20].

In each simulation run, the dipole was placed at a given height (H) and lateral displacement (x) from the aperture (Fig. 5-7). In addition, for each source location, the orientation of the dipole alternated between three orthogonal orientations - along x-, y-, and z- axes in three consecutive simulation runs. Uniting the resulting radiation fields for these three dipole orientations enabled a more appropriate "pseudo" point source - an approximately isotropic radiation field emanating from the three-dipole combination.

In this study, we calculate the total transmission through the aperture simply as the summation, without weighting factors, of the transmissions from all three dipole orientations. The parameters of the simulations were chosen to match with those of the experiments. That is to say, the thickness of the aluminum film is 60 nm, about nine times of the skin depth (λ_0= 650 nm); the diameter of the apertures (D) ranged from 100 nm to 1000 nm. Note that at near field, H is set to be 5 nm instead zero, which also agreed with the real near field imaging conditions, e.g. the NSOM tip is normally maintained at <20 nm

away from the surface. Note that the dipoles oriented in the x-axis and in the y-axis should be identical due to the symmetry of the geometry.

Figure 5-8 shows two examples of the simulation results with the effective point source at different lateral displacements above the nanoaperture (D= 300 nm), but with the same H (H= 50 nm). In this study, the time averaged power flow (*S*), i.e. Poynting vector, was chosen to quantify the total transmission of the aperture. As illustrated in Fig. 5-7, the total transmitted power is recorded by a "virtual detector" located 0.2 μm below the metal surface. From this light intensity map on the plane of the virtual detector, we can see that the transmission through the aperture can be significantly altered by varying the lateral position of the light source. Such a trend associated with the "walking point source" also explains the resolution of NSOM probes.

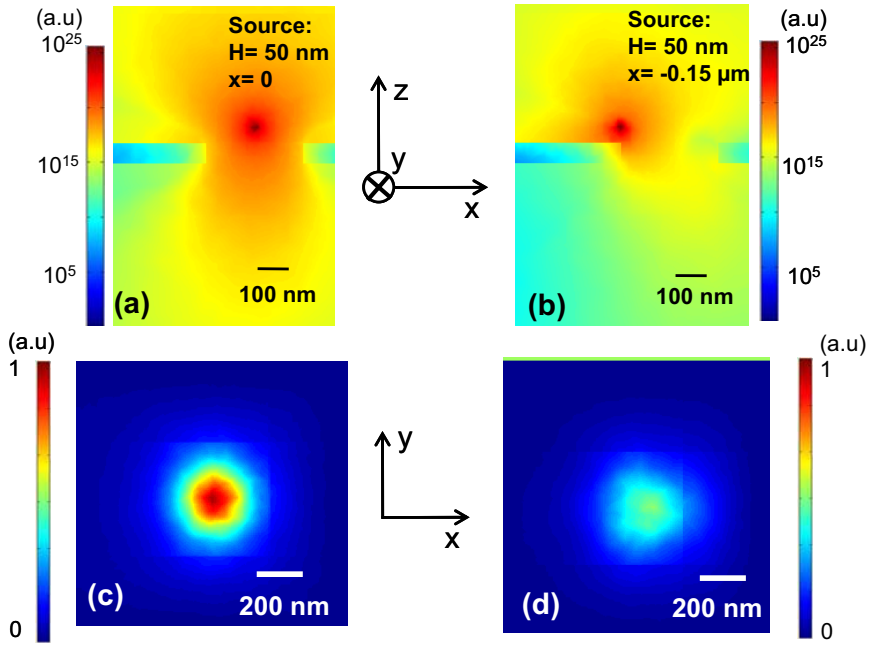

Figure 5-8: Examples of the simulation results with all three polarizations considered. (a) Cross sectional plot of power flow (|S|), time averaged; H=50 nm, D= 300 nm, x= 0. (c) Plot of |S| on the detector plane. (b) and (d) show the corresponding plots when x is changed to x = -0.15 μm.

We can thus produce a complete CPSF by moving the light source across the aperture in the simulation geometry and then plotting out the total transmission as a function of lateral displacement (x) of the source. Fig. 5-9 clearly illustrates the widening trend of the CPSFs with increasing H. In this figure, all the transmission signals have been normalized, and thus the absolute values of transmission cannot be known here. However, I will discuss about the absolute transmitted power later in this section.

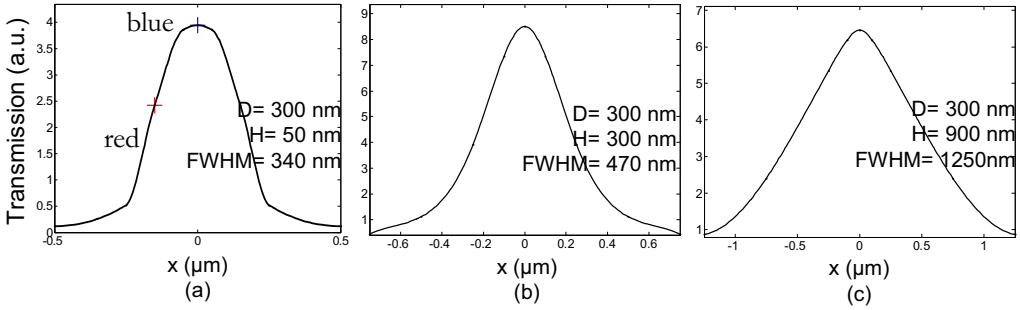

Figure 5-9 (a)-(c) Simulation generated CPSF plots for source at different heights from the aperture. The blue cross and the red-cross indicate the transmissions corresponding to the point source geometries in Fig. 5-8(a) and Fig. 5-8(b), respectively.

COMSOL Multiphysics is somewhat expensive in terms of memory usage, especially when a 3D structure at high EM frequency needs to be studied. It is desirable to have an efficient solver and an excellent absorbing boundary, such that the memory consumption can be minimized. Thus, both the specific solvers recommended for our application and the choice of numerical boundary conditions (BC) for truncating the entire simulation volume deserve detailed discussion.

In this software, the default outer boundaries, i.e. low reflection BC, that encloses the simulation space cause huge numerical reflection errors to the final simulation results, because the low reflection BC is a first-order scattering boundary condition (BC). Usually, the numerical boundaries do not have any a priori knowledge about the incoming electromagnetic waves. As such, approximating the incoming wave cannot be easily described by low order scattering boundary conditions. Consequently, such BCs were not sufficient to suppress or absorb the incoming waves. Subsequently, the incoming waves,

when seeing impedance mismatch at the boundary, reflect from it. This is the why numerical reflections can be generated by an inappropriate BC.

Therefore, designing a proper BC is one of the most significant steps of a computation method. Among all the possible means of solving this problem in electromagnetics, perfectly matched layers (PMLs) invented by Berenger [21] have been accepted as one of the most effective means. As such, we incorporated this scheme into our simulation.

It has been proved that PMLs can be perfectly absorptive, i.e., PMLs do not reflect the incoming wave, no matter what kind of radiation pattern the incident waves has. I do not intend to repeat all the derivations here. The interested readers can check Chapter 9 of J. Jin's book [22] or Berenger's original papers around 1995 [21, 23].

For PML, the refractive index and the absorption of the coefficient can be constant or variant. However, we found that the numerical reflection on the interface between the constant-value PMLs and the real medium (i.e. SiO_2 in our case), though greatly reduced, still exists because of the finite mesh discretization at this interface [21, 22]. Therefore, we adopted a method of variant-PMLs to truncate the computation domain, with the coordinate stretching factor (a_z in z direction) defined as [22]:

$$a_z = 1 - j\left(\frac{z - z_0}{L}\right)^m \delta \tag{5.14}$$

where z_0 is the z-coordinate of the interface between PML and the glass medium, and L is the thickness of PML; m and δ define the absorption property of the PMLs. In x and y directions, a_x and a_y can be similarly defined. In this equation, the complex part of the stretching factor has an m^{th}-order relationship with respect to $(z-z_0)$.

In our study, we chose L= 0.4 μm, m= 2, and δ= 1, which are similar with the PML optimization designs of other computational physicists [21, 22, 24, 25]. After defining PMLs, we chose an iterative solver, GMRES (generalized minimum residual method) with a geometric multigrid preconditioner to solve the 3D computation problem. The mesh step size was no larger than 100 nm for the empty space and was less than 10 nm when near the nanoaperture area. The mesh density has proved to be sufficient to generate a rapid convergence of the numerical solution during the process of iterative computation.

In mathematics, the GMRES is an iterative method for the numerical solution of a system of linear equations. Like other iterative methods, GMRES is usually combined with a preconditioning method in order to speed up convergence of the solution. The cost of the iterations grow like $O(n^2)$, where n is the iteration number. Geometric multigrid preconditioner was actually recommended on the COMSOL manual to facilitate such convergence.

In our simulation implementation, we studied aperture size ranging from 100 nm to 550 nm under both near field conditions and far field conditions. We studied larger apertures, such as D= 800 nm and D= 1000 nm, only under near field conditions. The simulation results will be summarized in the next chapter, where we will compare them with the experimental results conducted with the help of a NSOM system.

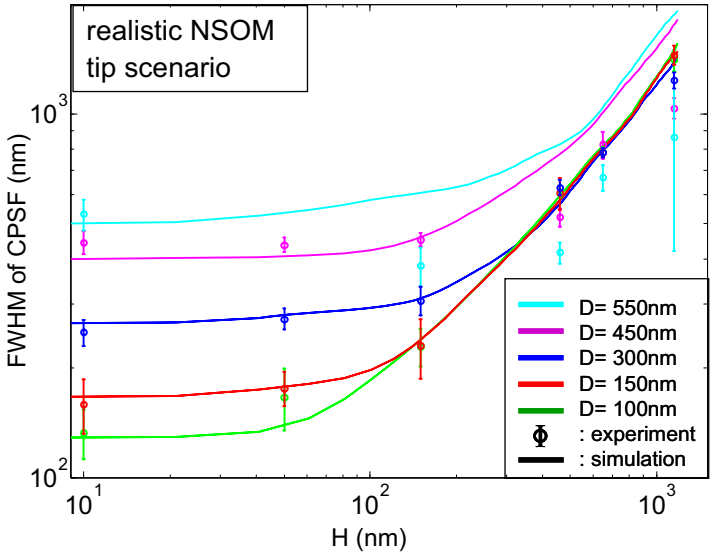

Figure 5-10(log-log scale): CPSF's FWHM *versus* the gap height (H) for a range of aperture sizes (realistic NSOM tip scenario). The lines represent simulation results and the circles represent experimental data. To match with the experimental conditions, only the line sources at lateral directions (i.e. x and y) were considered. The simulation model was adapted to match with the NSOM radiation characteristics. The collection N.A. for the transmission is effectively unity.

However, we can still show the plot of the relationship between the resolution and H by using the simulation results. It can be seen from Fig. 5-10 that nanoapertures of various sizes deliver similar resolution when the object is high above the nanoaperture plane, in which case the resolution is mostly determined by the vertical height, H. Nevertheless, larger apertures will have the advantage, in that they have stronger optical transmission and consequently deliver high image contrast. It will be particularly important when the light power itself is very weak (see the "photon budget" subsection).

Depth of Field (DOF)

The depth of field (DOF) is a quantity that corresponds to the working range in axial direction, or say axial resolution, of an imaging system. In general, an imaging system with high lateral resolution will inevitably have a short DOF, which may limit such a system to surface imaging applications.

Here, we define the DOF to be the height (H) at which the width of the CPSF (FWHM) is twice that of the CPSF when H is near zero. All the DOF values were pulled out from the simulation program. The DOF values for the apertures that are smaller than the wavelength (λ_0= 650 nm) are summarized in Table 1. It is worth noting that the aperture size D appears to be a fine estimate to the DOF. In other words, as a rough rule of thumb, in order to achieve good resolution with type-II ABIDs, the plane of interest of the target object should be maintained at a height (H) no larger than the value of the aperture size (D).

Table 1. Depth of field (DOF) of the subwavelength apertures

	D = 100 nm	D = 150 nm	D = 300 nm	D = 450 nm	D = 550 nm
DOF (Sim.)	130 nm	190 nm	440 nm	500 nm	610 nm

Note: Sim. : simulation.

'Photon budget'

In the end, I will discuss the "photon budget" issue, when realistic experiment constrictions, such as available illumination power, need to be taken into consideration. Such an issue is particularly important for tiny nanoapertures, as the transmission through circular nanoapertures could scale with D^6 [12].

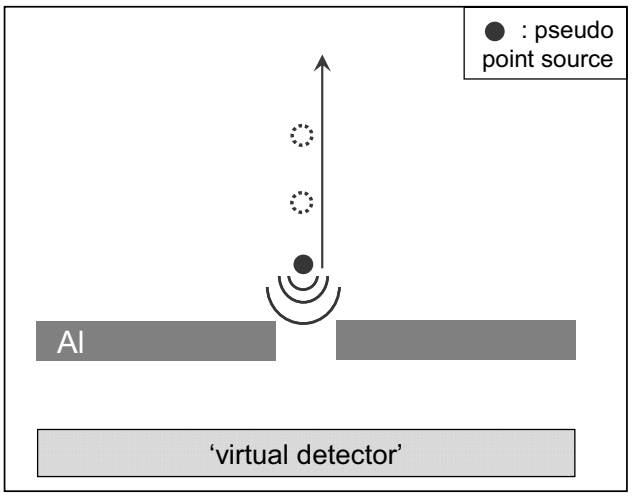

Figure 5-11: Schematic of the computation of the nanoaperture transmission with different H.

Figure 5-12 compares the total transmission from three different sizes (D= 100 nm, 200 nm, or 300 nm) when the light source was located above the center of the nanoaperture (see Fig. 5-11) in the simulation program. The y-axis is plotted out as the ratio of the transmission through larger apertures (D = 200 nm, D= 300 nm) and the transmission through nanoaperture with D = 100 nm.

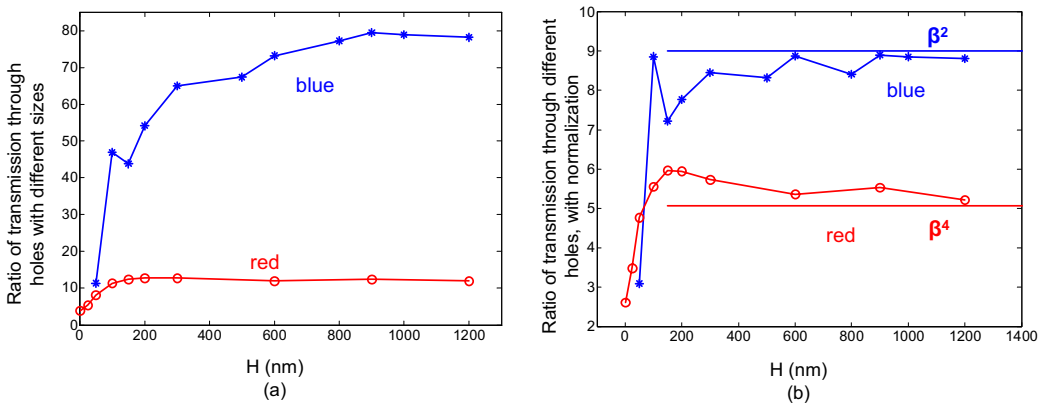

Figure 5-12: (a) Ratio of the transmission through different apertures. H: the height of the line source above the nanoaperture. Blue asterisks: the ratio of transmission through 300nm aperture and 100nm aperture. Red circles: the normalized ratio of transmission through 150nm aperture and 100nm aperture. (b) The ratio of the transmission through apertures with difference sizes with normalization (see Eq. 5.12). β: the size ratio between large aperture and small aperture. Blue dashed line depicts β^2 power law when comparing 300nm aperture and 100nm aperture. Red dashed line depicts β^4 power law when comparing 150nm aperture and 100nm aperture.

It has been shown in Fig. 5-10 that at far field (e.g. H > 300 nm), three nanoapertures give similar resolution. However, in Fig. 5-12, we can see that a 300nm nanoaperture can have total transmission about 75 times of that of a 100nm nanoaperture, while the transmission of a 150nm nanoaperture is about 10 times of that of a 100nm nanoaperture.

It means that using a 300nm nanoaperture will certainly have more advantages than using a 150nm or 100nm nanoaperture in those conditions where the distance between the object and the nanoaperture plane is always larger than a few hundred nanometers. Electrokinetic pumping is one such example. In electrokinetics, it is almost required that the metallic film has to be protected from the fluid by using a thin dielectric layer, normally 100 nm -200 nm thick. As a result, the samples will always be more than 100

nm away from the nanoaperture array. Using a 300nm nanoaperture, therefore, would be sufficient for this experiment.

In addition, we can see from Fig. 5-12 that when the light source is closer to the nanoaperture plane, the difference in transmission of different apertures diminishes. At the same time, a smaller nanoaperture (e.g. D=100 nm) regain the advantages over larger apertures by their ability to deliver better resolution (Fig. 5-10).

It is interesting that an asymptotic trend is shown in both curves of Fig. 5-12 (a), when H is getting larger and larger. The phenomenon is reminiscence of the previous studies of the scaling law of the nanoaperture transmission, which was inspired by Bethe and some other early pioneers more than 50 years ago [12, 19].

In our situation, a point-like source was utilized, while the transmission of nanoaperture is usually studied with plane wave illumination. However, the radiation pattern of a point source will be more and more similar to a plan wave for a tiny nanoaperture, when the point source is getting farther away from the nanoaperture. Note that the intensity of the approximate "plan wave" decreases with larger H. Therefore, the intensity difference between various H should all be normalized by the intensity of the incident wave.

In order to facilitate the comparison of our simulation data at different H, a new function (F) is defined as

$$F(D) = \frac{T}{\iint_{\substack{\text{right above} \\ \text{nanoaperture}}} I(x,y)dx \cdot dy} \tag{5.15}$$

where T is the total power received by the underlying detector, and the integration represents the total light power that is received by the nanoaperture. F functional is apparently a function of the aperture size, and thus we express the diameter (D) explicitly in Eq. (5.15). Fig. 5-12 (b) shows the ratio of $F(D)|_{D=300nm}$ and $F(D)|_{D=100nm}$, and also the ratio of $F(D)|_{D=150nm}$ and $F(D)|_{D=100nm}$.

In Fig. 5-12(b), the red circles indicate the ratio of the normalized transmissions between 150nm aperture and 100nm aperture. To facilitate later discussions, we define

the size ratio of the large aperture and small aperture as β. For example, β=1.5 when comparing a 150 nm aperture with a 100 nm aperture.

It is interesting to note that, at far field, the ratio of the normalized transmission is close to 5.0625, i.e., β^4. The β^4 power law relation was exactly what was obtained when the illumination was planar [12, 19]. It can be qualitatively understood by approximating the spherical wave generated by the point source as a planer wave when the point source is high above the nanoaperture. Under this approximation, the β^4 power law extracted from red circles (with large H) holds up reasonably well. Nevertheless, when H becomes small, the red curve indicates that the ratio of the normalized transmission of 150nm aperture and 100nm aperture becomes smaller. Actually, it becomes a function of both H and β.

On the other hand, blue asterisks on Fig. 5-12(b) represent the ratio of the normalized transmissions between 300nm aperture and 100nm aperture. When the light source is far above the nanoaperture, the ratio of the normalized transmission is close to 9.0, i.e. β^2, which scales differently from the previous case.

In Bethe's theory, the chosen metal is a perfect conductor with infinitely small thickness, and the aperture diameter has to satisfy $D << \lambda$. Both 150nm aperture and 100nm aperture can be considered much smaller than the wavelength (λ_0= 650 nm), and the conductivity of the metallic material, Al is probably the highest among all the metals for such wavelength. Therefore, β^4 law holds up reasonably well. However, 300nm aperture does not satisfy this size condition, and the asymptotic relation of 300nm aperture and that of larger apertures remain unknown from this study. We believe that future studies should consider the size and the geometry of the nanoaperture. Furthermore, it is possible that the illumination condition, e.g. whether it is planar or point like, or how high the point source is located, has some impact on the power law relation as well.

The scaling law disclosed here is far from being solid and complete. My intention was to bring up an interesting topic that may spark further study.

Concluding remarks of this chapter

In this chapter, we first lay out the geometry of two types of aperture based imaging devices and point out the relevance of type II ABID with the Optofluidic Microscope. Then we briefly discussed the two most popular simulation schemes: FDTD and FEM.

The light collection characteristics of subwavelength apertures with respect to point sources at varying heights and lateral displacements from the nanoaperture were studied by using a simulation method. We computed a set of point source scanning situations with apertures that range in size from 100 nm to 550 nm. We used our findings to gain a better understanding of type-II subwavelength aperture based imaging devices (ABIDs). We defined a parameter – collection mode point spread function (CPSF), which is similar to the point spread function for conventional microscopes, and used it to characterize the ABIDs throughout this chapter.

It has been shown that nanoapertures with diameters close to 100nm can deliver ultrahigh resolution in near field. However, such an advantage disappears with increased H. The diameter of the nanoaperture is a good estimate for the depth of field of a type-II ABID. Beyond the depth of field, the resolving power of nano-ABID rapidly degrades. In the end, we discovered that the transmission through different holes under point-like illumination shows the intriguing power law relationship. Such a subject certainly deserves systematic investigation in future.

Reference

1.B. Hecht, B. Sick, U. P. Wild, V. Deckert, R. Zenobi, O. J. F. Martin, and D. W. Pohl, "Scanning near-field optical microscopy with aperture probes: Fundamentals and applications," Journal of Chemical Physics **112**, 7761-7774 (2000).
2.J. O. Tegenfeldt, O. Bakajin, C. F. Chou, S. S. Chan, R. Austin, W. Fann, L. Liou, E. Chan, T. Duke, and E. C. Cox, "Near-field scanner for moving molecules," Physical review letters **86**, 1378-1381 (2001).
3.M. J. Levene, J. Korlach, S. W. Turner, M. Foquet, H. G. Craighead, and W. W. Webb, "Zero-mode waveguides for single-molecule analysis at high concentrations," Science **299**, 682-686 (2003).
4.D. Courjon, *Near-field microscopy and near-field optics* (London: Imperial College Press, 2003).

5.X. Heng, D. Erickson, L. R. Baugh, Z. Yaqoob, P. W. Sternberg, D. Psaltis, and C. Yang, "Optofluidic microscopy- a method for implementing a high resolution optical microscope on a chip," Lab on a Chip **6**, 1274 - 1276 (2006).
6.H. J. Lezec, A. Degiron, E. Devaux, R. A. Linke, L. Martin-Moreno, F. J. Garcia-Vidal, and T. W. Ebbesen, "Beaming light from a subwavelength aperture," Science **297**, 820-822 (2002).
7.H. J. Lezec, and T. Thio, "Diffracted evanescent wave model for enhanced and suppressed optical transmission through subwavelength hole arrays," Optics Express **12**, 3629-3651 (2004).
8.T. W. Ebbesen, H. J. Lezec, H. F. Ghaemi, T. Thio, and P. A. Wolff, "Extraordinary optical transmission through sub-wavelength hole arrays," Nature **391**, 667-669 (1998).
9.X. L. Shi, L. Hesselink, and R. L. Thornton, "Ultrahigh light transmission through a C-shaped nanoaperture," Optics Letters **28**, 1320-1322 (2003).
10.E. Popov, M. Neviere, P. Boyer, and N. Bonod, "Light transmission through a subwavelength hole," Optics Communications **255**, 338-348 (2005).
11.E. X. Jin, and X. F. Xu, "Obtaining super resolution light spot using surface plasmon assisted sharp ridge nanoaperture," Applied Physics Letters **86** (2005).
12. H. A. Bethe, "Theory of diffraction by small holes," Physical Review **66**, 163-182 (1944).
13.F. de Abajo, "Light transmission through a single cylindrical hole in a metallic film," Optics Express **10**, 1475-1484 (2002).
14.D. P. Tsai, A. Othonos, M. Moskovits, and D. Uttamchandani, "Raman-Spectroscopy Using a Fiber Optic Probe with Subwavelength Aperture," Applied Physics Letters **64**, 1768-1770 (1994).
15.K. Okamoto, and S. Kawata, "Radiation force exerted on subwavelength particles near a nanoaperture," Physical Review Letters **83**, 4534-4537 (1999).
16.Y. Lu, G. L. Liu, J. Kim, Y. X. Mejia, and L. P. Lee, "Nanophotonic crescent moon structures with sharp edge for ultrasensitive biomolecular detection by local electromagnetic field enhancement effect," Nano Letters **5**, 119-124 (2005).
17.K. S. Yee, "Numerical solution of initial boundary value problems involving Maxwell's equations in isotropic media," IEEE Transactions on Antennas and Propagation **AP14**, 302-(1966).
18.COMSOL_Multiphysics_3.3, in *COMSOL Inc.* *(http://www.comsol.com/)*.
19.C. J. Bouwkamp, "Diffraction theory," Reports on Progress in Physics XVIII, 35 (1954).
20.N. N. Rao, *Elements of engineering electromagnetics* (Upper Saddle River, N.J. : Pearson Prentice Hall, 2004).
21.J.P. Berenger, "Three-dimensional perfectly matched layer for the absorption of electromagnetic waves," Journal of Computational Physics **127**, 363-379 (1996).
22.J. Jin, *The finite element method in electromagnetics* (New York: Wiley, 2002).
23.J. P. Berenger, "A perfectly matched layer for the absorption of electromagnetic-waves," Journal of Computational Physics **114**, 185-200 (1994).
24.F. Collino, and P. Monk, "The perfectly matched layer in curvilinear coordinates," SIAM Journal on Scientific Computing **19**, 2061-2090 (1998).
25.S. D. Gedney, "An anisotropic perfectly matched layer-absorbing medium for the truncation of FDTD lattices," IEEE Transactions on Antennas and Propagation **44**, 1630-1639 (1996).

Chapter 6

EXPERIMENTAL INVESTIGATION OF COLLECTION-MODE OFM: TYPE II ABID

In this chapter, I will explain in detail how we designed an experiment to measure the "point spread function" of the nanoapertures, which is directly related to the resolution of the type II aperture based imaging device (ABID). Besides this discovery, I will also report our findings about the influence of the numerical aperture (NA) of the collection optics on the achieved resolution of ABID. In the end, by using Sparrow's criterion, we will compare the resolution of ABIDs and conventional microscopes.

6.1 Experimental scheme: 'walking-tip' method

Our first OFM prototype [1] is a type II ABID, where the nanoapertures served as light collection components (Fig. 6-1(a)). In the previous chapter, we concluded that the investigation of type II ABID is more complicated than the study of type I ABID. When investigating the imaging ability of a type II ABID, we should use a point-like object that can travel through the nanoaperture (D) at any programmed height (H).

The smallest object that can fulfill such requirements, as we found, is the probe of a near-field scanning microscope (NSOM), which has a sophisticated mechanical feedback control and a well-calibrated and easy-to-use light collection system. Meanwhile, we would call such a characterization method as the 'walking tip' method.

Note that although metallic nanoparticles can be much smaller than the NSOM probe, it is also exceptionally difficult to trap and manipulate the nanoparticles at will. For example, it is almost impossible to make them scan a nanoaperture at H= 100 nm.

For clarity, we define the collection-mode point spread function (CPSF) as the function of the transmission power versus the lateral displacement (x) of an isotropic point source

that is scanned over the aperture at a fixed height (H), as illustrated in Fig. 6-1(b, c). This CPSF method is analogous to the method generally used for the characterization of a commercial NSOM [2, 3].

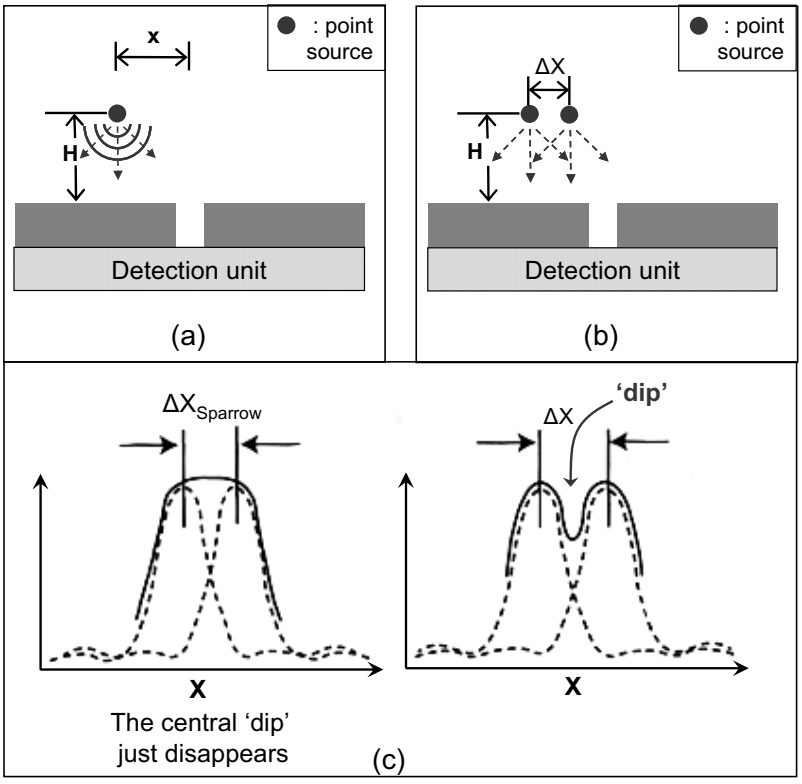

Figure 6-1: (a) Schematic of type II aperture based imaging devices (ABIDs). (b) Illustration of the scheme to measure the resolution of an ABID. (c) Illustration of Sparrow's criterion.

The resolving power of a type-II ABID can be related to the CPSF as follows. Consider two non-interfering point sources of equal strength at the same height (H) with a certain separation (ΔX). The resolution of the type-II ABID is equal to the minimum lateral separation between these two point objects, such that the peaks of their CPSFs are sufficiently separated to be distinguishable. One criterion – the Sparrow's criterion [4],

defines the resolution as the separation between the two point sources to be such that the central dip of the composite point spread function just disappears, i.e. having a zero second-order derivative in the center (see Fig. 6-1(c) as an illustration). One excellent property of such a criterion is that it does not depend on the specific shape of the point spread functions associated with different imaging modalities. Therefore, in the last section of this chapter, I will use Sparrow's criterion to draw a comparison between type II ABID and conventional optical microscopes.

However, in order to keep our measurement and analysis relatively general, we chose to quantify the CPSFs in the following sections by their full width at half maximum (FWHM) – a quantity that is more widely used for characterizing PSFs as they are more easily measured and conceptually simple to understand.

Experimental procedure

The fabrication of apertures of all the sizes is simple. A thin layer (60 nm) of aluminum was coated on a clean quartz slide. Then the apertures are defined on the Al film by using high-resolution focused ion beam milling (FEI nova 200 dual-beam FIB). Aluminum was chosen in our experiment, as it is a highly optically absorptive metal. Its refractive index is given by $n = 1.47 + 7.79\times i$ at $\lambda_0 = 650$ nm [5, 6], which implies an intensity-associated skin depth of 6.7 nm. The thickness of the aluminum layer was about 9 times the skin depth and turned out to be excellent at blocking the direct illumination from the laser diode.

FIB normally uses a high-energy and tightly focused Gallium beam to bombard the surface of the substrate physically. The beam width can be less than 10 nm. The advantage of FIB fabrication is that it does not require any use of a lithography mask or photo resist. Actually the whole chemistry involved with conventional lithography process can be skipped. Such a mask-less feature of FIB proves to be very effective during the prototype development of microscale photonic devices.

The aperture diameters ranged from 100 nm to 1000 nm; the aperture size was measured with a scanning electron microscope (SEM) (Hitachi S4100). The SEM images of nanoapertures with a diameter of 100 nm and 550 nm are shown in Fig. 6-2(b, c). For each diameter value, multiple apertures were used in the "walking tip" experiment. These

apertures had sufficient inter-aperture spacing (more than 20 μm) on the metal film, so that the surface-plasmon (SP) induced anomalous transmission of the subwavelength apertures did not occur.

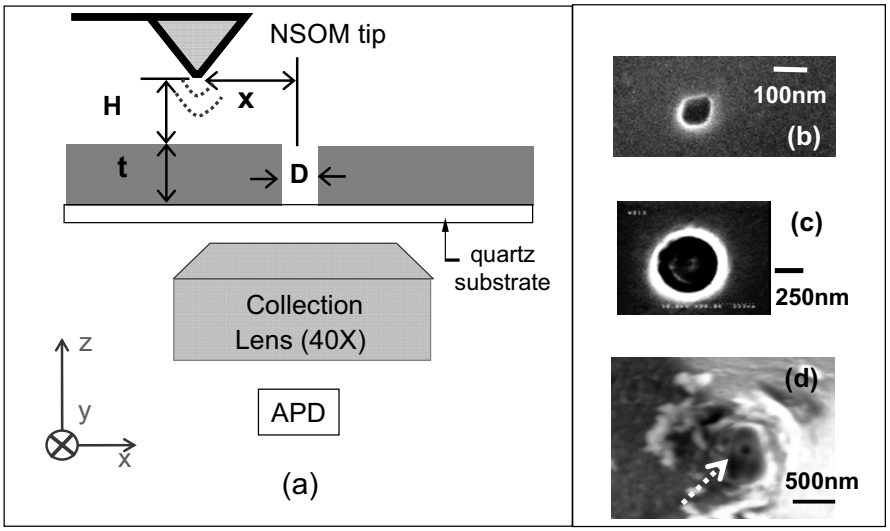

Figure 6-2: (a) Illustration of the experimental scheme. The NSOM tip scans over the subwavelength aperture (diameter: D) milled in a thin aluminum film (thickness: t) at a constant height (H). Substrate is an ultra-clean quartz wafer. x: the lateral distance between the NSOM tip and the aperture center. (b) SEM image of a FIB milled aperture; D=100 nm. (c) SEM image of a nanoaperture; D=550 nm. (d) SEM image of a NSOM tip with a diameter of ~100 nm.

Our NSOM system is a commercial near field microscope (Alpha-SNOM, WITec Gmbh.). In our experiments, as illustrated in Fig. 6-2(a), the NSOM tip scanned over the aperture (diameter: D), at a constant height (H) above the metal surface. The illumination through the NSOM tip was provided by a red laser diode (λ_0 = 650 nm, 30mW). The total transmission through the aperture was collected by a microscope objective (Nikon 40X, NA=0.6) and measured with an avalanche photodiode (AQ series, Perkin Elmer Optoelectronics). Then we characterized the CPSF based on the data we collected (see Fig. 6-3 as an example). Note that NSOM tip can only be engaged with the surface at its near

field. Therefore, we need a method to "defeat" the system and let it work in a far field distance from the nanoaperture plane.

In the first step, we ran the NSOM tip in near field, operating at normal "constant-height" mode, i.e. we preferred that the NSOM tip did not dip into the very small nanoapertures (e.g. D=100 nm). By finely tuning the PID parameters, which we were putting into the shear-force feedback control, we could tell from the topographic image simultaneously obtained with this NSOM probe that the constant-height mode was maintained fairly well. On the other hand, for larger apertures (e.g. D= 500 nm or 1μm), 'constant-height' condition was not required as the change of the height of the tip (<=50 nm) would have negligible effects on the CPSF curve.

In the second step, we deposited a thin film (50 nm) of silicon dioxide (refractive index n = 1.5) by using plasma enhanced chemical vapor deposition (STS PECVD system). The NSOM tip was scanned across the aperture to collect the CPSF profile. In this manner, the NSOM tip will be maintained 50 nm - 60 nm away from the nanoaperture plane. As such, the shear-force feedback control could always engage the tip stably and the tip can maintain a desired distance away from the nanoapertures.

Next, we planarized the nanoapertures by using diluted SU8 resin (Microchem Corp.). The thickness was about 100 nm. Then the "walking-tip" experiment was executed at this accumulated height (~150 nm).

After the planarization step, thin films of S_iO_2 were deposited successively on top of the nanoaperture chip. At each accumulated thickness, the "walking-tip" experiment was carried out, and a film thickness measurement tool (SCI FilmTek 2000) was used to measure the total thickness of silicon dioxide.

Note that we terminated the experiment when the total thickness reached 1.15 μm. Beyond that thickness, the optical signals from nanoapertures e.g., D =100nm were too low to be detected. Furthermore, refractive index of the silicon dioxide layers had also been accounted for in the simulations described in the previous chapter.

Figure 6-3 shows an example of our collected NSOM data; the diameter of aperture in this example is 300 nm. From Fig. 6-3 (a2 → c2) and Fig. 6-3 (a3 → c3), it can be clearly

seen that the measured CPSF of the aperture widens as H becomes larger. It is equivalent to say that the resolution of such a nanoaperture degrades with increasing H.

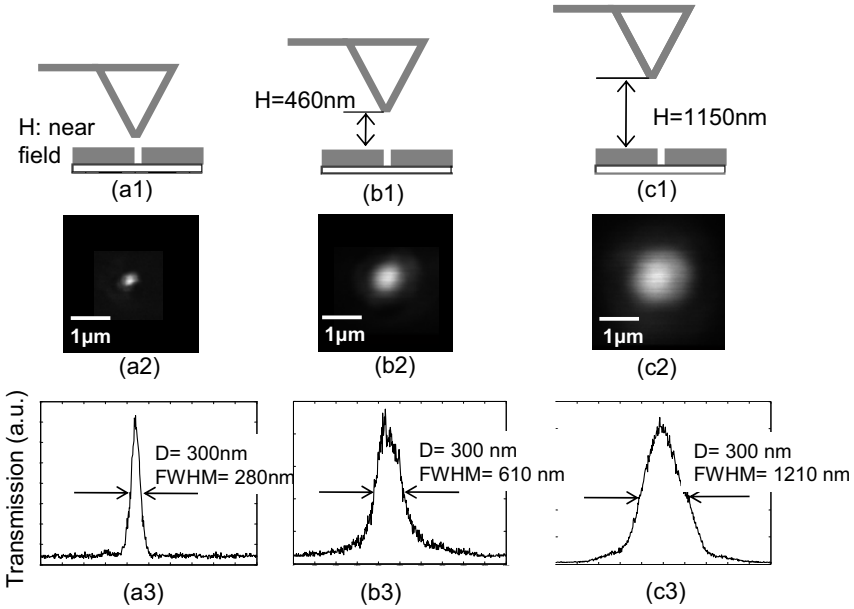

Figure 6-3: NSOM measurements of a subwavelength aperture (D= 300 nm). (a1) An illustration of the experimental scheme, with the NSOM tip engaged in the near field. (a2) The collected NSOM image with the experimental geometry shown in (a1). (a3) The CPSF curve extracted from the NSOM image shown in (a2). (b1) - (b3) The geometry and data, corresponding with H = 460 nm. (c1) - (c3) The geometry and data corresponding with H = 1150 nm.

The described experiment departed from an ideal point-source experiment in three ways. First, as mentioned above, the NSOM tip was approximated as a point source. The finite NSOM tip size (50 nm - 100 nm) can be expected to cause some experimental inaccuracy especially when it was used to quantify the CPSFs of small nanoapertures. Second, the radiation dipole components of the NSOM tip are largely confined to the x-y plane [7], which is a deviation from an ideal point source where the radiation pattern is isotropic. Finally, the transmission through the aperture is collected with a finite NA objective in the

experiment. Ideally, we would want to detect all the transmitted components, i.e. the reception angle should be 180°. These deviations from an ideal experiment were not the result of flawed experimental design, but were instead due to the practical limitations of the available NSOM system.

6.2 Summary of both experimental results and the simulation results

We have mentioned in the previous section that the experimental limitations (such as the finite tip size) could cause system errors in the experimentally measured CPSFs. As such we use the simulation results to "cross-verify" the validity of the experimental data. In this section, we first adjusted the simulation parameters such that they can match the experimental conditions. Specifically, we adapt the light source in the simulations to resemble more closely the actual NSOM tip. Finally, we run the simulations based on ideal experimental conditions and compute the CPSFs for a range of aperture sizes (D) and varying heights (F).

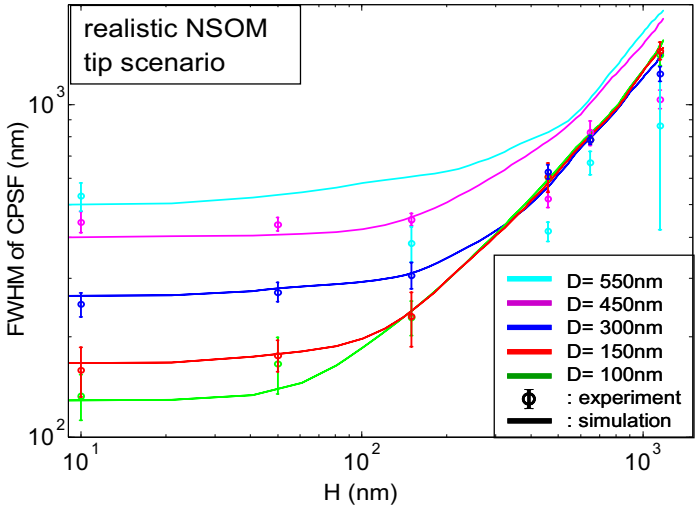

Figure 6-4 (log-log scale): CPSF's FWHM *versus* the gap height (H) for a range of aperture sizes (realistic NSOM tip scenario). The lines represent simulation results and the circles represent experimental data. To match with the experimental conditions, only the line sources at lateral directions (i.e. x and y) were considered. The simulation model was adapted to match with the NSOM radiation characteristics. The collection N.A. for the transmission is effectively a unity.

We experimentally measured the CPSFs for five aperture sizes: 100 nm, 150 nm, 300nm, 450 nm, and 550 nm by using the experimental procedure described in Section 6.1. The dielectric medium has a refractive index of 1.5. In our experiments, the tip height (*H*) ranged from a near field value (≤10 nm) to 1.15 μm. The FWHMs of the measured CPSFs are plotted in Fig. 6-4 (log-log scale).

The data was fit with the theoretical CPSFs profiles obtained by using the EM simulation scheme described in Chapter 5. Nonetheless, we took the following modifications. First, the point source was simplified into a combination of x- and y- dipole components – to better match the radiation pattern of the NSOM nanoaperture probe [7]. Second, we convolved the probe's aperture function (Gaussian with FWHM of 100 nm) with the simulated CPSFs to generate broadened CPSFs that can account for the finite size of the NSOM tip. The simulation results are plotted in Fig. 6-4.

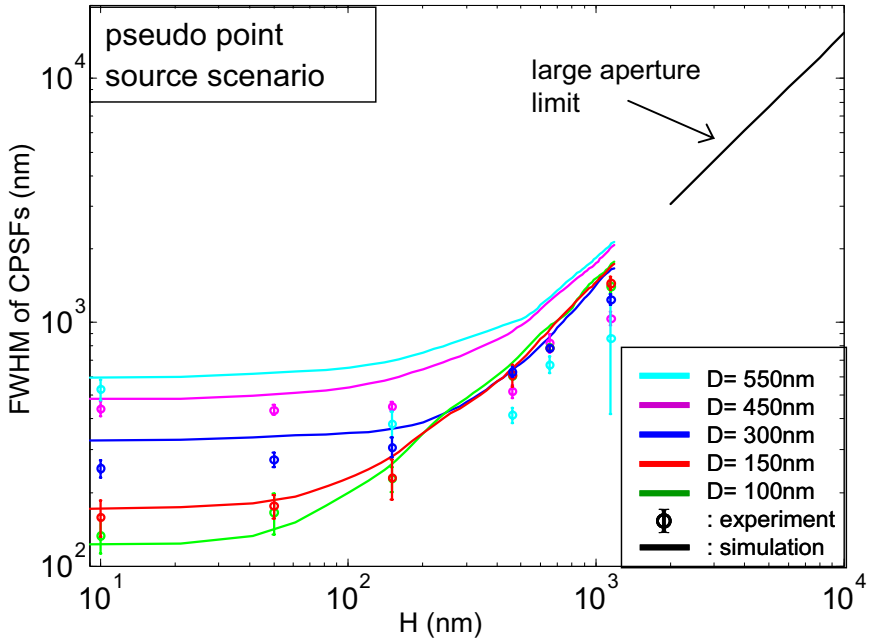

Figure 6-5 (log-log scale): CPSF's FWHM *versus* the gap height (H) for a range of aperture sizes (pseudo point source scenario). The lines represent simulation results and the circles represent experimental data. Line sources of all three orientations were considered - the light source is modeled as an effective isotropic point source. Black line: the far field trend of large apertures (FWHM ~ 1.53 H). The collection N.A. for the transmission is effectively unity.

With the simulation model been validated, we proceeded to compute the CPSFs for apertures of varying sizes based on our model description. The FWHMs of the CPSFs are plotted in Fig. 6-5. We can see that the widths of the CPSFs are at their minimum when H is small. The respective width matches the apertures' size. Such a finding is consistent with our expectation that the resolution of type-II ABIDs is determined by the aperture size and that the best resolution is achieved when the aperture is close to the target, which is also a well-known property of near field optical imaging.

The goodness of fit between simulation result and experimental data (see Fig. 6-4 and Fig. 6.5) is excellent for most of the data points. However, the experiment and simulation do deviate significantly for the last three points of the data set for the 450 nm diameter apertures; for most of the data sets for the 550 nm diameter aperture, the difference is even more pronounced. The measured width of the CPSF for that aperture size actually dipped as a function of H – a counter intuitive behavior.

After examining the experimental setup, it was speculated that this discrepancy between the simulation and the experiment could be attributed to the finite numerical aperture (NA) associated with the collection optics in the experiment. By contrast, the simulation uses a geometry that provides nearly perfect collection of the transmitted light.

Such a limited NA issue was more significant for larger apertures. During the simulation, we found that the transmitted EM waves through a large aperture tended to propagate dominantly along the input light field direction (see Fig. 6-6). Due to such directionality, a large fraction of the transmitted light, although it could still be received by a virtual detector in simulation, would miss the collection optics of the NSOM, especially when the incident angle of the incoming light was large. The drop-off in the collected signals for large lateral displacements (x) led to an effectively narrower CPSF and subsequently a lower FWHM value. The observed lower experimentally measured FWHM value is consistent with this explanation (see 450 nm and 550 nm apertures in Fig. 6-4 and Fig. 6-5).

In comparison, a small nanoaperture, although it diffracts the transmission broadly, maintains the direction of diffracted light reasonably well. As such, the width of the CPSF is less affected by the limited NA problem, although the light signals may be weaker. In

section 6.3, I will report our research into the interplay between the measured CPSF and the NA of the collection optics in a different set of experiments.

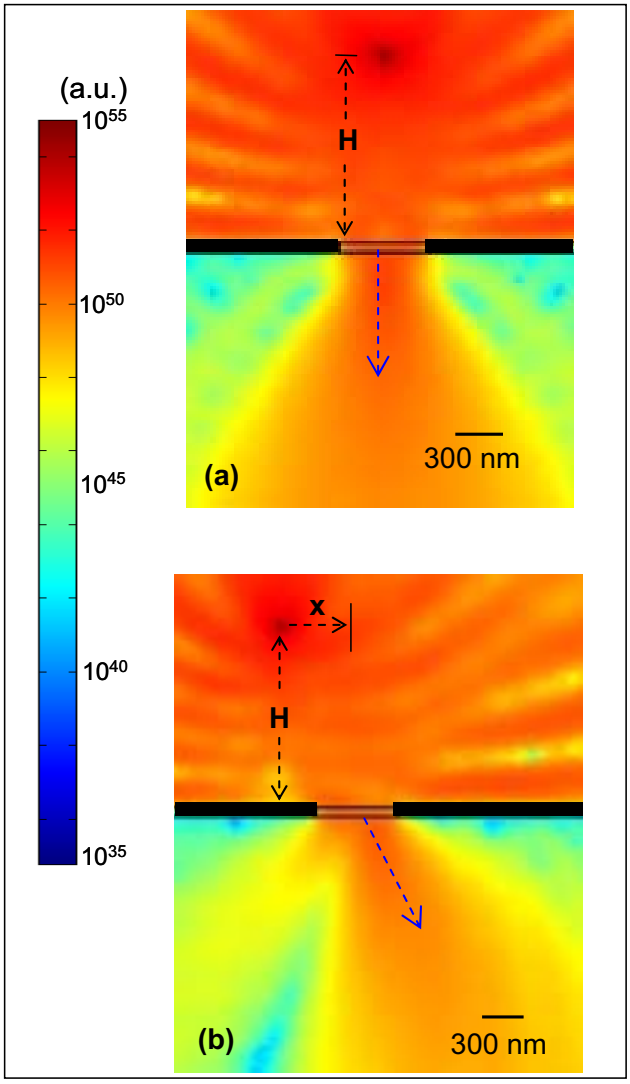

Figure 6-6 (a), (b) 2D cross sectional plots of power flow, |S| for two different lateral displacements: 0 nm in (a) and -500nm in (b). Aperture size is 550 nm; H= 1150 nm.

The resolution of type-II ABIDs and the far field trend

The plots in Fig. 6-5 can be used to characterize the resolution in type II ABID devices. There are a few issues of note. First, as the CPSFs are the narrowest when H is small, we can conclude that a type-II ABID should provide the highest possible resolution when the

target sample is at close proximity to the aperture. For clarity, in our nomenclature, we shall refer to this quantity as the resolution limit. Second, we can see in Fig. 6-5 that as the height (H) of the point source increases, the CPSFs begin to widen. This trend corresponds to degradation of the resolution when the target is at a larger distance from the aperture.

The behavior of the CPSFs' width at large H values deserves some discussion. For large H, the light field incident on the aperture simplifies to a plane wave propagating along the direction from the light source to the aperture. This far field simplification allows us to derive CPSF behaviors for very large apertures analytically. In the large aperture limit, the width of the CPSF should vary linearly with the point source height. The following paragraphs derive the exact relationship.

The transmission areas of very large apertures are assumed to be the same as their physical areas (i.e. $\pi D^2/4$). Therefore, the total transmission (T) through a large aperture is given by the surface integral of the incident Poynting vector (S) over the area of the aperture. The large apertures should not change the direction of the incident light, i.e. the transmitted EM wave should maintain the same direction as the incident wave.

In the far field limit, we can treat the incident light field emanating from a point source roughly as a plane wave. This approximation simplifies the integration to a product of the magnitude of the Poynting vector normal to the aperture ($S_\perp$) and the area of aperture (A):

$$T = S_\perp \cdot A = S(x,H)\cos(\theta)\cdot A = S(x,H)A\sqrt{\frac{H^2}{x^2+H^2}} \propto \frac{A}{x^2+H^2}\sqrt{\frac{H^2}{x^2+H^2}} \qquad (6.1)$$

where $S(x, H)$ is the time-averaged energy density above the open area of the aperture from a point source at height H and the lateral displacement of x between the point source and the aperture; θ is the incident angle with $\theta=0$ representing normal incidence. The proportionality relationship is derived by noting that the light energy density is inversely proportional to the square of the distance between the source and the aperture, i.e. $\sqrt{x^2+H^2}$. The profile of the aperture's CPSF is given by the expression in Eq. 6.1 under the abovementioned assumptions. As such, the FWHM of the resulting CPSF is equal to:

$$FWHM = 2\sqrt{2^{2/3} - 1} \cdot H \approx 1.53H \tag{6.2}$$

Such an asymptotic trend given by Eq. (6.2) with large H is plotted in Fig. 6-5. It is clear that FWHM of all of the CPSFs tend to taper into a proportionality relationship with the source height (H). More specifically, the relationship is almost linear, if not purely linear. While we expected only the simulation results of the larger apertures to show convergence to this trend, it turned out that all of the simulation curves show good convergence to this trend. This convergence suggests that aperture size has weak impact on the CPSF in the far field limit.

We can use a naively simple model to characterize nanoapertures with large H. It is known that nanoapertures can deliver ultrahigh resolution, which is equivalent to saying that nanoapertures have an extremely wide reception angle, i.e. a NA larger than 1.0. As such, no matter what the incident angle is, the nanoaperture can collect it with 100% efficiency. After assuming the "perfect NA", the *cos(θ)* term of Eq. (6.1) can be neglected:

$$T = S(x,H) \cdot A \propto \frac{A}{x^2 + H^2} \tag{6.3}$$

Therefore, the FWHM of nanoapertures should be *2H*, i.e. linear with *H* but with a different factor.

Finally, we will point out that in type-I ABID configuration the PSF's behavior in the far field limit for very large apertures is very different. In type I ABID case, incident planar illumination of wavelength (λ) on the input side of the aperture of size D will result in a well-characterized diffraction pattern on the output side. In the far field regime, Fraunhofer diffraction calculation is valid. Based on such calculation, the diffraction pattern should be described by Airy's disk [8]. Therefore, FWHM of the diffraction profile (i.e. CPSF) is:

$$FWHM = 1.03 \times \frac{\lambda}{D} \cdot H \tag{6.4}$$

Note that the width of the PSF for large aperture type-I ABIDs, unlike the CPSF for large aperture type-II, is indeed dependent on the illumination's wavelength, aperture sizes and the height of the plane of interest. This difference corroborated our early claim that the

two optical geometries (type I and type II) are not optically equivalent, although under near-field conditions, both configurations deliver the same resolution.

6.3 The 'finite-NA' problem and our treatment

As mentioned earlier, NA of the collection optics can affect the observed CPSFs. That is to say, the main direction of diffracted light through a large aperture depends on the incident angle of the illumination light. For example, a certain portion of the diffracted light cannot be received by a 40X objective lens, which has a reception angle of ~100^{o}. Our experimental geometry enabled us to investigate the influence of such a NA issue in more details. This phenomenon needs to be investigated in two scenarios: the small aperture regime and the large aperture regime.

a) Small apertures

First, consider a sufficiently small aperture ($D < \lambda/2$), which functions as a "zero mode waveguide" [9, 10]. The infinitely long version of such a zero-mode waveguide does not support any propagating modes; all the modes are rapidly decaying inside such a waveguide, and the attenuation of the high orders are extremely fast. In other words, the diffraction pattern of the small nanoapertures (short zero-mode waveguides) is mostly determined by the lowest orders of all the decaying "waveguide modes".

Therefore, in the small nanoaperture case, the input light field pattern incident on the aperture has a negligible effect on the transmission pattern. In addition, such an independence of the output diffraction pattern on the pattern of the input light field extends approximately to apertures that are small enough to support only few number of propagating modes, i.e. merely the lowest orders. Fig. 6-7 (a, b) show the results of our simulation results of the transmission through a 300 nm wide aperture for a point source at height H =1.15 μm with two different lateral displacements (x= 0 and x = -500 nm). It can be seen from our simulation that although the strength of the transmission is changed with different x, the output diffraction pattern remains almost unchanged: the major axes

of the diffracted light remain aligned with the Z direction. This finding implies that the finite NA of the objective lens for the collection optics should have little impact on the overall shape of a CPSF profile. The use of large or small NA merely enables the collection of more light or less light transmitted from the nanoapertures.

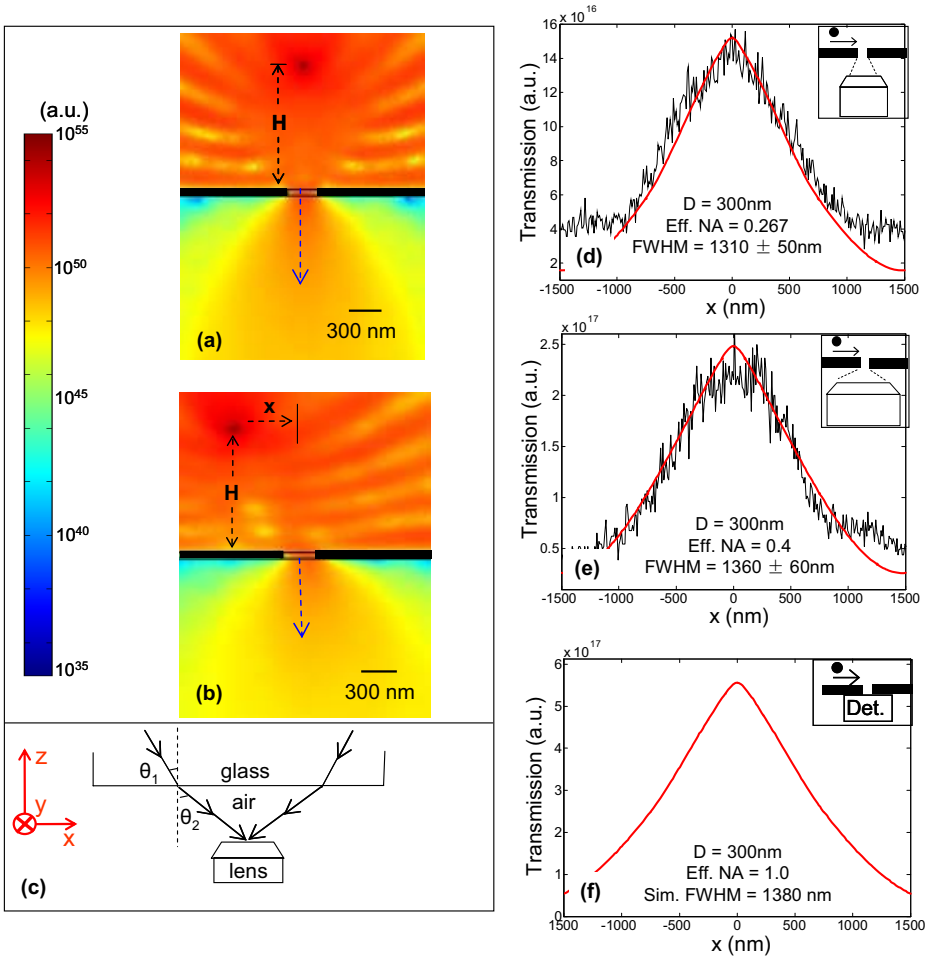

Figure 6-7: (a), (b) 2D cross sectional plots of power flow, |S| for two different lateral displacements. The source lateral displacement is 0 in (a) and -500nm in (b). Aperture size is 300 nm; H= 1150 nm. (c) Light collection geometry in the experiment showing that the effective numerical aperture is reduced by the presence of the quartz wafer. (d) Plots of the CPSFs from experiment (black) and simulation (red dashed). Effective NA =0.267. H= 1150 nm. (e) Corresponding plots in the case where effective NA = 0.4. (f) Simulation CPSF curve with a perfect collection NA, i.e. NA=1.0. (Note that FWHMs indicated in figure (d) and (e) are obtained from experimental results. All the experimental FWHMs are summarized in Table 1.)

Besides simulation, we performed an experiment with a 300 nm nanoaperture to verify this prediction. The point source was scanned at a height of 1.15 μm above the aperture. Two objective lenses (NA = 0.6 and NA = 0.4) were used for this study. Due to the intervening free space between the glass substrate and the collection optics, the effective collection NA was further lowered than that of the cited objective values. See Fig 6-7(c) for an illustration of this consideration. The effective NA values of these two objectives are 0.4 and 0.267, respectively.

The measured CPSFs are plotted in Fig 6-7. As can be seen from the figures, our simulation results agree reasonably well with our experimental findings. First, the measured signal associated with the NA = 0.4 setup (Fig. 6-7(d)) was lower than that for the NA = 0.6 setup (Fig. 6-7(e)); this result is consistent with the fact that the lower NA system would collect less light from the diffracted transmission. For comparison, we also plotted the simulation result for the case where the collection NA = 1.0 (all the light is collected) in Fig. 6-7(f). In Fig. 6-7, the FWHMs of the two experimentally measured CPSFs match up well with the simulation result for the case where the NA is 1.0 (5% and 1.4% difference, respectively). This comparison corroborates our claim about the relative insensitivity of the measured CPSFs on the NA of collection optics for small nanoapertures.

b) Large apertures

In contrast to the zero mode waveguide, a waveguide with a relatively large diameter (e.g. $D \geq \lambda$) supports a number of propagation modes. As such, its truncated counterpart, i.e. a large & shallow aperture, can have quite a few modes transmitting through it without much attenuation.

In this case, the output diffraction pattern from the aperture depends strongly on the the profile and direction of the input light field. We repeated the same simulations as illustrated in Fig. 6-7, but used a 550 nm aperture in the place of the 300 nm aperture. The results are shown in Fig 6-8. As can be seen in Fig 6-8 (b), a laterally displaced point source (x= -500 nm) gives rise to a severely skewed diffraction pattern.

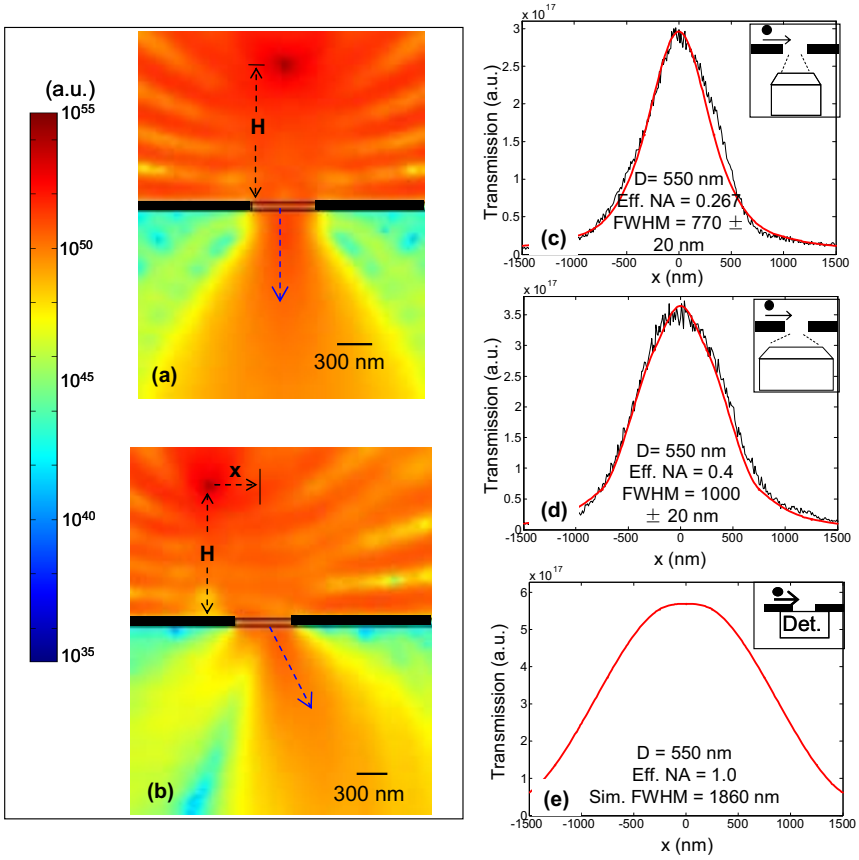

Figure 6-8: (a), (b) 2D cross sectional plots of power flow, |S| for two different lateral displacements: 0 nm in (a) and -500nm in (b). Aperture size is 550 nm; H= 1150 nm. (c) Plots of the CPSFs from experiment (black) and simulation (red dashed). Effective NA= 0.267. H= 1150 nm. (d) Corresponding plots in the case where effective NA = 0.4. (e) Simulation CPSF curve with a perfect collection NA, i.e. NA=1.0. (Note that FWHMs indicated in figure (c) and (d) are obtained from experimental results. All the experimental FWHMs are summarized in Table 1.

In such a situation, the choice of the collection optics' NA would have a significant impact on the observed CPSF. Explicitly, a small NA objective will fail in collecting most of the transmitted light, when the skewed angle of the central diffraction lobe is

larger than the collection angle of the objective. As such, a smaller collection NA system will give a narrower CPSF in comparison to a higher NA system.

This prediction is supported by an experiment with such a 550nm nanoaperture. The experimental setup and parameters are similar to those the 300nm aperture. The measured CPSFs and the simulation profiles are plotted in Fig. 6-8(c, d). The experiment and simulation are again in good agreement. For comparison, we also plotted the simulation result for the case where the collection NA = 1.0 (all the light is collected) in Fig. 10 (e). The measured FWHMs of the CPSF for finite collection NA situations (FWHM = 770 nm for NA = 0.267, FWHM = 1000 nm for NA = 0.40) deviate significantly from the simulation result for the ideal light collection case (FWHM = 1860 nm).

The results of Fig. 9 and Fig. 10 are summarized in Table 1. On the other hand, the finding suggests that it is possible to design type-II ABIDs to have a significantly reduced CPSF for large H values (i.e. far field), and consequently a longer DOF, by restricting NA of the collection optics. Although this method should be valid for relatively large apertures, it will probably have a negligible impact on type-II ABIDs with small nanoapertures. However, decreasing the NA of collection optics will reduce light collection; as a consequence, the sensitivity (contrast) of such an imaging device will subsequently be reduced.

Table 1: Summary of Fig. 6-7 and Fig. 6-8

Aperture Diameter	FWHM of the CPSF Effective NA= 0.267 Experiment (Simulation)	FWHM of the CPSF Effective NA= 0.4 Experiment (Simulation)	FWHM of the CPSF Perfect NA (NA= 1.0) (Simulation)
300 nm	1310 ± 50 nm (1290 nm)	1360 ± 60 nm (1350 nm)	(1380 nm)
550 nm	770 ± 20 nm (710 nm)	1000 ± 20 nm (970 nm)	(1860 nm)

Note: both the experiment data and the simulation data are acquired at a source height (H) equals to 1.15 μm.

6.4 Comparison of nanoaperture based imaging systems with conventional microscopes

In Section 6.1, we introduced Sparrow's criterion, as the use of such a criterion does not assume a particular PSF profile. Thus, it forms a good basis for an unbiased comparison of resolution between systems with different PSF profiles. For example, the PSF of a conventional microscope can be described by a Bessel function [8, 11], while a type-II ABID's CPSF can not. We will use this criterion in our comparison of type-II ABIDs with conventional microscopes.

The CPSF of the aperture functions similar to the PSF of a conventional microscope, as both of them can be used to characterize the ability of the specific imaging system to resolve objects. As mentioned in Section 6.2, the resolution limit of type-II ABIDs is reached only when the target is in close proximity to the nanoaperture. The CPSF widens with an increasing target height (H). This behavior can be found in a conventional microscope as well – the associated PSF rapidly widens when a target moves away from the focal plane of a conventional microscope. In essence, such a downgrade of resolution associated with H is directly related to the axial resolution, i.e. the working distance of the specific imaging system.

Fig. 6-9 shows the measured resolution limit for type-II ABIDs based on our simulation results for a range of aperture sizes, where the Sparrow's criterion was used. We have also included the estimates based on our experimental data in the figure. However, due to the previously mentioned limitations, such as a limited NA, in NSOM experiments, the estimates based on our experimental data tend to over-estimate the resolution. The simulation results are more accurate and unbiased.

Within the range of our measurements, the result shows an approximately linear trend. A fit of the simulation data was added to the plot to indicate the trend, but we note that this linearity may not extend beyond the plotted range and is purely an empirical observation.

Within the range plotted in Fig. 6-9, the resolution limit of type-II ABIDs is consistently smaller than the physical size of the aperture. In fact, the resolution limit is approximately 90% of the aperture's diameter based on our measurements. This

empirical result is useful as a rule of thumb for estimating a type-II ABID's resolution when dealing with aperture diameter in the range of 100 nm to 1000 nm. We do not expect this trend to hold for aperture of all sizes. In the limiting case where the aperture is large (e.g. 100 μm), geometric optics is valid to analyze the system. The optical cross section of a large hole is the same as its physical area in the geometric optics regime. The CPSF at zero height should then be close to a top hat function with a width that is equal to the aperture's width. In that situation, the resolution limit should be equal to the aperture's diameter.

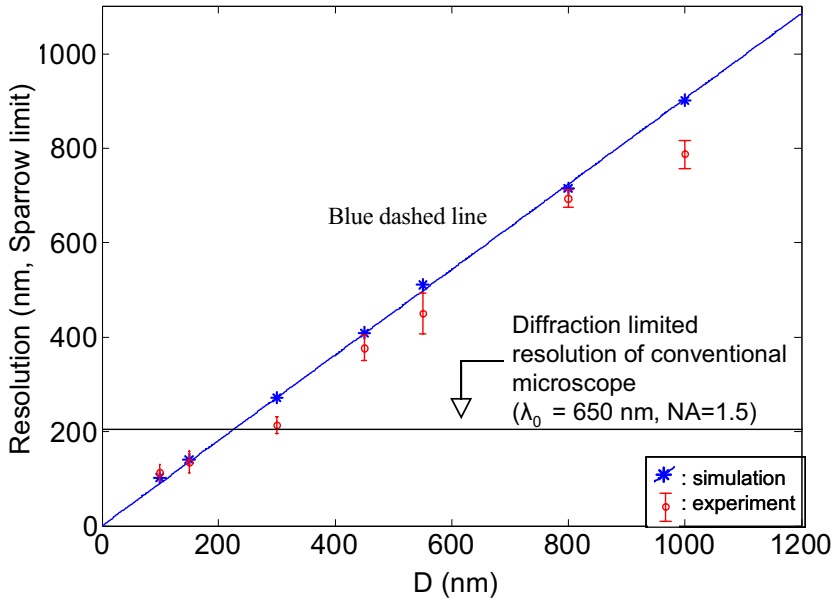

Figure 6-9: Comparison of type II ABIDs with conventional microscopes. Asterisk: Near field resolution of type II ABIDs vs. D (simulation). Simulation assumed an effective isotropic point source. Blue dashed line: linear fit of the resolution limit of type II ABIDs. Red error bars: Near field resolution of type II ABIDs based on our experiment. Black dashed line: diffraction limited resolution of an ideal conventional microscope.

The dashed black line was also added to the plot to show the resolution limit (based on Sparrow's criterion) for an ideal diffraction limited conventional microscope with perfect NA. The medium's refractive index of 1.5 and a free-space wavelength of 650 nm were

used in the calculation to match with the medium and illumination parameters in our subwavelength aperture study. Such a system has a resolution limit of about 200 nm. Based on the observed crossing point of this line with the simulation data fit, we can see that an aperture of size 225 nm can achieve the same resolution limit. Smaller apertures should therefore be more likely to exceed the resolution limit of an ideal diffraction limited conventional microscope, that operates with the same wavelength and the same refractive index.

Concluding remarks of this chapter

It this chapter, we explained in detail our experimental scheme for the investigation of the fundamental imaging properties of type II ABIDs. To our knowledge, we were the first to use a walking-tip method to characterize nanoapertures. At the same time, we also drew a comparison between the experimental results and the simulation results. The agreement between both results is excellent.

Three significant findings were made in the study. 1) We found that, in the far field limit, the width of the CPSF increases linearly with source height (H). Our simulation results indicate that, for far field, the width of the CPSF is only weakly dependent on the size of the aperture. In the far field and large aperture limit, the width of the CPSF is independent of the aperture size. This implies that the CPSF behavior of type-II ABIDs is quite different from the PSF behavior of type-I ABIDs at those limits.

2) In the experiment, the observed CPSF is dependent on the NA of the collection optics that gathers the transmission from the exit side of the aperture. Our study shows that the depth of field associated with apertures can be increased by restricting the NA of the collection optics.

3) We observed an empirical linear relationship between the resolution limit of type-II ABIDs and the aperture size for sizes ranging from 100 nm to 1000 nm. Our study shows that type-II ABIDs based on small nanoapertures can deliver ultrahigh resolution beyond the diffraction limit – a restriction on the resolution of an ideal conventional microscope.

Reference

1.X. Heng, D. Erickson, L. R. Baugh, Z. Yaqoob, P. W. Sternberg, D. Psaltis, and C. Yang, "Optofluidic microscopy- a method for implementing a high resolution optical microscope on a chip," Lab on a Chip **6**, 1274 - 1276 (2006).
2.E. Betzig, J. K. Trautman, T. D. Harris, J. S. Weiner, and R. L. Kostelak, "Breaking the Diffraction Barrier - Optical Microscopy on a Nanometric Scale," Science **251**, 1468-1470 (1991).
3.D. Courjon, *Near-field microscopy and near-field optics* (London: Imperial College Press, 2003).
4.T. R. Corle, and G. S. Kino, *Confocal scanning optical microscopy and related imaging systems* (San Diego: Academic Press, 1996).
5.L. G. Schulz, and F. R. Tangherlini, "Optical Constants of Silver, Gold, Copper, and Aluminum .2. the Index of Refraction-N," Journal of the Optical Society of America **44**, 362-368 (1954).
6.L. G. Schulz, "The Optical Constants of Silver, Gold, Copper, and Aluminum .1. the Absorption Coefficient-K," Journal of the Optical Society of America **44**, 357-362 (1954).
7.D. E. Grupp, H. J. Lezec, T. Thio, and T. W. Ebbesen, "Beyond the Bethe limit: Tunable enhanced light transmission through a single sub-wavelength aperture," Advanced Materials **11**, 860-862 (1999).
8.J. W. Goodman, *Introduction to Fourier optics* (New York : McGraw-Hill, 2004)).
9.E. Popov, M. Neviere, P. Boyer, and N. Bonod, "Light transmission through a subwavelength hole," Optics Communications **255**, 338-348 (2005).
10.M. J. Levene, J. Korlach, S. W. Turner, M. Foquet, H. G. Craighead, and W. W. Webb, "Zero-mode waveguides for single-molecule analysis at high concentrations," Science **299**, 682-686 (2003).
11.S. Inoue, and K. R. Spring, *Video microscopy: the fundamentals* (New York: Plenum Press, 1997)).

Chapter 7

INTEGRATION OF OPTICAL TWEEZERS WITH GRID-BASED OFM

In this chapter, I will introduce a new class of Optofluidic Microscope – Grid based OFM [1], where a closely spaced 2D grid of nanoapertures functioned as an illumination mesh. By optically tweezing a targeted sample and moving it across the grid in a controlled fashion, we were able to generate high-quality images of a few different samples. In the first section, I will describe a special design of optical tweezers for our purpose. Then the layout of the nanoaperture grid will be introduced. In the end, I will present the complete system as well as how we applied it in the imaging experiments.

7.1 Motivation

One of the most popular applications of subwavelength apertures, i.e. nanoapertures, is imaging, i.e. near field scanning optical microscopy. NSOM imaging probes enabled by tiny nanoapertures can deliver resolution beyond that of conventional microscopy [2]. Nowadays, commercial NSOM systems are extensively utilized in the laboratory to discover the miniscule structures of chemical, biological, or geological samples.

However, while the concept of NSOM is simple, NSOM systems, in general, are neither cheap nor fast. A modern NSOM normally includes high-quality illumination sources, a robust 2D scanning stage, a complicated feedback control electronic system, and high-sensitivity optical detectors/cameras. The total price of such an advanced piece of equipment can easily exceed 100K dollars.

The strictest requirement of a rugged NSOM system is arguably the feedback control system to control/monitor the motion of the NSOM probe. In other words, during the image acquisition, the scanning system generally requires sophisticated feedback control to

achieve stable 2D scanning. As such, the whole imaging procedure is very time consuming. Furthermore, it usually takes a long time to train a novice how to use the system.

Last, but not the least, most of the available NSOM systems cannot operate in liquid medium, in which biological samples such as cells are usually kept. Therefore, biological samples usually have to be dried out, to some extent, before being inserting into a NSOM. Such a procedure may diminish the viability of the sample and their normal functioning.

Recently, we have developed a new class of imaging systems - the Optofluidic Microscopy (OFM), which combined microfluidic technology and nanoaperture imaging techniques to create compact and cheap microscopes. Target samples were maintained and transported in liquid media in the entire imaging process. Furthermore, the flexibility of the OFM platform allowed for the use of a wide range of fluid/sample transport mechanisms, such as pressure difference, electrokinetics and optical tweezers.

In our previous work [3], we implemented the first OFM prototype based on a linear aperture array and demonstrated imaging of nematode (*C. elegans*) larvae where the primary fluid transport mechanism was the pressure difference (ΔP).

However, the original 1D array of nanoapertures was lengthy (>500 μm), which was required such that sufficient sampling rate could be achieved. However, biological samples, especially spherical ones, are likely to change orientation during such a long trip, which may diminish the capability of an OFM. In order to reduce the total length of the nanoaperture array and improve OFM's vulnerability to rotation, a shorter nanoaperture pattern is definitely desired. Therefore, in this chapter, we will introduce the implementation of a 2D nanoaperture array (i.e. a grid) instead of the lengthy 1D nanoaperture array.

Some of the key differences of this work from the previous implementation [3] included: 1) the use of nanoapertures as the illumination sources rather than the light collection components. 2) Replacing the linear nanoaperture array with a 2D nanoaperture grid. 3) The use of an optical tweezer to actuate target samples over the nanoaperture grid.

7.2 Optical tweezers and the instrumentation

1) General setup

Optical tweezer, since its invention from the Bell Lab in the 1980's [4], has developed into a mature and popular tool to manipulate micron-sized and even nanometer-sized objects, such as DNA attached microbeads, single biological cells, or metallic Rayleigh particles. An optical tweezer makes use of optical forces exerted by a tightly focused beam of light or, sometimes, counter-propagating beams to realize the trapping of microscopic objects. Objects much smaller than the wavelength (λ), such as nanoparticles develop an electrical dipole moment in response to the electric field of light, whose intensity gradient is usually drawn toward the optical focal spot. Objects larger than the wavelength (λ) act as lenses, thus refracting rays of light beams and redirecting the momentum of photons. The resulting effect is the same: the objects are attracted to the higher flux of photons – the focal point [5].

In fact, there are other schemes which can be used to trap and transport cells. To name a few: Dielectrophoresis (DEP), optoelectronic tweezers, magnetic tweezers, or even photo-activated hydro gel. Compared with these manipulation schemes, one major advantage of the optical tweezer is that it could not only accurately place a cell in a desired location, but it can also robustly transport the cell to other places of interest with pre-programmable speed and direction. Such an advantage in sample manipulation can nicely fit into OFM [3] and other microfluidic devices [6]. In this paper, we will implement an asymmetric optical tweezer for sample actuation.

In Fig, 7-1, I plot out our optical tweezer scanner. A titanium-Sapphire laser (Spectral Physics Tsunami) operating in CW mode was chosen as a source for the laser trap. The wavelength should be selected carefully. Usually light sources at visible spectrum should be desired, as water absorption in this band is minimized. However, it was said that visible lasers are likely to induce two-photon absorptions in endogenous and exogenous cellular components [7], and thus we picked a near-IR wavelength: 850 nm, which has proved to be safe for most biological samples. Another consideration is that we would like to have a slightly longer wavelength such that it can be easily separated from illumination

wavelength and fluorescence wavelength. Note that the imaging experiment will be discussed in more details toward the end of the chapter.

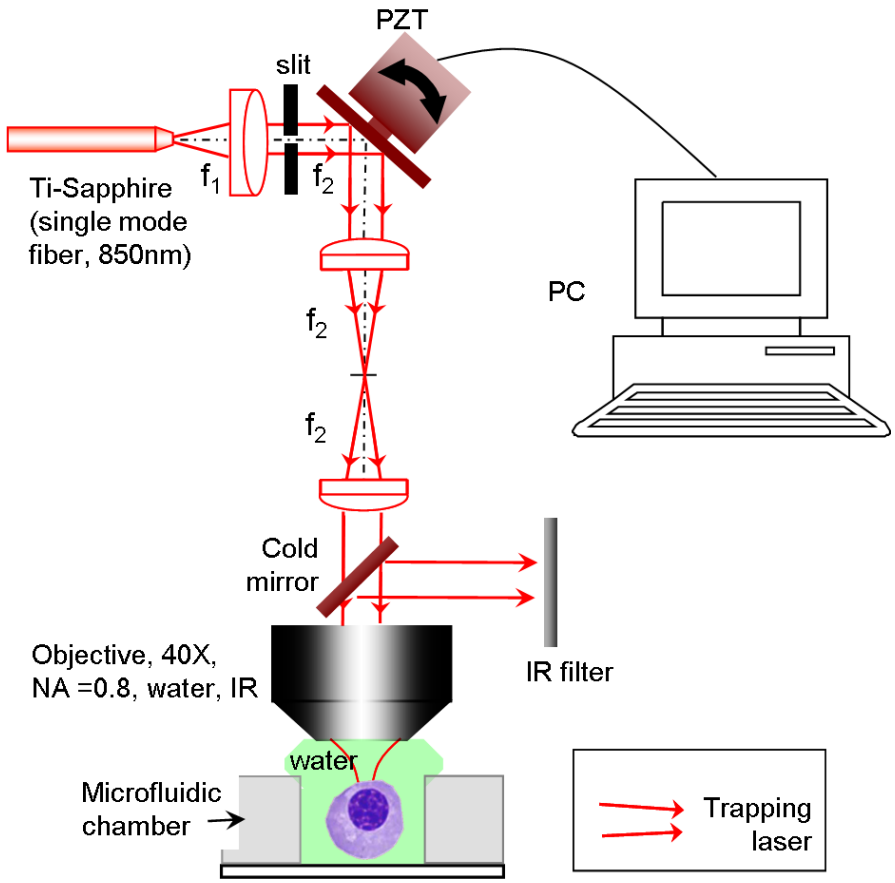

Figure 7-1: Setup of the optical tweezer system. Ti-Sapphire: Ti-Sapphire laser (λ= 850 nm). f1: collimation lens (f1=3.5 cm); f2: 4f scanning system (f2 = 10.0 cm). PZT: Piezo scanning tube (Physik Instrumente S-334). Cold mirror (R: 400-700 nm, T: 780 nm onward, from Newport). Objective lens: Olympus, 40X, NA=0.8, water, IR. Infrared filter: Newport short-pass @ 650 nm.

After setting the laser at the desired wavelength, we coupled it into a single-mode fiber, collimated it by using f_1 lens (beam diameter ~ 8 mm). Then, a PC controlled PZT mirror

scanner (Physik Instrumente S-334) was installed to steer the beam. The motion of the PZT mirror is accurately controlled by using a Labview program.

A 4f lens relay was added into the scanning system, so that when the laser beam was deflected by the scanning PZT, and the geometric center of the laser beam always hit the center of the back aperture of the microscope objective (Olympus, 40X, NA=0.8, water immersion, IR). Note that the 4f relay technique is routinely used in varieties of laser scanning systems.

When the power of the trapping laser is sufficiently high, the sample will be held firmly within the tight focus of the objective lens, and then move together with the scanning beam. The power of the trapping laser at the exit end of the objective lens was set at 20 mW, which proved to be safe enough for the biological samples. Note that the light components of the trapping beam back scattered from the metallic nanoaperture plate are strong and can easily saturate the recording camera's CCD pixels. In order to eliminate this saturation problem, a cold mirror (from Newport) and an IR filter (Newport, short wave pass, 650 nm) are introduced into the system.

One of the strict requirements for OFM implementation is that the sample should not have any rotation or tumbling when passing the nanoaperture array. Note that the array was not shorter than 500 μm in the first OFM prototype [3]. The simplistic pressure driven flow was used in our initial *C. elegans* experiment, which led to a quite high rejection rate: 45%. It was believed that such an issue was merely because of the system's vulnerability to sample rotation. Optical tweezers can address this problem much better, but a little twist in tweezer design is needed.

2) Testing of an 'asymmetric' optical tweezer

Normal optical tweezers with a circular Gaussian beam profile, although they can firmly entrap a micron-sized sample, are not good at controlling its orientation, due to the circular symmetry and the non-polarized nature of the beam. Nevertheless, this also implies that as long as the circular symmetry can break or the polarization of the laser is fixed, then the sample should be able to align with a principle axis and stabilize afterwards. Here, we chose to engineer the beam profile of the trapping laser.

In order to introduce optical intensity anisotropy, we inserted a slit in the laser beam pass-way, as shown in Fig. 7-1 and Fig. 7-2(a). This is because even geometrically circular objects, such as cells, always had slight inhomogeneity in their structures. Therefore, the object would orient with the asymmetric focal spot.

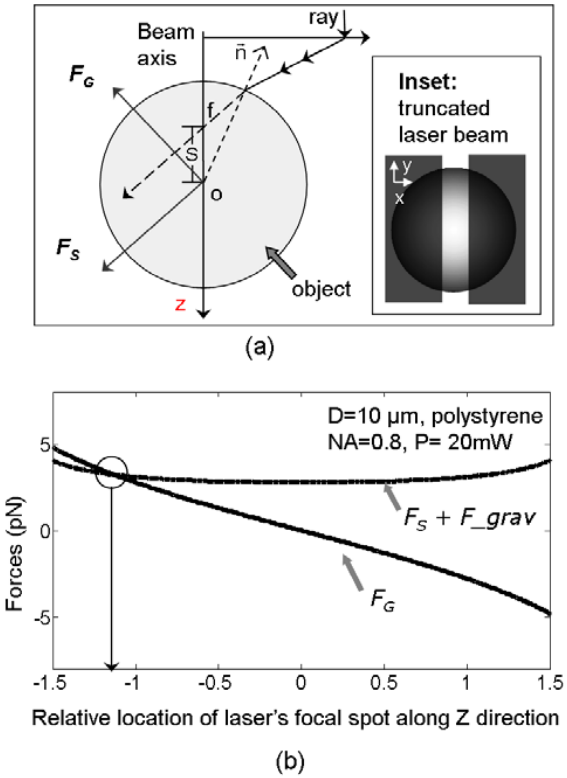

Figure 7-2: Calculation of the strength of the optical tweezer. (a) The diagram of the force (F_Z) calculation. f: focal point; o: center of the object; S: the distance between f and o (|fo|); R: radius of the spherical object. F_S: scattering force; F_G: gradient force. (b) Calculated forces. Relative location is defined as S normalized by R. A solution with |S/R|>1 is not real. D=10 µm, polystyrene bead. NA=0.8, P= 20mW.

This method originally developed by Padgett and colleagues [8] does not require either high-order laser mode or polarization control. However, we have found in our experiment that a laser beam with a 5:1 aspect ratio, i.e. 8 mm : 1.6 mm, was sufficient to suppress sample rotation during the sample delivery. We observed that a trapped sample (pollen

spore) typically aligned with the slit orientation within seconds and the stable trapping condition remained (angular rotation of sample did not exceed 0.01 rad). In such a measurement, the sample was held static and the jittering of a tiny dot near the periphery of the NIST bead was monitored.

Another key requirement for high-resolution nanoaperture imaging is that the sample must be close to the nanoaperture plane because the depth of field of those tiny nanoapertures is extraordinarily small [2, 9]. Optical tweezer setups with a high power IR laser (commonly >100 mW) and a high NA objective lens (usually NA>1.0) can easily lift the sample away from the substrate and hold it within the liquid solution [5, 10]. However, this effect is by no means desirable in the implementation of nanoaperture imaging.

We carefully examined the possibility of sample levitation by tuning the plane of focus of the objective lens and watching how the trapped objects followed. During our tests with micro beads (3 μm -20 μm) and various cells (5 μm -15 μm), it was found that the objects always remained at the same plane as those that are settled and untrapped, while the trapped ones could still be steered in X-Y plane effectively. A computation method originally developed by Ashkin was also used, which I will explain later.

The major reason why the samples are not levitated in our experiment is that we used a moderate laser power (20mW) and an objective lens with a modest NA (NA= 0.8). Therefore, unlike the existing high-power optical tweezers, our system was unable to control the sample in the third dimension, i.e. z direction (Fig. 7-2(a)), which nicely satisfied our need for a close sample-nanoaperture separation.

In order to corroborate our observation, we also adopted a ray approximation method developed by A. Ashkin [11] to calculate the Z-direction forces (F_z) of such an asymmetric optical tweezer. Note that ray approximation is only valid when the size of the samples is much larger that the wavelength. In our imaging experiments, both the micro beads and the biological samples are no smaller than 5μm, which satisfied such a size requirement.

We first used a polystyrene bead (radius D =10 μm, ρ=1.06 g/mL, n=1.57) in our calculation. The laser was non-polarized with a total power of 20 mW; the intensity distribution is Gaussian truncated by a slit with a 5:1 aspect ratio.

The forces that tend to push the microscopic object out of the laser trap include its gravity force balanced by buoyancy (*F_grav*) and the optical trap's scattering force (F_S) [5, 11]. Both forces are in +z direction.

On the other hand, the only force holding the sample within the optical trap is termed gradient force (F_G). This force is in -z direction. Note that both F_G and F_S depend on the location of focal point (f) inside the sample body, while *F_grav* does not. We calculated F_G and *F_grav*+F_S when the location of the focal point (f) swept from the top of the microsphere to its bottom. It is shown in Fig. 7-2(b) that F_G is always smaller than *F_grav*+F_S unless f is above the microsphere (S/R = -1.15), which is merely a virtually existing solution. Therefore, our calculation has confirmed that the inhomogeneous optical tweezer is not able to levitate the microsphere in the vertical direction.

We also ran the calculation for larger (D= 20 μm) and smaller (D= 5μm) microspheres. The results are shown in Fig. 7-3. It was found that larger microspheres are even less likely to be levitated in the Z direction. The smaller microspheres, however, can be lifted theoretically, although it was not observed in our experimental testing. Furthermore, it is worth noting that biological samples should be much more difficult to be raised because of their much lower refractive index contrast with the surrounding water medium (n=1.33).

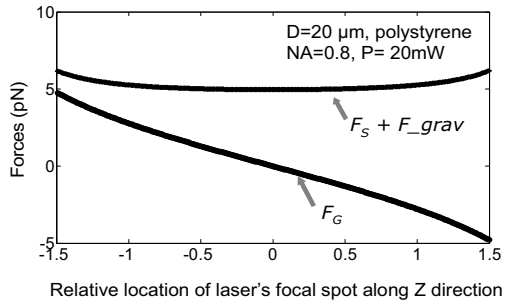

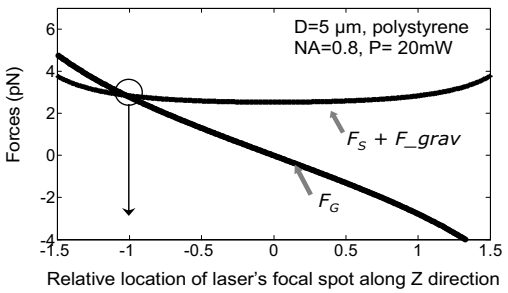

Figure 7-3: (cont'd) calculation of the strength of the optical tweezer. Relative location is defined as S normalized by R. A solution with |S/R|>1 is not real. Polystyrene bead. NA=0.8, P= 20mW. (a) D=20 μm; (b) D=5 μm.

Besides the testing of the axial (Z-direction) control of the optical tweezer, we also examined its robustness of transverse scanning with the use of 10μm polystyrene spheres and 1μm ones. Note that the testing scheme is similar to the equipartition method in optical trap characterization [12].

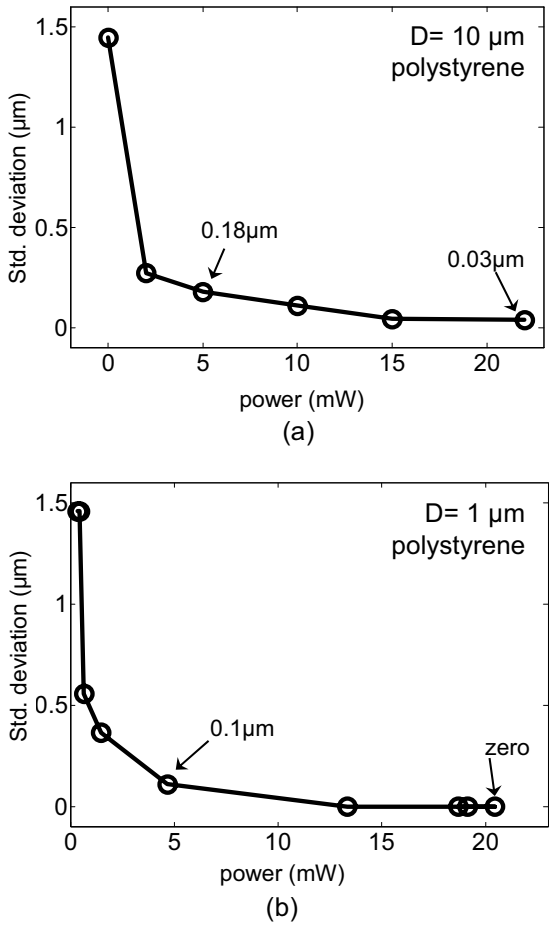

Figure 7-4: Strength of the optical tweezer. (a) The deviation of the microsphere (diameter =10 μm) away from its origin (in the lateral plane). (b) The deviation of the microsphere (diameter =1 μm) away from its origin.

In this assessment, the optical tweezer was not scanned, and the sample was firmly trapped at the origin. Then, the laser power was gradually attenuated so that the optical trap

became weaker and weaker. Eventually, we could see that the microsphere started to agitate/rotate around the origin, and the migration of the microsphere from its original position (measured as standard deviation) was employed to characterize the strength of the optical trap.

From Fig. 7-4, it can be seen that the microspheres were firmly trapped when the laser power was more than 15 mW. Nevertheless, the optical trap became less strong when the laser power was dropped to 10 mW. Eventually, the optical trap became too weak, and the microsphere became totally loose.

Therefore, throughout our experiment, we set the laser power at 20mW such that not only was the asymmetric optical tweezer sufficiently strong, but the sample also could not levitate above the nanoaperture plane.

3) Addition of a fluidic chamber

In our design, we also added an open fluidic chamber made of PDMS on top of the nanoaperture array. Before this addition, we observed that when the fluidic environment is open, i.e. the reservoir is larger than 2 cm, the object that was trapped by the optical tweezer underwent constant vibration primarily because of the agitation from the surrounding bulk of fluid (see Fig. 7-5(a)). By using the same definition as Fig. 7-4, the standard deviation of the migration for a 5μm polystyrene bead in open fluidic environment is approximately 110 nm- 150 nm. However, when we introduced the sample into a microfluidic channel with a cross section of 100 μm (H) x 25 μm (W), the tiny jittering of the microsphere could be improved by about 5-10 times. Later on, we found that adding an open fluidic chamber whose diameter of about 1 mm could give similar results (see Fig. 7-5(c, d)), and thus we adopted this method for its superior simplicity. In our experiment, the rotation angle of NIST beads and pollen spores was less than 0.01 rad.

Another noteworthy advantage of adding a fluidic reservoir or a microfluidic channel is that introducing confined fluidic environment dramatically reduces the appearance of floating objects during the data acquisition. Floating objects, such as microspheres

suspended in the liquid medium could randomly change the light transmission through nanoapertures and bring unnecessary power fluctuation into the system.

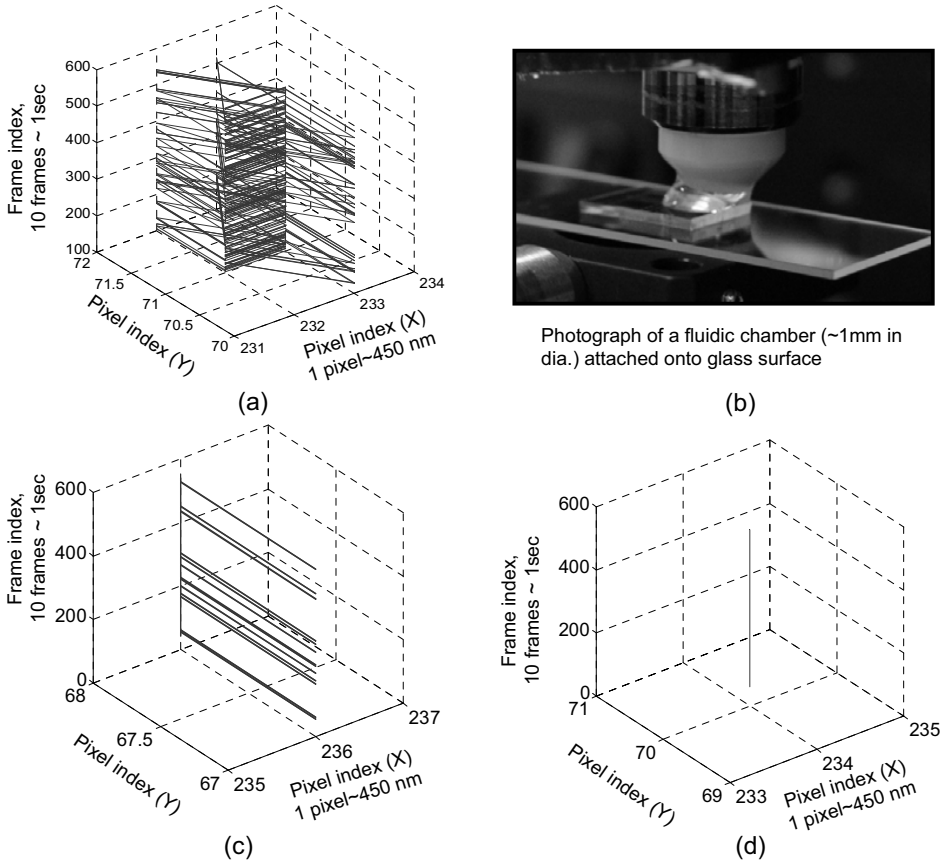

Figure 7-5: (a) 3D rendering of the jittering of the center-of-mass of a 5μm microsphere, in open fluid. Z-axis is equivalent to time lapse. The x and y axes represent the lateral plane: 1 pixel~450 nm. (b) Photograph of a fluidic chamber (~1mm in dia.) attached onto glass surface. (c, d) 3D rendering of the jittering of the center-of-mass of a 5μm microsphere with a small fluidic chamber. Note that in (d), the jittering of the microsphere is literally zero.

7.3 Grid based OFM: operating principles and fabrication

Nanoaperture grid: fabrication and its resolving power

The average diameter of the nanoapertures was 100 nm (as determined by SEM, Fig. 7-6(a)) in this experiment. The adjacent nanoapertures were spaced 2.5 μm apart from each other, so that the light transmissions through neighboring nanoapertures were still able to be resolved on the CCD camera. One such image of the nanoaperture grid is demonstrated in Fig. 7-6(b).

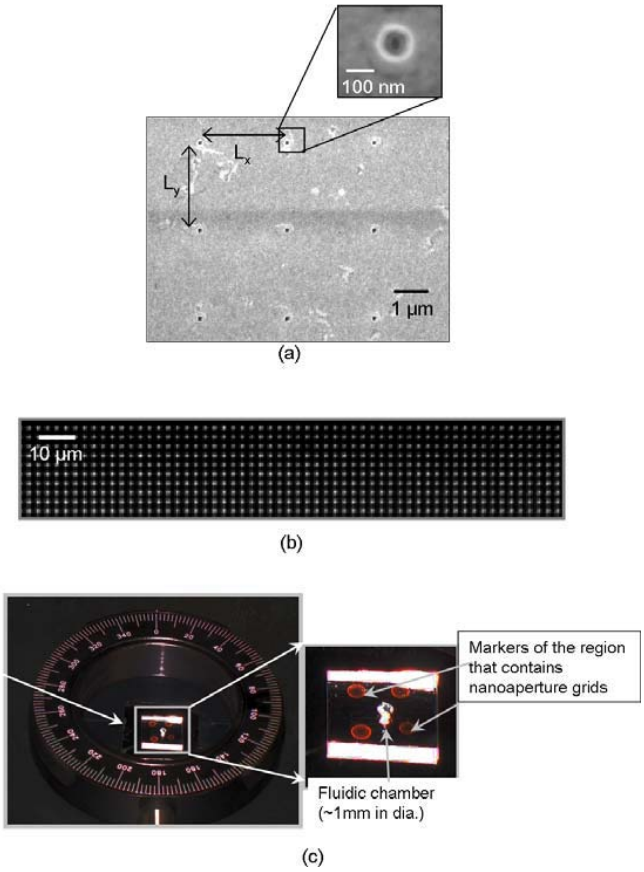

Figure 7-6: (a) SEM image of the nanoaperture grid. The substrate is aluminum. The inset shows one typical nanoaperture (D= 100 nm). (b) The image of the 2D nanoaperture grid shown on the recording CCD camera; there is no sample above this region. (c) Photograph of such a device. The inclusion of a 0-360^o rotation wheel is to facilitate the alignment of the nanoaperture grid with the CCD camera.

Note that small inter-aperture spacing is desired, as it will reduce the total size/length of the nanoaperture array. However, the crosstalk between adjacent apertures due to surface plasmon polarition (SPP) wave needs to considered when the inter-aperture spacing (L) is shorter than or similar with the decay length of the SPP wave.

Surface plasmon waves at the metallic surface decreases as $\exp(-k_x^{"}x)$. The decay length (δ_x) after which the intensity of the SPPs drops to 1/e is then given by [13],

$$\delta_x = \left(2k_x^{"}\right)^{-1} \tag{7.1}$$

where $k_x = k_x^{'} + i \cdot k_x^{"}$

$$k_x^{"} = \frac{\omega}{c}\left(\frac{\varepsilon_1 \varepsilon_2}{\varepsilon_1 + \varepsilon_2}\right)^{\frac{1}{2}} \tag{7.2}$$

There are a few parameters to be clarified. $k_x^{"}$ is the imaginary part of the wave vector of the SPP wave along the metallic surface; ε is the permittivity of the medium, which is illustrated in Fig. 7-7. Therefore, with the knowledge of the optical property of the materials at the specific optical frequency, the propagation length of the SPP wave can be readily obtained.

Table 1 lists δ_x for a few popular metals. The dielectric medium is assumed to be water (n_1=1.34).

However, such formulation (Eq. 7.1 and Eq. 7.2) assumed that the metal film was very thick. In all of our cases, the metal thickness does not exceed 100 nm, and thus we may need to consider the radiation loss of the SPP wave that penetrates through the metallic film and propagates on the other metal/dielectrics interface. The resulting propagation length can be shorter [14]. Besides that, the roughness of the film during fabrication also causes SPP waves to radiate into the dielectric medium, further shortening the SPP propagation length.

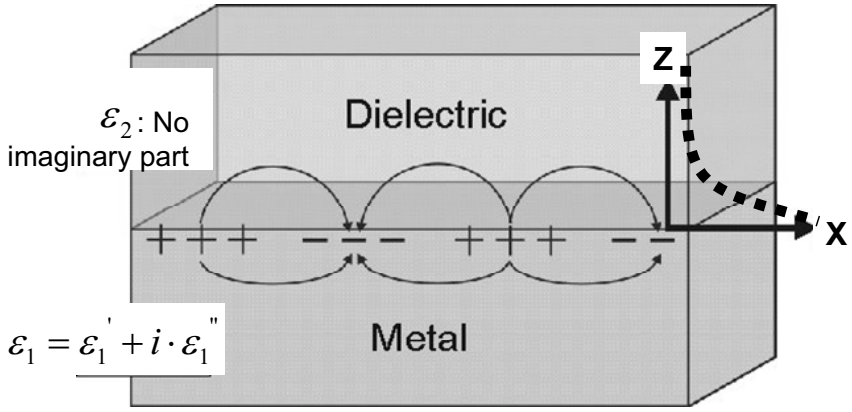

Figure 7-7: Illustration the propagation and damping of the surface plasmon polariton waves on metal-dielectric interface.

Table 1: The propagation length of the SPP waves at the water-metal interface, with different λ.

Metal type	λ in vacuum (μm)	Dielectric constant of the metal (n)	Propagation length (δ_x, μm)
Au	0.532	0.5 + 2.2·I	**0.24**
Au	0.40	1.6 + 2·I	**0.17**
Ag	0.40	0.17 + 1.9·I	**0.2**
Ag	0.532	0.12 + 3.1·i	**3.2**
Al	0.40	0.5 + 4.9·i	**2.8**

We fabricated the nanoaperture grid using the following procedure. First, a clean quartz wafer was coated with a 100 nm thick layer of aluminum by an electron-beam evaporator (CHA Mark 40). Then, a thin layer (250 nm) of PMMA 950 C4 was spun onto the aluminum plate. Next, the nanoaperture grid was patterned on PMMA through the use of an electron beam writer (Leica EBPG 5000). The grid pattern was then transferred onto aluminum by a Chlorine based reactive ion etcher. Finally, the PMMA residue was

completely stripped off by Methylene chloride. A picture of the final device is shown in Fig. 7-6(c).

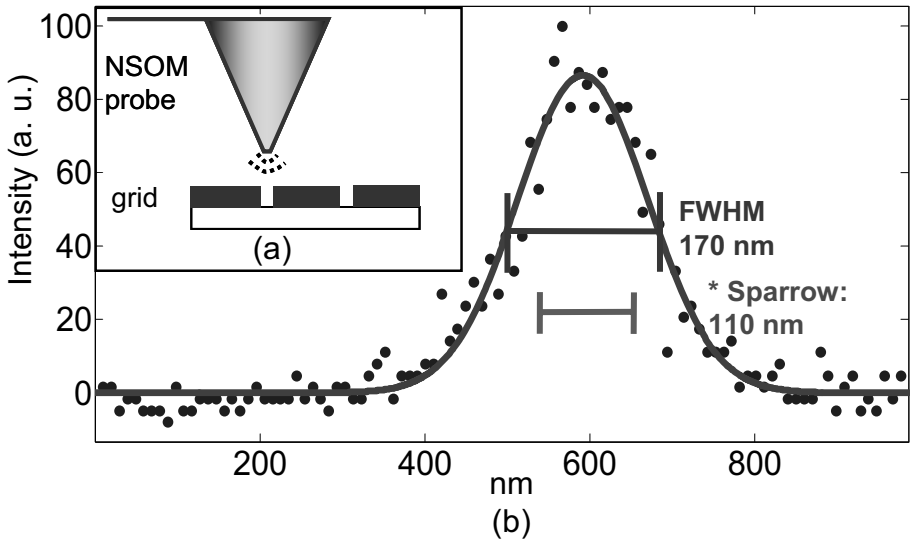

Figure 7-8: Measurement of the resolution limit. (a) Illustration of the measurement scheme, where the NSOM probe is taken as a virtual point source. The tip is held in close proximity to the nanoaperture plane. (c) The point-spread-function profile of a typical nanoaperture as measured with the NSOM tip; the width is 170 nm (FWHM). The dark solid line is a Gaussian fit to the curve of the point spread function. * After accounting for the finite NSOM tip size, the near-field imaging resolution of this nanoaperture is established to be 110 nm (Sparrow's criterion).

It is well known that the resolution limit of the nanoaperture based imaging system is determined by the size of the nanoaperture [2, 9]. It is often desirable to verify the fundamental resolving power of the nanoaperture grid before putting it into use.

We performed a resolution check of our system with the help of a commercial NSOM system (WITec alpha-SNOM, tip diameter= 100 nm, λ= 650 nm). The characterization scheme was the same as that presented in a previous paper published by our group [9] , and it is illustrated in Fig. 7-8 (a). The NSOM tip served as a nanometric test object in this

experiment. Fig. 7-8(b) shows the result with a typical nanoaperture. It was found that the "point spread function", as measured with the NSOM, had a FWHM value of 170 nm.

The approximation of the NSOM tip as a point source was no longer solid in this experiment for the reason that the nanoapertures were nearly as small as the tip (~100 nm). Therefore, the size effect of the NSOM tip should be removed from the plot of the "point spread function".

A rigorous treatment of such a size effect requires the complete description of the complicated near field scattering of vectorial optical fields, which is out of the scope of this study. However, a simpler method that uses the scalar quantity of the field, e.g. the optical intensity was able to remove the size effect to some satisfaction.

In other words, we could approximate that the resulting profile of the "point spread function" (Fig. 7-8(b)) was a convolution of the real point spread function of the nanoaperture and the size function of the NSOM probe; the size function was in fact the near field diffraction profile of the tip. Here, we assumed such a diffraction profile was a Gaussian function with a FWHM equal to the tip size.

As such, by accounting for the finite NSOM tip size (~100 nm) and deconvolving its contribution from the measurements, we obtained a near-field resolution of 135 nm (FWHM) or 110 nm (Sparrow's criterion, Fig. 7-8(b)) for the aperture grid. These two values can be taken as good estimates of the resolution limit of this imaging system.

The setup of the imaging system and the operating principle of grid OFM

The imaging segment of the entire system is shown in Fig. 7-9: a white LED or a red laser illuminated the nanoaperture grid from its back side. The transmission through the nanoapertures was collected by an infinity-corrected objective lens (Olympus, 40X, NA = 0.8, water, IR) and then projected onto the recording CCD camera (Princeton Instruments, Spec10-100) with an achromatic camera lens (f= 20.0 cm from Thorlabs).

The theory of nanoaperture imaging in near field is complex. A vivid example of how nanoaperture interacts with the nanoscopic object in a 2D situation can be found in one of Novotny et al.'s theory papers [15]. In general, the presence of a scatterer above the

nanoaperture interrupts and scatters the light emitted from the nanoaperture. Such "disturbance" causes changes in the signal recorded by the camera. Fig. 7-10 shows an example of a NIST-standard bead (10 μm) passing a vertical array of nanoapertures. By measuring such time varying transmission changes of all the apertures, an image of the target can thus be produced.

From Fig. 7-10, we can also see that the transmission power through apertures had a large difference between each other. There are a few reasons for this. First, the fabricated apertures might have slight difference in size. A 20% change in the final aperture size would have introduced three times (i.e. 1.2^6) of difference in the transmission power, when borrowing Bethe's sixth-order empirical law of nanoaperture transmission [16]. The second reason is that the illumination from the backside of the nanoaperture plate (Fig. 7-9) might not be uniform. When removing the nanoaperture plate, there was indeed light intensity non-uniformity within the field of view (~ 30μm x 250μm) on the screen of the camera. Note that the variation of the transmission between individual apertures has been normalized based on the difference in aperture size during the data processing step. As such, the amount of the change in the transmission intensity reflected the genuine scattering/absorption events from the object itself.

Another noteworthy remark is that sometimes, the transmission intensity of a few apertures had a sudden decrease during my experiment and never went up again. This is probably because some tiny particles or molecules within the fluid fell into the tiny hole and blocked the transmission. In such a case, the obtained raw data should be discarded, as they did not represent real line-scans across the object. Fortunately, such a sudden decrease of transmission power showed up nicely in the raw data and this it was easy for one to make a decision whether such a blocking event took place during data acquisition process.

In OFM, the time-varying transmission changes associated with each nanoaperture in fact represented a line scan across the target. By choosing to tweeze the target across the nanoapertures at a small tilt angle (θ) with respect to one of the principle axis of the grid (x-axis in Fig. 7-11), we were assured that the line scans acquired with the nanoapertures overlapped appropriately and fully covered the entire sample, a sufficient sampling

condition. The parameters we used specifically for the imaging experiment will be detailed later.

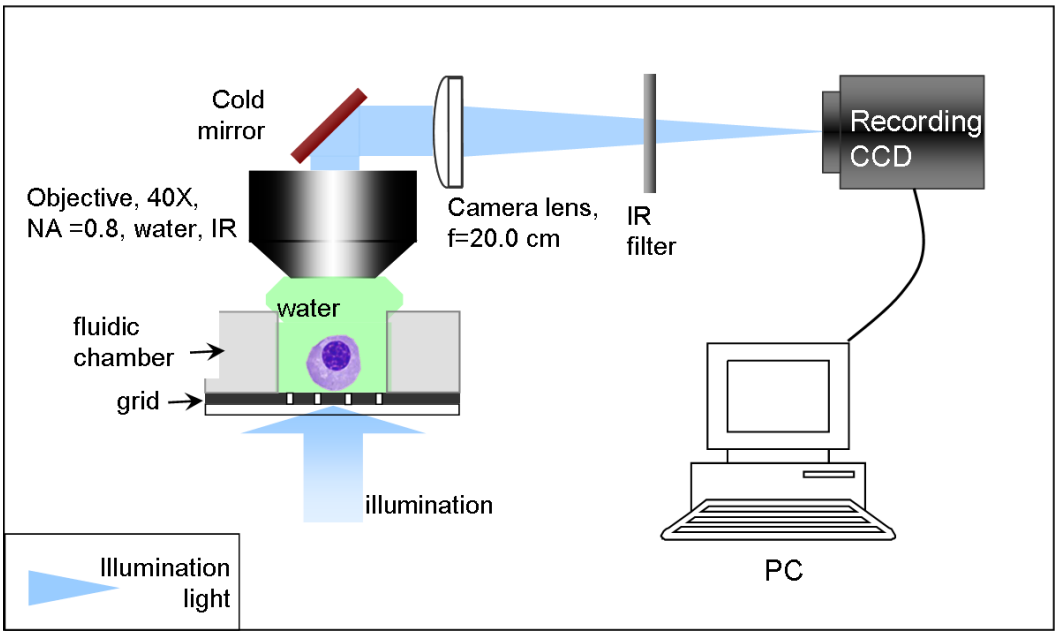

Figure 7-9: Setup of the imaging part. Cold mirror (R: 400-700 nm, T: 780 nm onward, from Newport). Objective lens: Olympus, 40X, NA=0.8, water, IR. Infrared filter: Newport short-pass @ 650 nm; Recording CCD: Princeton Instruments (Spec10-100).

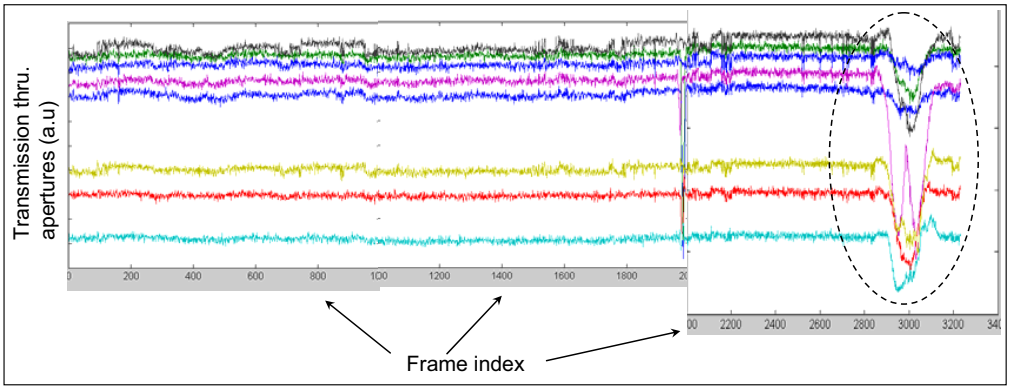

Figure 7-10: Example of a NIST standard bead (10 μm) passing a vertical array of nanoapertures. Near the end of the time traces, the passage of the microsphere is clearly seen.

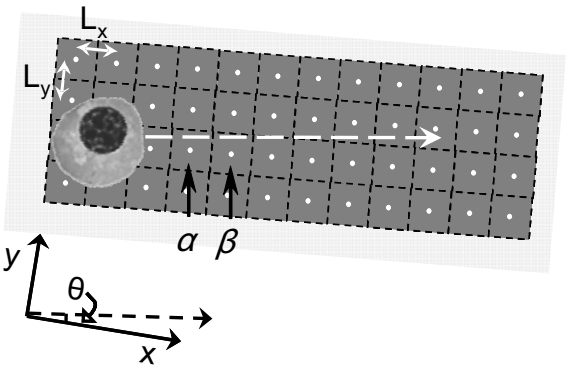

Figure 7-11: The orientation of the nanoaperture grid with respect to the scanning direction of the sample. L_x: hole spacing in x direction; L_y: hole spacing in y direction; θ: the angle between the scanning direction of the sample and the x axis.

The appropriate composition of the acquired line scans to form an image of the target required knowledge of the spacing between nanoapertures (L_x, L_y), the target's flow speed (V), and the assurance that the object maintained its shape and orientation during the entire image acquisition process. The composition process was straightforward. For example, nanoaperture α and β in Fig. 7-11 acquired adjacent line scans of the target. As the object passed nanoaperture α before it passed β, the line scan associated with nanoaperture β needs to be time shifted by

$$\Delta t = \frac{L_x \cos\theta}{V} \tag{7.3}$$

in order to synchronize with the line scan associated with nanoaperture α.

More generally, the time delay factor can be computed from:

$$\Delta t = \frac{L_x \cos\theta}{V}(n-1) - \frac{L_y \sin\theta}{V}(m-1) \tag{7.5}$$

where m (or n) is the row (or column) index of the nanoaperture in question.

The pixel density of the final OFM image had the following characteristics. The pixel size in y direction (δy) and that in x direction (δx) can be expressed as follows:

$$\delta y = L_x \sin(\theta)$$
$$\delta x = V\delta t \tag{7.6}$$

where δt is the CCD camera time step. In our experiment, we set the scanning speed of the trapped sample at V= 0.7 μm/sec, and the camera's frame rate at δt = 0.11 second/ frame. The tilt angle θ was finely adjusted to be 0.03 in rad. Under this condition, the pixel size δy was ~75 nm, and δx was ~80 nm. It is worth noting that the resolution of this system is given by the larger of the following two factors: twice of image's pixel size (i.e. $2\delta x$, $2\delta y$) or the FWHM of the transmission profile associated with the nanoaperture.

The complete system: optical tweezers + grid-based OFM

The complete setup that integrates the optical tweezer function and nanoaperture imaging function is shown in Fig. 7-12. The inset shows the arrangement of the nanoaperture grid, the virtual sample, and the objective lens.

The integration of the metallic nanoaperture plate directly onto the light source (such as LED or laser diode) is quite straightforward by making use of the state-of-the-art semiconductor technology and very-small-aperture light source technology [17].

An optical tweezer can also be made up of multiple traps [5], which can enable parallel processing of a number of samples at the same time. However, integrating optical tweezer onto a chip is not as simple, although there has been steady progress in this direction [18]. We believe that in near future there will be a variety of imaging systems-on-a-chip with flexible sample actuation schemes. They will surely be able to replace bulky microscopes in many applications.

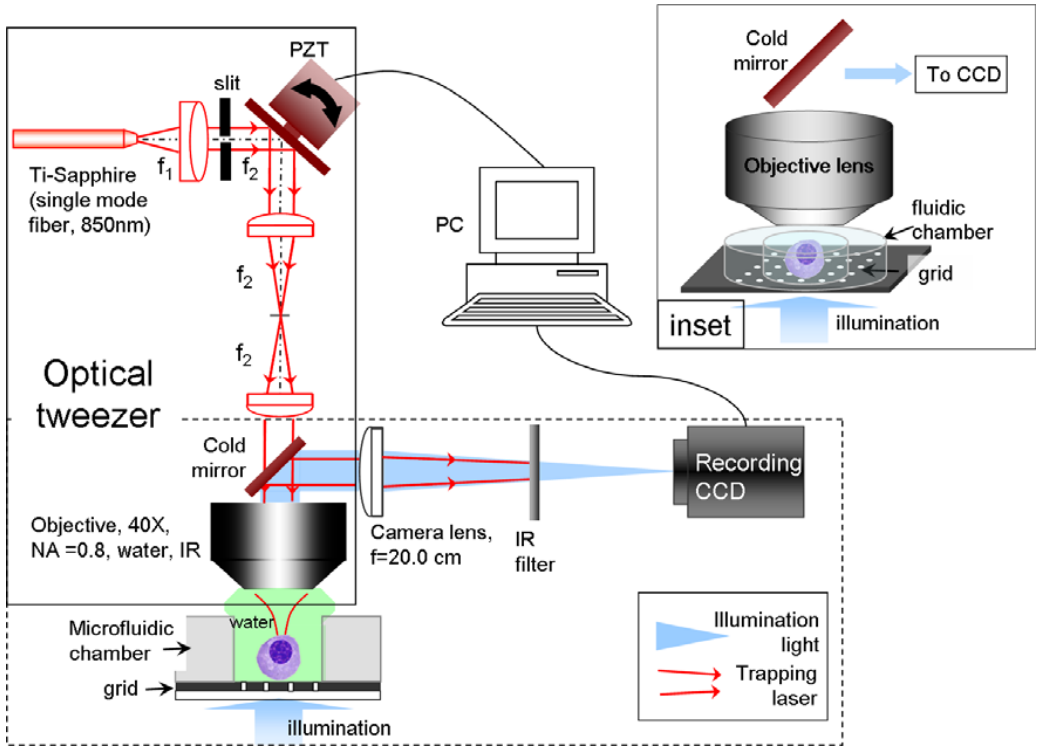

Figure 7-12: Setup of the entire imaging system.

7.4 Application in high resolution OFM

In our experiment, the tested illumination sources included a He-Ne laser (Melles Griot, 633 nm, 20 mW) and a white light LED (Lamina, titan series, daylight white). Both light sources have their own importance depending on the applied field. Lasers, as a coherence source, are essential in the development of fluorescence OFM imaging or interferometer-related OFM systems [19]. White LED is useful in producing cheap OFMs for point-of-care or on-field testing.

We demonstrated the ability of this optical tweezer-coupled OFM system by imaging polystyrene beads and paper mulberry pollen spores. Figure 7-13 (b2, c2) show OFM

images of two different paper mulberry pollen spores (Duke Scientific, diameter =11 μm - 17 μm). Fig. 7-13 (d2) shows an OFM image of a 10μm polystyrene microsphere under LED illumination and Fig. 7-13 (e2) shows an image of a smaller polystyrene microsphere (Duke Scientific, Cytoplex, 5 μm) when we used the He-Ne laser as illumination.

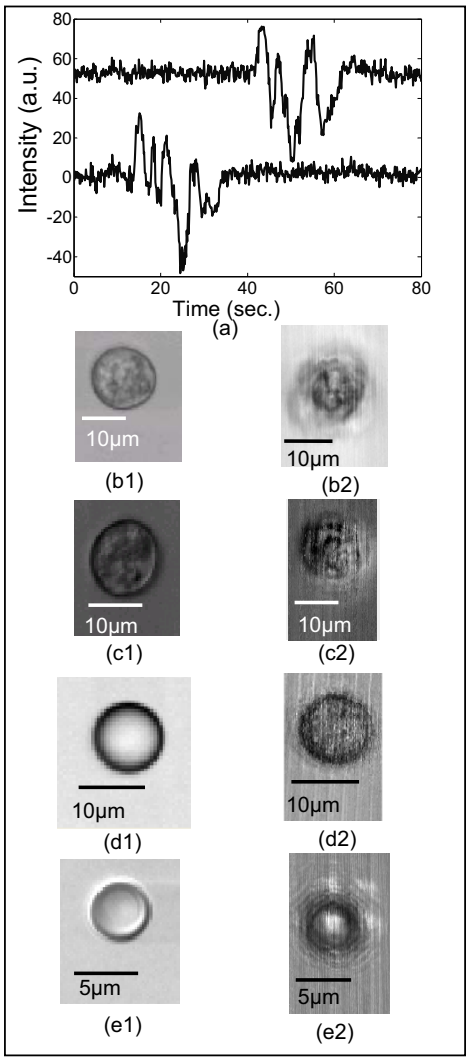

Figure 7-13: (a) An example of the transmission time-of-flight traces from two nanoapertures that are in the same row but $10L_x$ (i.e. 25 μm) apart. The sample is a pollen spore. (b1, c1) Microscope images of two paper mulberry pollen spores. The microscope set is the same as Fig. 7-11 except that the nanoaperture plate was removed. (d1, e1) Microscope image of 10μm and 5μm polystyrene microspheres. (b2, c2) OFM images of two paper mulberry pollen spores. (d2) OFM image of a 10μm microsphere. (e2) OFM image of a 5μm microsphere under laser illumination. Note that the samples used for OFM imaging are not necessarily those used in microscope imaging.

It can be seen that OFM images were able to uncover some fine structures of the microscopic objects. Fig. 7-13 (b1, c1, d1, e1) are corresponding images acquired with the home-built imaging system, shown in Fig. 7-12, except that the nanoaperture plate was not used.

We found that the OFM acquired images at this resolution were different in appearance from the conventional microscope images, especially in the depth of the image. It is mainly because the depth of field (DOF) associated with OFM is significantly shorter than that of a conventional microscope. Through a simple diffraction analysis by the finite element methods (COMSOL Multiphysics [20], we have calculated that the point spread function associated with a typical nanoaperture (D=100 nm, λ= 650 nm) will double in width at a distance of about 120nm away from the nanoaperture plane.

On the other hand, the DOF of a conventional microscope can be estimated in the case of Gaussian beam focusing by the same microscope objective lens (40X, NA= 0.8, water, λ=650 nm)). Our calculation shows that the point spread function for the microscope objective will double in width at a distance of about 1.0 μm from the plane of focus, which is about an order of longer than the 100nm nanoapertures.

Similar to NSOM, to obtain the best resolution with the OFM system, the object is required to be as close to the nanoaperture grid as possible. A rule-of-thumb number for such a separation is $\lambda/4\pi$. The blurry edges shown in some of the OFM images can be attributed to the fact that the edges of the ellipsoidal objects were at appreciable distances from the nanoaperture plane.

The relatively low quality of the periphery of the acquired images can be attributed to the fact the edges of the object were not close enough to the nanoaperture grid. Going forward, this also suggests that target object will need to be intrinsically flat so that the object can make maximal contact with the grid or a means for flattening the object against the grid is needed. Note that such a limitation of nanoaperture based OFM also exists in commercial NSOM and total internal refection fluorescence microscope (TIRFM).

Nevertheless, we recognize that the path to acquiring high quality NSOM-type images is a long one. Better and more robust means of controlling the samples is required, such that

larger portion of a sample can be placed sufficiently close to the nanoapertures. We believe the image quality can be improved significantly by implementing a means to squash the object against the grid. Achieving such a condition without significantly disturbing the functions of the biological objects is not technologically trivial and deserves further investigation.

Furthermore, there are several significant differences associated with a grid based OFM in comparison with an array based OFM. First, when imaging the same object, a grid-based system can be much shorter than an array-based system.

The shortening of the imaging region makes it easier for the flow strategy to satisfy the OFM's requirements, i.e. stable, rotation-free object transportation during the imaging process. For example, when imaging a cell (diameter, D= 9μm) with an array based OFM (δy =75 nm, L_x= 2.5 μm), the object would need to maintain a constant speed and a steady orientation within a scan range of 300 μm (i.e., $D*\sin^{-1}(\theta)$). However, with a grid-based system, the object would only need to remain stable for a distance of about 83 μm (i.e., $L_x*\sin^{-1}(\theta)$).). This can potentially be a significant implementation advantage for situation, where the target's shape or orientation is particularly susceptible to change – the shorter the scan duration, the less chance of a shape or orientation change ruining the image acquisition process.

In the case of imaging an elongated object such as a *C. elegans* larva (15 μm wide (Wid.) and 300 μm long (Le)), the 1D array based OFM (with the same parameters as the previous example), the object would need to maintain static orientation within a scan range as long as 800 μm, i.e. $D*\sin^{-1}(\theta)$ + Le. On the other hand, for a grid-based OFM (with the same parameters as the previous example), the object needs such stability for a total scan range 383 μm, i.e. $L_x*\sin^{-1}(\theta)$ + Le.

In addition, even as an off-chip and bulk optical implementation, the grid design is an efficient way to implement simultaneous scans of multiple samples. On the other hand, the array design is well suited for direct implementation on a linear CCD or CMOS sensor array. The grid design requires the use of a 2D sensor chip.

This type of OFM is to some extent a simplified implementation for NSOM systems. The OFM brings two advantages in this respect. First, multiple nanoapertures can

simultaneously scan the target at the same time – the total number equals the number of nanoapertures the target object overlaps at a given time during the scan. Second, this approach drastically simplifies the scanning pattern: with the grid based OFM, the target object needs only to make a single sweep over the grid, as opposed to a complicated raster scan pattern that a conventional NSOM system employs. However, the 100 thousand dollars spent on a commercial NSOM is often worth it. For example, the near-field separation between sample and the tip enabled in NSOM is by no means guaranteed by grid-based OFM. Therefore, OFM with smaller nanoapertures should be more applicable in areas that require high-throughput screening but are not selective in terms of the ultimate resolving power.

Concluding remarks of this chapter

In conclusion, we have presented a new type of OFM system - nanoaperture-grid based OFM, which is comprised of a 2D nanoaperture grid that functioned as an illumination source, an optical tweezer that translated the target sample over the grid, and a collection system that measured the time varying transmission changes associated with the nanoapertures during the scan. This OFM shared a similar image formation mechanism with illumination-mode nano-ABIDs and had an experimentally determined resolution limit of 110 nm (Sparrow's criterion). The simplified scan pattern and simultaneous scanning nature of this implementation indicated that this is a simpler and potentially faster scanning replacement for the NSOM for a range of applications.

In addition, this paper also reported on the first application of the optical tweezer as a sample delivery mechanism for aperture based imaging. By using a moderate laser power (20mW), we showed that an asymmetric optical scanner was able to firmly trap and stably transport micron-sized samples. The robustness of the optical tweezer was tested by measuring the deviation of trapped microspheres. We demonstrated the use of this system by acquiring images of polystyrene microspheres and mulberry pollen spores with both coherent and incoherence illumination sources. Note that images acquired through this study were mid-quality and were unable to show the full high resolution potential of this

system. There remains the technical challenge of effectively pushing the target objects so that they are flat against the scanning grid.

In addition, optical tweezers can readily be made into a tweezer array, which will dramatically improve the imaging efficiency. Furthermore, additional imaging functionality, e.g. fluorescence, can also be integrated into the system thanks to the rapid development of on-chip filters [21].

Reference

1.X. Heng, E. Hsiao, D. Psaltis, and C. Yang, "An optical tweezer actuated, nanoaperture-grid based Optofluidic Microscope implementation method," Optics Express **15**, 16367-16375 (2007).
2.D. Courjon, *Near-field microscopy and near-field optics* (London: Imperial College Press, 2003).
3.X. Heng, D. Erickson, L. R. Baugh, Z. Yaqoob, P. W. Sternberg, D. Psaltis, and C. Yang, "Optofluidic microscopy- a method for implementing a high resolution optical microscope on a chip," Lab on a Chip **6**, 1274 - 1276 (2006).
4.A. Ashkin, J. M. Dziedzic, J. E. Bjorkholm, and S. Chu, "Observation of a single beam gradient force optical trap for dielectric particles," Optics Letters **11**, 288-290 (1986).
5.D. G. Grier, "A revolution in optical manipulation," Nature **424**, 810-816 (2003).
6.J. Enger, M. Goksor, K. Ramser, P. Hagberg, and D. Hanstorp, "Optical tweezers applied to a microfluidic system," Lab on a Chip **4**, 196-200 (2004).
7.K. Konig, H. Liang, M. W. Berns, and B. J. Tromberg, "Cell damage in near-infrared multimode optical traps as a result of multiphoton absorption," Optics Letters **21**, 1090-1092 (1996).
8.A. T. O'Neil, and M. J. Padgett, "Rotational control within optical tweezers by use of a rotating aperture," Optics Letters **27**, 743-745 (2002).
9.X. Heng, X. Q. Cui, D. W. Knapp, J. G. Wu, Z. Yaqoob, E. J. McDowell, D. Psaltis, and C. H. Yang, "Characterization of light collection through a subwavelength aperture from a point source," Optics Express **14**, 10410-10425 (2006).
10.P. Jordan, J. Leach, M. Padgett, P. Blackburn, N. Isaacs, M. Goksor, D. Hanstorp, A. Wright, J. Girkin, and J. Cooper, "Creating permanent 3D arrangements of isolated cells using holographic optical tweezers," Lab on a Chip **5**, 1224-1228 (2005).
11.A. Ashkin, "Forces of a single-beam gradient laser trap on a dielectric sphere in the ray optics regime," Biophys. J. **61**, 569-582 (1992).
12.K. C. Neuman, and S. M. Block, "Optical trapping," Review of Scientific Instruments **75**, 2787-2809 (2004).
13.H. Raether, *Surface Plasmon on Smooth and Rough Surfaces and on Gratings* (Springer-Verlag, Berlin, Germany, 1988).
14.J. T. van Wijngaarden, E. Verhagen, A. Polman, C. E. Ross, H. J. Lezec, and H. A. Atwater, "Direct imaging of propagation and damping of near-resonance surface plasmon polaritons using cathodoluminescence spectroscopy," Applied Physics Letters **88** (2006).

15.L. Novotny, D. W. Pohl, and P. Regli, "Light-propagation through nanometer-sized structures - the 2-dimensional-aperture scanning near-field optical microscope," Journal of the Optical Society of America a-Optics Image Science and Vision **11**, 1768-1779 (1994).
16.H. A. Bethe, "Theory of diffraction by small holes," Physical Review **66**, 163-182 (1944).
17.A. Partovi, D. Peale, M. Wuttig, C. A. Murray, G. Zydzik, L. Hopkins, K. Baldwin, W. S. Hobson, J. Wynn, J. Lopata, L. Dhar, R. Chichester, and J. H. J. Yeh, "High-power laser light source for near-field optics and its application to high-density optical data storage," Applied Physics Letters **75**, 1515-1517 (1999).
18.S. Cran-McGreehin, T. F. Krauss, and K. Dholakia, "Integrated monolithic optical manipulation," Lab on a Chip **6**, 1122-1124 (2006).
19.M. Lew, X. Cui, X. Heng, and C. Yang, "Interference of a four-hole aperture for on-chip quantitative two-dimensional differential phase imaging," Optics Letters **32** (2007).
20.COMSOL_Multiphysics_3.3, in *COMSOL Inc. (http://www.comsol.com/)*.
21.M. M. Dandin, "Optical filtering technologies for integrated fluorescence sensors," Lab on a Chip **7**, 955-977 (2007).

Chapter 8

CONCLUSION OF MY THESIS

8.1 Summary of my graduate work

Compact, high-throughput imaging or screening/sorting systems are greatly needed in a large variety of fields, where an optical microscope or an expensive flow cytometer is either unnecessary or unavailable. Microfluidics is arguably the most promising platform for the next generation of "Labs-On-a-Chip", although there were few reports on the development of compact imaging devices that could be easily integrated with microfluidics. In my thesis, I discussed in detail the implementation of one such device, termed Optofluidic Microscope (OFM).

OFM improves the resolving power of a commercial CMOS (or CCD) camera by introducing an array of nanoapertures directly on top of the camera (Fig. 8-1). To some extent, such a design can be considered as redefining the pixel size of the camera pixels.

In essence, OFM utilizes a lensless imaging technique, which brings forth two immediate advantages: 1) The imaging process of OFM does not rely on imaging lenses, and thus the device can be made both compact and cheap. One of our reported OFM prototypes is smaller than the size of an iPod video [1]. 2) Depending on the specific applied field, the resolving power of OFM can be easily tuned by fabricating nanoapertures with difference sizes. Such a fabrication process costs much less than purchasing an objective lens.

More importantly, the planar nature of the nanoaperture array enables its integration into a microfluidic platform (Fig. 8-1) without incurring many technological challenges. The basic integration strategy of OFM is to fabricate the nanoaperture array and the microfluidic device as separate modules, and then mount them together with the help of alignment markers. In the complete device, the nanoaperture array + CMOS camera carries

out all the imaging functions, whilst the microfluidic chip is used as an agile sample delivery component. As the two functional chips are fabricated as individual modules, the disposal and replacement of one module have minimal effects on the functioning of the other one.

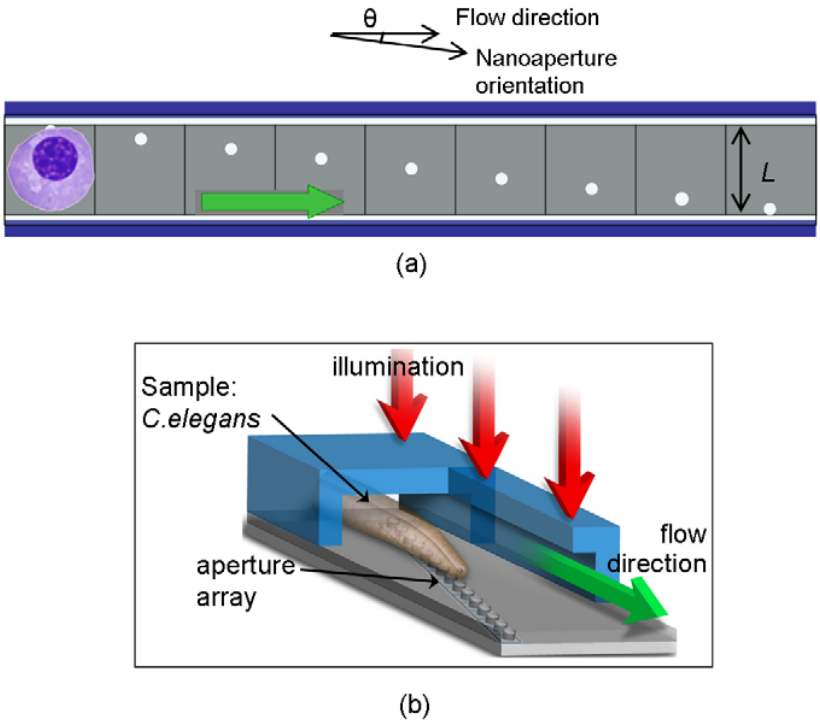

Figure 8-1: (a) OFM design: the nanoaperture array is patterned in a slanted fashion on the CMOS camera. The artificial time delay between adjacent apertures is used to correct the geometry distortion in the image. (b) Illustration of an OFM device for *C. elegans* imaging.

The first OFM prototype was not completely on-chip, i.e. a microscope was used to relay the transmission time-traces from the nanoapertures onto a CCD camera. However, we successfully demonstrated OFM's potential as a high-performance imaging device (resolution limit: ~490 nm, throughput: ~40 worms per minute at maximum [2]).

Then we carried out a phenotype study of two different *C. elegans* larvae: wild type and dpy-24. The separation of two such genotypes on the morphology map (Fig. 8-2(b)) was a success. Considering *C. elegans*' significance in various fields of biology and biochemistry, the imaging capability of OFM demonstrated in such an initial experiment could surely inspire future designs of low-cost nematode imagers.

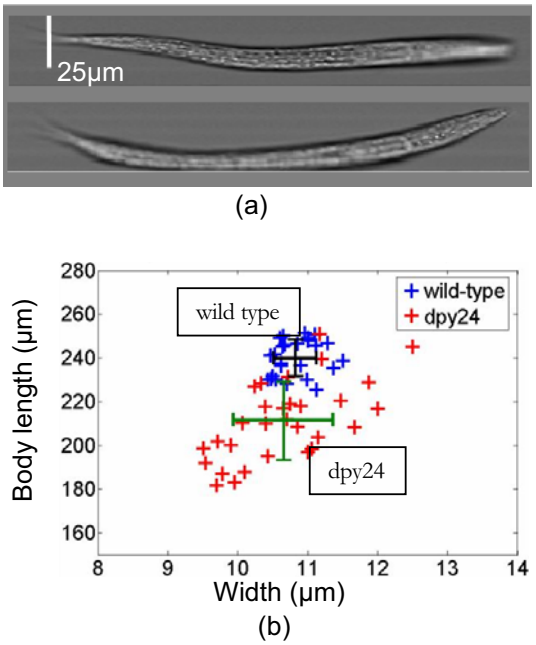

Figure 8-2: (a) Representative examples of *C. elegans* images. (b) Aspect ratio map of wild-type larvae (25 entities); aspect ratio map of dpy-24 mutants (31 entities).

Unlike common nanoaperture based imaging systems (such as NSOM), OFM is more prone to resolution variation, due to variation of the sample-nanoaperture separation. Therefore, we performed a detailed study of the nanoaperture based imaging devices of two different configurations (Fig. 8-3), while the main attention was paid to type II ABID [3].

The relationship of the resolution variation with the sample-nanoaperture separation was investigated by using both a FEM based computation method and a NSOM based experimental scheme (Fig. 8-4). Such a resolution trend of type II ABID can be taken as plausible guidance to new designs of nanoaperture based imaging devices.

One of the surprising findings of this work is that the directionality of the diffracted waves may or may not depend on the angle of the incident waves. The threshold of such dependence was found determined by the ratio of the wavelength and the diameter of aperture (λ/D). However, such an effect with aperture of other shapes remains unclear.

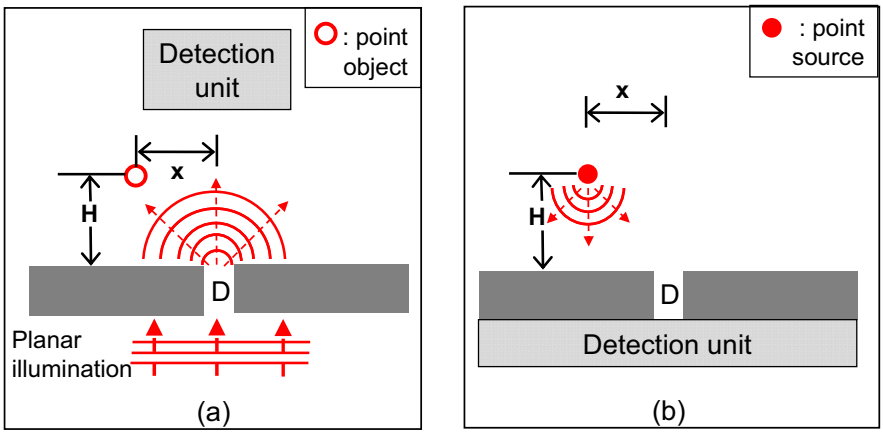

Figure 8-3: Two schemes of subwavelength aperture based imaging devices (ABIDs): (a) type-I, (b) type-II.

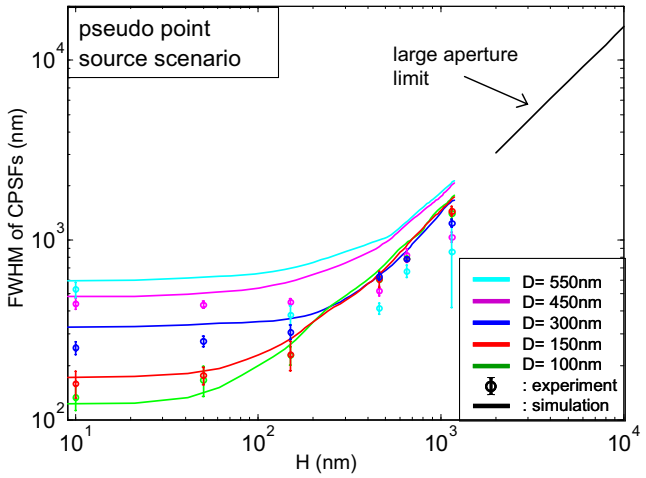

Figure 8-4: (log-log scale): CPSF's FWHM *versus* the gap height (H) for a range of aperture sizes (pseudo point source scenario). The lines represent simulation results and the circles represent experimental data. The light source is modeled as an effective isotropic point source. Black line: the far field trend of large apertures (FWHM ~ 1.53 H). The collection N.A. for the transmission is effectively unity.

If circular nanoapertures are considered a truncated version of the metallic waveguides, then such a "threshold effect" of the circular nanoapertures can be related with the guided modes of their waveguide counterparts. This discovery has direct relevance with some of the existing nanoaperture based optical devices, such as differential phase OFM [4] and nanoaperture based beam profiler [5].

In Chapter 7 of my thesis, I introduced two innovative designs for OFM: nanoaperture grid array and optical tweezer actuation (Fig. 8-5(a)) [6]. Nanoaperture grid is in fact a 2D nanoaperture array defined on a thin metallic film. Nanoaperture grid can be considered as segmenting the long 1D nanoaperture array into shorter pieces and then folding them back to align with the leading aperture, as shown in Fig. 8-5(b). Thus, the total length of a nanoaperture grid can be 5-10 times shorter than 1D nanoaperture array, thus making OFM much less vulnerable to sample rotation/tumbling. In addition, when assuming identical camera speed and flow speed, OFM based on nanoaperture grid can be 5-10 times faster than that based on 1D array.

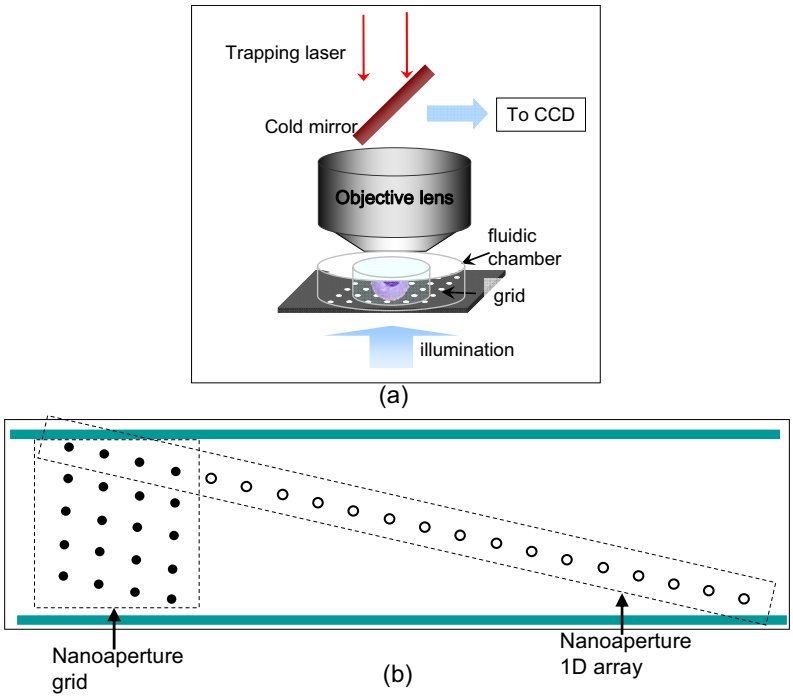

Figure 8-5: (a) Arrangement of the 2D nanoaperture grid (for illumination), objective lens (also for optical tweezing) and the fluidic chamber (for reducing sample jittering). (b) Illustration of the nanoaperture array and the nanoaperture grid.

We applied the nanoaperture grid to high resolution imaging of a few samples that are around 10 μm in diameter (Fig. 8-6). Such a size range is tens of times smaller than that of a microorganism, like nematode. Therefore, in this work, we successfully demonstrated that OFM could be used to produce images of both small animals and single cells.

Furthermore, we set up an optical tweezer scanner to actuate the transportation of micron-sized samples. The optical tweezer has advantages in holding the sample and then actuating it with high flexibility and superb accuracy. We employed an asymmetrical optical tweezer to translate microspheres and pollen spores across the region of the nanoaperture grid. The holding accuracy of our tweezer setup could be within 50 nm, which was verified both theoretically and experimentally.

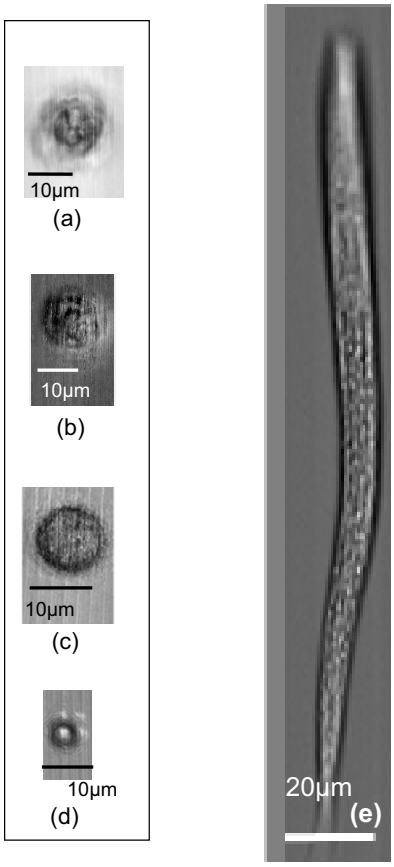

Figure 8-6: OFM images of a few representative samples: (a, b) Mulberry pollen spores; (c) 10μm polystyrene bead; (d) 5μm polystyrene bead (laser illumination); (e) *C. elegans* larva

8.2 Preliminary results of new OFM functions

In addition to the reported results on the technology development of Optofluidic Microscopy [1, 2, 6], I have also investigated a few modified versions of OFM during my Ph.D. work. I will hereby briefly talk about two of the more significant functions that will benefit OFM almost immediately: fluorescence and electrokinetic actuation.

Fluorescence

The significance of fluorescence for the biology community is immense. Chemically tagging the biological entity of interest with fluorescent molecules enables sensitive and quantitative characterization of the biological sample. OFM, as a new class of compact imaging platform, will certainly find many applications if its fluorescence capability can be demonstrated. Therefore, by using the same setup of the nanoaperture grid and the optical tweezer, we performed a proof-of-concept experiment of "fluorescence OFM".

In this initial prototype, the fluorescence filter was not deposited directly on-chip. Instead, we placed an external fluorescence filter right in front of the recording camera (Princeton Instruments, Spec 10), as illustrated in Fig. 8-7.

The laser excitation source is a highly-coherent 10mW He-Ne laser (633 nm) with a default beam diameter of ~2 mm. We selected a fluorescent species of microspheres (Cytoplex, 5μm, Duke Scientific) as a test object. The emission wavelength of the fluorescent molecules (Cy-5) is centered at 680 nm. As such, we selected a 660nm longpass filter to block the excitation wavelength. In addition, the IR filter (Fig. 8-7) effectively removed the intervention from the trapping laser.

The imaging procedure can be summarized by Fig. 8-8(a). After knowing the locations of individual nanoapertures, we inserted the fluorescence filter and recorded the fluorescence signals from each nanoaperture (Fig. 8-8(b) as an example). Note that such a fluorescence time-of-flight signal needed to be normalized by the transmission strength of individual nanoaperture.

The image construction procedure is identical to that for direct imaging, which we have discussed in Chapter 7. Figure 8-8 (b) shows images of a fluorescent microsphere.

Note that the fluorescent dyes were actually dispersed in the entire body of the microsphere, thus making it impossible to identify the in-focus and out-of-focus portions of the microsphere. A better sample would be a chemically modified microsphere with fluorescence molecules only tagging the surface of it. Such a microsphere can be easily produced by making use of the amino-carboxylic chemistry.

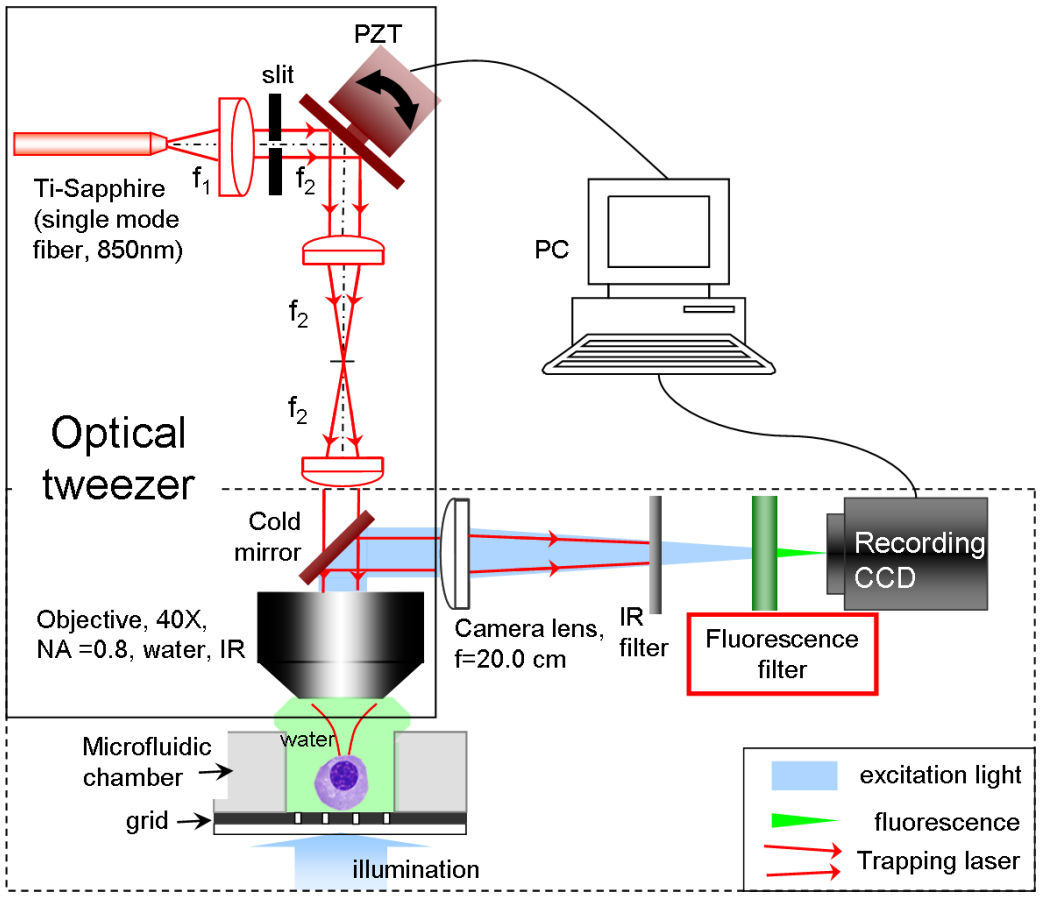

Figure 8-7: Setup of the entire imaging system (optical tweezer + nanoaperture grid)

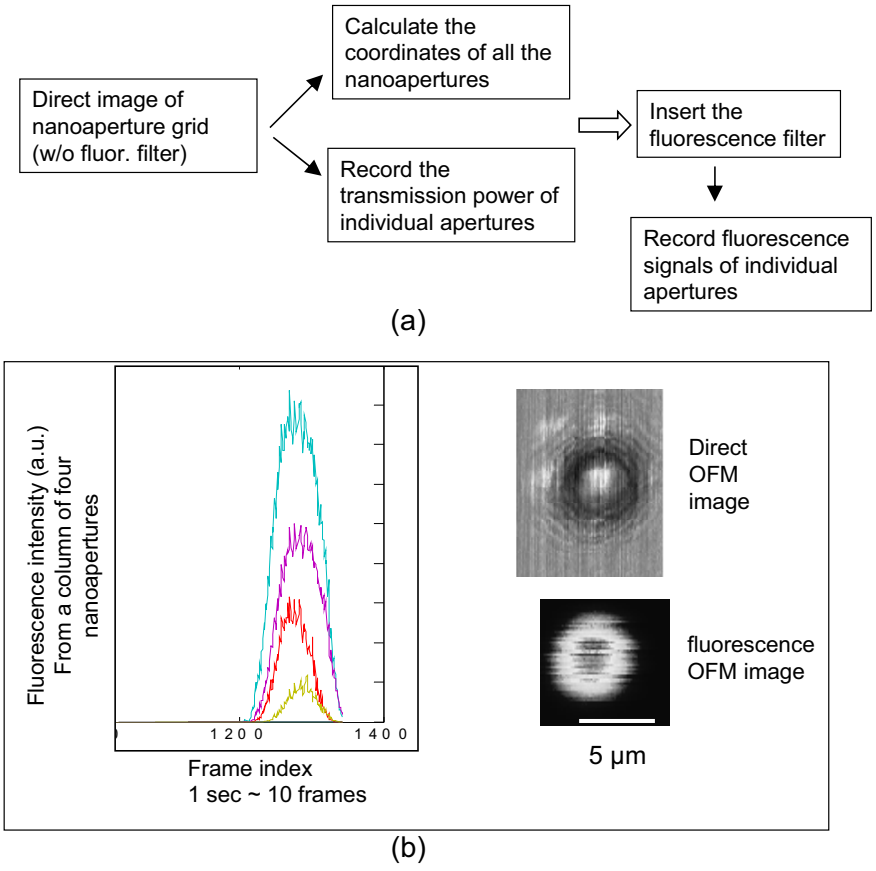

Figure 8-8: (a) Procedure of the fluorescence imaging experiment with the nanoaperture grid device. (b) Preliminary results with 5μm fluorescent bead (Cy5): fluorescent time-of-flight signals from four nanoapertures in the same column; direct OFM image; fluorescence OFM image.

Electrokinetic pumping

Numerous fluidic pumping mechanisms can be easily combined with the platform of Optofluidic Microscopy. In the initial OFM prototype, we employed a gravitation-driven

flow scheme to actuate the translation of *C. elegans* larvae. Although pressure driven flow might work fine for elongated microorganisms, it may cause severe sample rotation for more spherical-like objects such as white blood cells, because the velocity profile of fluid in a microfluidic channel in parabolic, causing the top and the bottom of the spherical sample to have a velocity difference; such a velocity difference leads to a torque to the sample body, thus causing it to rotate.

Therefore, a more plausible fluid actuation method is desired in order to eliminate sample rotation. An asymmetric optical tweezer as explained in Chapter 7, to some extent, can satisfy such a request. However, it is not a high throughput method and may require human intervention in the middle of the experimentation. Therefore, developing a fast and automated optical tweezer instrument is appealing.

Another promising candidate is electrokinetic pumping. Electrokinetic fluid flow in the microchannel has a flat velocity profile outside the thin Debye double layer (DBL). As such, the embedded spherical objects would not rotate during their passage in the fluidic channel. Besides that, electrokinetics has other superior advantages such as being integratable and highly automated. Therefore, I examined electrokinetic pumping within the framework of OFM.

The selected object was 5μm carboxylic polystyrene microspheres. The microfluidic channel was 40μm wide, 15 μm tall, and 1 cm long. We spun spin-on-glass (SOG, Accuglass 311, 200 nm thick) on top of the metal-coated glass substrate because a non-conductive dielectric layer is required to protect the underlying metallic layer from the fluid. Figure 8-9 is a conceptual drawing of the completed device of electrokinetically actuated OFM.

We used a DC voltage supply (HP E3617A) to drive the fluid actuation. The allowed voltage is from 0V to 64.5V, and the polarity of the DC electrical field can be flipped by a home-made switch. We recorded the sample transportation at the transparent part of the glass substrate by using a CCD camera (DMK 31BF03).

The mean velocity of the microspheres is plotted in Fig. 8-10 with a linear fit. The maximum velocity was about 600 μm/s, with an input voltage of 64.5V. At the maximum voltage, no electrolysis was observed in the channel or on the Pt electrodes. It indicates

that the 200nm thick SOG protected the metallic surface very well. Note that the fitted curve does not intersect with the origin, indicating a non-balanced pressure difference between two electrodes. At zero voltage, the experimentally measured velocity under the residual pressure driven flow was less than 1 μm/sec.

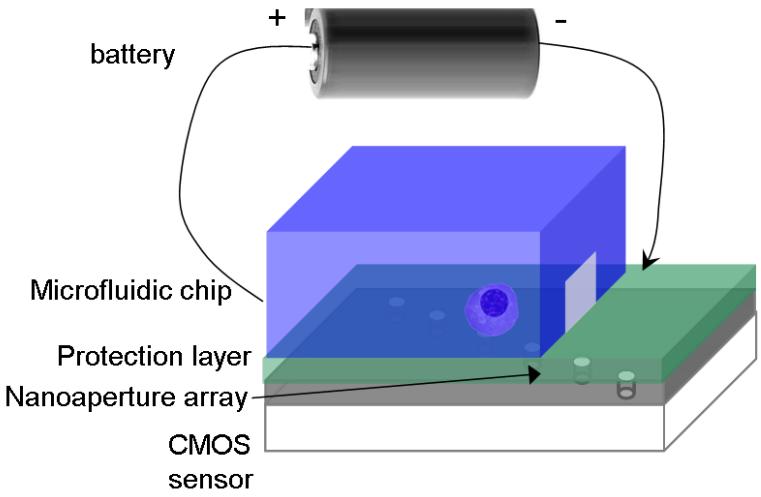

Figure 8-9: Illustration of an electrokinetic enabled OFM device. A normal DC battery is sufficient to actuate the sample transportation. An insulating layer is inserted between the nanoaperture array and the fluidic chip.

Note that the Carboxylated microspheres have negative surface charge (COO^-), and thus they were supposed to move toward the cathode ('+'). However, in my experiments, it was found that the microspheres were always flowing in the opposite direction, probably because the observed transportation of the microspheres is a combined effect of both electrophoresis (as for the microsphere) and electroosmosis (as for water medium). Although the electrophoresis of the microsphere might be toward left, the water's electroosmosis should be in the rightward direction, indicating a positive zeta-potential at the interface of water and PDMS elastomer.

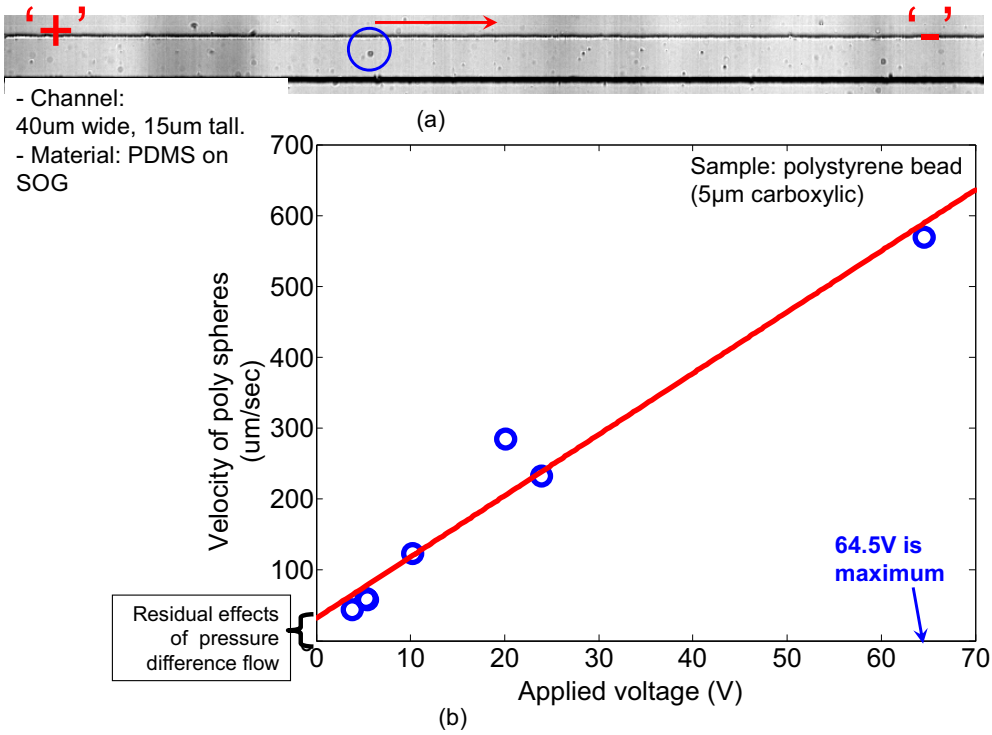

Figure 8-10: (a) Microscope image of a microfluidic channel that is attached on a metal coated glass slide. SOG is used to protect metal from being shorted by electric current. The shown region is without metal coating, so that an inverted microscope could see through the whole stack. (b) Velocity of the polystyrene bead v.s. the applied DC voltage

8.3 Short comments on OFM

Based upon the work described so far in my thesis, I believe that Optofluidic Microscopy (OFM) will continue to grow very rapidly with additional functionality and when improved integration schemes been demonstrated. Here, I will spend the last part discussing about the future development of OFM. I will emphasize, in a very brief manner, both the advantages and the technological difficulties of the new development.

Fluorescence enabled OFM can have a tremendous amount of biological applications, such as studying sub-cellular structures of cells. In my opinion, it will be one of the most important functions of an OFM device. However, there are several problems related to signal strength. First, fluorescence is a weak nonlinear process, which requires a fairly high excitation power. High excitation intensity may introduce sample damage or fluid heating. In addition, a CMOS camera is not as sensitive as usual fluorescence detectors such as PMT or cooled CCD; this indicates that even more excitation power is required. Thirdly, nanoapertures attenuate a high percentage of the incident light. Although surface plasmon polaritions (SPP) may enhance the transmission of the nanoapertures by one or two orders of magnitude, the resolution of such a SPP-assisted OFM may also be comprised. Nevertheless, one advantage of using a nanoaperture array is that the excitation source can be very localized and thus the excitation volume is very small ($\sim 10^{-20}\ m^3$).

Phase sensitive OFM can be realized by using a nanoaperture pair or a quartet [4]. In such a configuration, individual apertures probe the optical fields above them, and subsequently the transmitted optical fields create an interference pattern on the screen tens of micrometers beneath the nanoaperture plane. Such a common-pass, Young's interferometer type of device can be made very compact, thus enabling on-chip interferometric imaging. However, detailed study is required in order to understand completely the nanoaperture's influence on the intensity, phase, and directionality of the incident waves, especially when surface plasmon polaritons inevitably exist; any change of the abovementioned quantities may introduce inaccuracy of the measured differential phase.

The effectiveness of fluid actuation is a critical part of Optofluidic Microscopy, as it determines the efficiency and the fail rate of the imaging process. A sample transportation scheme that is fully automated, high speed and rotation free is most desired by OFM. The fluid actuation methods that I have utilized in my Ph.D. work could not satisfy all the requirements simultaneously. However, we are certain that future development in microfluidic technology will address such issues successfully.

Reference

1.X. Q. Cui, X. Heng, W. W. Zhong, P. W. Sternberg, D. Psaltis, and C. H. Yang, "Imaging microorganisms with a high-resolution on-chip optofluidic microscope," *submitted* (2007).
2.X. Heng, D. Erickson, L. R. Baugh, Z. Yaqoob, P. W. Sternberg, D. Psaltis, and C. Yang, "Optofluidic microscopy- a method for implementing a high resolution optical microscope on a chip," Lab on a Chip **6**, 1274 - 1276 (2006).
3.X. Heng, X. Q. Cui, D. W. Knapp, J. G. Wu, Z. Yaqoob, E. J. McDowell, D. Psaltis, and C. H. Yang, "Characterization of light collection through a subwavelength aperture from a point source," Optics Express **14**, 10410-10425 (2006).
4.M. Lew, X. Cui, X. Heng, and C. Yang, "Interference of a four-hole aperture for on-chip quantitative two-dimensional differential phase imaging," Optics Letters **32** (2007).
5.X. Q. Cui, X. Heng, J. G. Wu, Z. Yaqoob, A. Scherer, D. Psaltis, and C. H. Yang, "Slanted hole array beam profiler (SHArP)- a high-resolution portable beam profiler based on a linear aperture array," Optics Letters **31**, 3161-3163 (2006).
6.X. Heng, E. Hsiao, D. Psaltis, and C. Yang, "An optical tweezer actuated, nanoaperture-grid based Optofluidic Microscope implementation method," Submitted.